UNIVERSITY OF CALIFORNIA SAN DIEGO

Tribological Performance of the Head-Disk Interface in Perpendicular Magnetic Recording and Heat-Assisted Magnetic Recording

A dissertation submitted in partial satisfaction of the

Requirements for the degree

Doctor of Philosophy

in

Engineering Sciences (Applied Mechanics)

by

Tan Duy Trinh

Committee in charge:

Professor Frank E. Talke, Chair
Professor Eric Fullerton
Professor Yeshaiahu Fainman
Professor Michael Tolley
Professor James Friend

2019

The Dissertation of Tan Duy Trinh is approved, and it is acceptable in quality and form for publication on microfilm and electronically:

_____

_____

_____

_____

_____
Chair

University of California San Diego

2019

DEDICATION

To my parents, Ninh Trinh and Oanh Pham, who have always loved me unconditionally, believed in and supported me.

I dedicate this work to my wife, Dr. Linh Phan, who has been a constant source of support, and encouragement, who shares with my ups and downs during the challenges of the Ph.D. program. A very special thank for our sweet and beautiful daughter, Natalie Tuyet Anh Trinh, for being with us. I am truly thankful for having you in my life.

TABLE OF CONTENTS

LIST OF ACRONYMS

CMRR	Center for Memory and Recording Research
LMR	Longitudinal Magnetic Recording
PMR	Perpendicular Magnetic Recording
SMR	Shingled Magnetic Recording
MAMR	Microwave-Assisted Magnetic Recording
HAMR	Heat-Assisted Magnetic Recording
FWHM	Full Width at Half Maximum
HDI	Head-Disk Interface
MWW	Magnetic Write Width
BPM	Bit-Patterned Media
PSA	Pitch Static Angle
RSA	Roll Static Angle
RH	Relative Humidity
LT	Life-Time

LIST OF FIGURES

LIST OF TABLES

ACKNOWLEDGEMENTS

First, I would like to express my sincere gratitude to Professor Talke, my academic advisor. With Professor Talke's mentorship, guidance, and support, I learned so much about interdisciplinary engineering and the importance of collaborations, and fundamental research. Professor Talke challenged me with ideas and projects that tested my ability to be resourceful, communicative, and how to think outside the box. After many decades of teaching and research, Professor Talke's enthusiasm and love for science continues to inspire many generations of students, allowing me to grow both personally and professionally during the Ph.D. program than I ever imagined. Without such great support, this dissertation would not have been possible.

Second, I would like to thank my committee members Professor Eric Fullerton, Professor Yeshaiahu Fainman, Professor James Friend, and Professor Michael Tolley. I also would like to express my gratitude to my managers, Michael Sullivan, Dr. Brian Karr, and Dr. Qing Dai for their guidance during my summer internships at Western Digital Corporation and Seagate Technology for the last four summers as well as when I was back at UC San Diego. I also would like to thank Dr. Andrey Ovcharenko, Dr. Sukumar Rajauria, and Dr. Erhard Schreck from Western Digital for their advice and support for my research.

I would like to extend my sincere thanks to Dr. Frederick Spada for fruitful discussions, research and experimental skills. Dr. Spada has always be my source of knowledge during my Ph.D. program whenever I had issue with the experimental setups or struggled to explain the experimental data. Dr. Spada's dedication, logical thinking,

persistence, and extreme hard work have never stop inspiring me to become a better researcher. I wish to thank to former and current Talke's members Dr. Liane Matthes, Dr. Alex Phan, Karcher Morris, Benjamin Suen, Phuong Truong, Buu Truong, Matthew Kohanfar, Dr. Guoqing Zhang, Christoph Schade, and Oren Gotlib. I am very lucky to communicate, learn, and discuss with them from different perspectives of research during my Ph.D. study.

I would like to also thank to CMRR's members Iris Villanueva, Marina Robenko, and Ray Descoteaux who were very big contributors to my success during the past several years due to their dedication and supportive roles. Thank you to Iris and Marina for all of her support and taking care of our lab space, finances, and grants. Thank you to Ray for spending the time to help me to develop many of the experimental apparatus used in the projects. Ray's knowledge, and technical skills were a cornerstone to making my experimental setups possible. Special thanks to the entire CMRR staff, you all have been wonderful to work with and I am really grateful for all of your contribution to our building.

Lastly, I would like to also thank my parents whose unconditionally support me during this journey. They had waited so long for me to finish my degree and see me to walk every steps to achieve my dreams. They have labored all of their lives and sacrificed so much to ensure my future and success. Thank you so much for your love, patience, perseverance, encouragement, support, and sacrifice.

Chapter 4, in part is a reprint of the material as it appears in "Effect of Air and Helium on the Head-Disk Interface during Load-Unload," Tan Trinh, Michael Sullivan, Sujit Kiperkar, and Frank E. Talke, *Tribology Letters*. The dissertation author was the primary investigator and author of this paper.

Chapter 5, in part is currently being prepared for submission for publication of the material. "Investigation of the Effect of Bias Voltages and Relative Humidity on Wear and Buildup at the Head-Disk Interface," Tan Trinh, Christoph Schade, Michael Johnson, and Frank E. Talke, submitted to *IEEE Transactions on Magnetics*, 2019. The dissertation author was the primary investigator and author of this paper.

Chapter 6, in part is currently being prepared for submission for publication of the material. "Laser Current Studies of Heat-Assisted Magnetic Recording", Tan Trinh, Sukumar Rajauria, Robert Smith, Erhard Schreck, Qing Dai, and Frank E. Talke, in preparation for submission to Microsystems Technologies, 2019. The dissertation author was the primary investigator and author of this paper.

Chapter 7, in part is currently being prepared for submission for publication of the material. "Temperature induced near field transducer (NFT) failure in heat-assisted magnetic recording (HAMR)," Tan Trinh, Sukumar Rajauria, Robert Smith, Erhard Schreck, Qing Dai, and Frank E. Talke, submitted to *IEEE Transactions on Magnetics*, 2019. The dissertation author was the primary investigator and author of this paper.

VITA

06/2011	Bachelor of Engineering in Applied Physics and Control Systems Saint-Petersburg State Polytechnic University, Saint Petersburg, Russia
2011 – 2012	Researcher, Academy of Science and Technology, Hanoi, Vietnam
2013	Department of Mechanical and Aerospace Engineering University of California, San Diego, La Jolla, CA, USA
01/2015	Master of Science in Engineering Sciences (Mechanical and Aerospace Engineering) University of California, San Diego, La Jolla, CA, USA
2014-2019	Teaching and Research Assistant at Department of Mechanical and Aerospace Engineering University of California, San Diego, La Jolla, CA, USA
06/2019	Doctor of Philosophy in Engineering Sciences (Mechanical and Aerospace Engineering) University of California, San Diego, La Jolla, CA, USA

PUBLICATION

Journal Papers

Tan D. Trinh, Sukumar Rajauria, Robert Smith, Erhard Schreck, Qing Dai, Frank E. Talke, "Optimal Laser Current Studies in Heat-Assisted Magnetic Recording", in preparation for submission to MicroSystems Technologies, 2019.

Tan D. Trinh, Sukumar Rajauria, Robert Smith, Erhard Schreck, Qing Dai, Frank E. Talke, "Temperature Induced Near Field Transducer (NFT) Failure in Heat-Assisted Magnetic Recording (HAMR)", submitted to IEEE Transactions on Magnetics, 2019.

Tan D. Trinh, Christoph Schade, Michael Johnson, Frank E. Talke, "Investigation of Bias Voltage and Relative Humidity on Wear and Nano-Corrosion of the Head-Disk Interface", submitted to IEEE Transactions on Magnetics, 2019.

Tan D. Trinh, Michael Sullivan, Sujit Kiperkar, Frank E. Talke, "Effect of Air and Helium on the Head-Disk Interface during Load-Unload", Tribology Letters, February, 2018.

Guoqing Zhang, Hui Li, Shengnan Shen, Tan Trinh, Fengliang He, Frank E. Talke, "Effect of Track-Seeking Motion on Off-Track Vibrations of the Head-Gimbal Assembly in HDDs", IEEE Transactions on Magnetics, vol. 54, issue 5, May, 2018.

Conference Papers

Tan D. Trinh, Frederick E. Spada, Christoph Schade, Michael Johnson, Frank E. Talke, "Voltage Biasing and Nano-Corrosion of the Head-Disk Interface", 2019 ASME Information Storage and Processing Systems, June 27-28, San Diego, CA.

Qin Zhao, Zijian Zeng, Tan D. Trinh, Christoph Schade, Frank E. Talke, "Investigation of Disk Runout in Air, Helium, and Vacuum", 2019 ASME Information Storage and Processing Systems, June 27-28, San Diego, CA.

Tan D. Trinh, Frederick E. Spada, Andrey Ovcharenko, Frank E. Talke, "Investigation of the Contact Potential of the Head-Disk Interface using Kelvin Probe Measurements", 2018 ASME Information Storage and Processing Systems, September 29-30, San Francisco, CA.

Tan D. Trinh, Michael Sullivan, Sujit Kiperkar, Frank E. Talke, "Effect of Air and Helium on the Head-Disk Interface during Load-Unload", 2017 ASME Information Storage and Processing Systems, September 29-30, San Francisco, CA.

Guoqing Zhang, Hui Li, Shengnan Shen, Tan Trinh, Fengliang He, Frank E. Talke, "Effect of Track-Seeking Motion on Off-Track Vibrations of the Head-Gimbal Assembly in HDDs", 2017 ASME Information Storage and Processing Systems, September 29-30, San Francisco, CA.

ABSTRACT OF DISSERTATION

Tribological Performance of the Head-Disk Interface in Perpendicular Magnetic Recording and Heat-Assisted Magnetic Recording

by

Tan Duy Trinh

Doctor of Philosophy in Engineering Sciences (Mechanical Engineering)

University of California, San Diego, 2019

Professor Frank E. Talke, Chair

International Data Corporation (IDC) estimates that hard disk drives will still be the main storage device for storing digital data in the next 10 years, holding approximately 80% of the data inside data centers. To increase the areal density of hard disk drives, the mechanical spacing between the head and disk surface has decreased to approximately 1nm. At such a small spacing, tribology of the head-disk interface, including head-disk contacts, wear, material buildup, and lubricant transfer, become increasingly more important for the reliability of hard disk drives. In addition to small spacing, heat-assisted magnetic recording (HAMR) technology aims to deliver higher areal density recording by heating up the media surface to a few hundred Celsius degrees, facilitating the writing process. High temperature at the head and disk surfaces cause serious reliability issues for

the head-disk interface (HDI). Therefore, understanding of the main factors that affect the reliability of the head-disk interface is an essential task.

In this dissertation, the effect of bias voltage and helium environment on the tribological performance of the head-disk interface is investigated. To do this, we first simulated the flying characteristics of the slider as a function of bias voltage in air and helium environment. Thereafter, an experimental study was performed using custom built tester located inside a sealed environmental chamber to study the effect of air and helium on wear and lubricant redistribution at the head-disk interface during load-unload. We investigated the effect of bias voltage and relative humidity on wear, material buildup, and nano-corrosion on the slider surface. Finally, we have studied laser current and laser optical power in heat-assisted magnetic recording as a function of operating radius, head-disk clearance, media design, and their effects on the life-time of the head-disk interface.

The results of this dissertation provide guidance for the effect of bias voltage, relative humidity, and helium environment on wear, material buildup, corrosion, and lubricant transfer at the head-disk interface. More importantly, our experimental study in heat-assisted magnetic recording leads to a better understanding of the main factors that cause failure of the HAMR head-disk interface. Our results are important for the improvement of the tribological performance and reliability of perpendicular magnetic recording (PMR) and heat-assisted magnetic recording (HAMR) head-disk interface.

Chapter 1

Introduction to Data Storage

1.1 Computer Memory

Computer memory, consisting of volatile and non-volatile memory, refers to physical devices that are capable of storing information in a computer. Volatile memory, abbreviated as VM, requires continuous electrical power to retain stored information, i.e., in the absence of power the data gets lost. Volatile memory is fast and considered as working memory in which operational instructions of the computer and real-time data of currently running programs are stored while the calculations are performed in the Central-Processing Unit (CPU). Popular volatile memory inside a computer includes SRAM (static random-access-memory) and DRAM (dynamic random-access-memory). DRAM uses a single capacitor and a single transistor within an integrated circuit to store data, allowing DRAM to be a space efficient and cost effective device. In SRAM, a cell of six transistors is used to store data instead of capacitors like in DRAM. Therefore, SRAM performs faster than DRAM and typically more expensive than DRAM. However, the requirement of continuous electrical power restricts volatile memory like SRAM and DRAM from being long-term storage devices.

In contrast to volatile memory, non-volatile memory or NVM is used as secondary storage or long-term storage devices, retaining data without electrical power [1]–[5]. Non-

volatile memory is categorized into mechanically-addressed and electrically-addressed memory. Typical examples of mechanically addressed systems are magnetic tapes, optical disks, floppy disks, hard disks, and holographic memory. In mechanically addressed systems, a contact structure or “head” is used to read and write data on the designed storage medium using magnetic or photosensitive materials. Electrically addressed systems feature Mask ROMs (read-only memory), PROMs (programmable read-only memory), EPROM (erasable programmable read-only memory), F-RAM (ferroelectric RAM), MRAM (magnetic RAM), and flash memory [1], [2]. Generally speaking, electrically-addressed systems are faster and more expensive than mechanically-addressed systems [3], [4]. Mechanically-addressed systems, like hard disk drives, currently offer the best cost per stored data compared to electrically-addressed systems [5]. In 2018, the price per terabyte of data stored in hard drives is approximately 10 times cheaper than that of the flash memory or solid state drives (SSD) as shown in Figure 1.1.

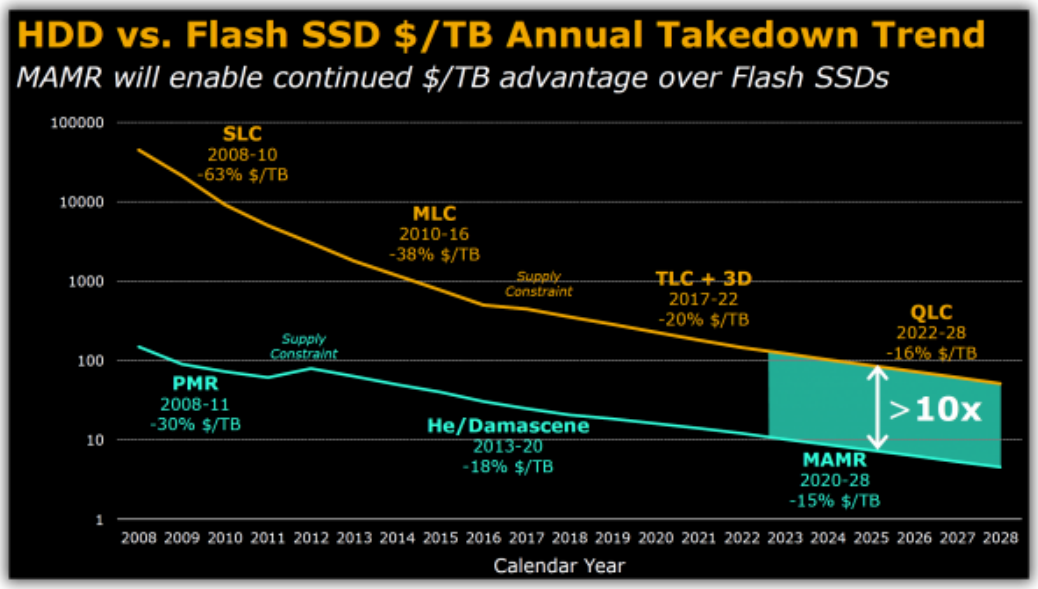

Figure 1.1 Cost per Terabytes of Hard Disk Drives vs. Flash Solid State Drives [5]

1.2 Data Growth in the Digital World

Recently, more data is created by humans than ever before and most of them is digitized and stored in the computer memory devices [6]–[8]. It is estimated that 2.5 quintillion (10^{18}) bytes of data are created every day according to research from IBM [6]. International Data Corporation, or IDC, estimates that worldwide data will grow annually 61% from 33 zettabytes (2018) to 175 zettabytes by 2025 [7]. The massive growth of data is due to the evolution of new technologies with rising of cloud computing, artificial intelligence (AI), machine learning, deep learning, data analytics (Big Data), 5G technology, and Internet-of-Things (IOT). Forbes estimated that 70 percent of enterprises will implement artificial intelligence in 2019 [8] that allows a company to have an insight look into the meaning of the data to make business decisions. For the last 5 years, data center has become an important tool for people to create, store and share data. Beginning in 2019, more data will be stored in the enterprise core than in all the world's existing endpoints and approximately 80% of the data in data centers will be stored in the hard disk drives, as predicted by IDC [7]. Clearly, hard disk drives storage plays an important role in the world of digital data. In near future, cost per stored data of the hard drives will keep getting cheaper compared to flash memory with new technologies such as shingled magnetic recording (SMR), microwave-assisted magnetic recording (MAMR), heat-assisted magnetic recording (HAMR), and heated-dot magnetic recording (HDMR).

1.3 History of Hard Disk Drives

Hard disk drives have had a long history of research and development. In 1956, the first commercial hard disk drive, named RAMAC (Random Access Method of Accounting

and Control) 305, was shipped by IBM (International Business Machines) Corporation [9]. The RAMAC 305 can store five million six-bit characters (which is equivalent to a total capacity of 3.75MB), costing approximately $10,000 per megabytes and was used primarily for U.S. military and wealthy private corporations. The areal density of the RAMAC 305 is equivalent to 2,000 bits per square inch (bits/in^2). The system featured fifty disks of 24 inches (~61cm) diameter, having the size of a large refrigerator. The RAMAC 305 weighed about one ton and was delivered via large cargo airplanes (Figure 1.2). In the RAMAC 305, the inductive read and write heads were flown above the disk surfaces at a distance of approximately 800 micro inches (~20 microns) using a hydrostatic forced air bearing.

Figure 1.2 IBM RAMAC 305 that weighed over a ton, and had to be transported by air plane [9]

In 1962, the IBM 1301 disk storage unit pioneered self-acting air bearing slider technology that allows a head to fly on a hydrodynamic air bearing caused by moving air [10]. This invention allowed a significant reduction of the distance between the head and the disk down to 250 micro inches (~6.35 microns). As a result, the areal density of the IBM 1301 disk drive increased to 26,000 bits/in^2 , a thirteen times increase compared to the IBM 305 system. In the same year, IBM introduced a removable disk drive, the IBM 1311, with 14 inches diameter disks and ferrite recording heads [11]. In 1965, a voice coil actuator motor was first employed to control the motion of the actuator arm [12]. In 1971, a track following servo system and a voice coil actuator were used, decreasing access time to 30 milliseconds [12]. Track following servos and voice coil actuator systems are still used in modern hard disk drives. In 1974, a new type of low-cost hard disk drive, the IBM 3340 or "Winchester" [13] drive, was introduced. This system used lubricated disks and low-mass recording heads located inside a sealed assembly (Figure 1.3). The Winchester hard drive allowed the read and write head to land on a dedicated zone on the disk surface upon spin-down. During the spin up of the disk, the head takes off and flies on the disk surface at a flying height of approximately 18 micro inches (~460 nanometers). The invention of the new "Winchester" head was considered by Al Shurgart, the co-founder of Seagate Technology LLC., as one of the four most significant developments [13] in the history of hard drives technology.

In 1979, thin-film technology using photolithography was used to fabricate recording heads of small size in IBM [14] by utilizing photo masking, etching, and deposition processes to build magnetic and non-magnetic thin films on ceramic substrates.

The reduction in size and mass of the recording head allowed the flying height of the slider to decrease 30% compared to the Winchester head design, to approximately 320 nanometers. Thin film technology initiated the development of magneto-resistive (MR) head technology, establishing the foundation for a significant increase of the areal density in the hard drives [15]–[17]. At early 1990, hard drive reached a milestone one gigabyte capacity for the first time. Together with a reduction in size of the recording head, the platter sizes were also reduced from 14 inches (360mm) to 8 inches (200mm), 5.25 inches (130mm), and 3.5 inches (95mm) in diameter in 1983. At present, the two most popular form factors of hard disk drives are 2.5” (65mm) and 3.5” (95mm) for enterprise and personal storage systems. It is likely that the 2.5” (65mm) form factor will disappear in the

near future because of the competition with solid state drives (SSDs). Power consumption of hard drives can be reduced significantly due to a reduction of the disk sizes.

Figure 1.3 IBM 3340 Hard Disk Drive that used low-cost, low-load, landing read and write heads with lubricanted disks [18]

Another important milestone of the hard drive industry was the development of magneto-resistive (MR) read elements in which the resistance changes as a result of changing magnetic field [17]. In 1990, the first hard disk drive, the IBM 9345, with thin film magneto-resistive heads was introduced by IBM (Figure 1.4). In 1997, IBM started selling hard drives using giant-magneto-resistive (GMR) heads that reached an areal density of 1 Gigabits per square inch (Gbits/in^2). In GMR read elements, alternative layers of ferromagnetic and non-magnetic materials are placed next to each other [16], [17].

Depending on the parallel or anti-parallel alignment of the ferromagnetic layers, the electrical resistance of the GMR read sensor changes significantly. The resistance is low for parallel alignment and high in the case of antiparallel alignment [17]. Albert Fert and Peter Grunberg were awarded the Nobel Prize for the discovery of the giant-magneto-resistance (GMR) effect in 2007. In addition to GMR, tunneling magneto-resistance (TMR) was developed in 2004 that can also be used in magnetic recording technology [19]. The only difference between GMR and TMR is that the metallic non-magnetic layer in a GMR head is replaced by an insulator, the so-called tunnel barrier, in TMR. The insulator layer is designed to be very thin, allowing electrons to tunnel from one ferromagnetic layer to another ferromagnetic layer. Similar to the GMR, the electrons are likely to tunnel through a thin insulator layer when the ferromagnetic layers are parallel compared to the case when the ferromagnetic layers are antiparallel.

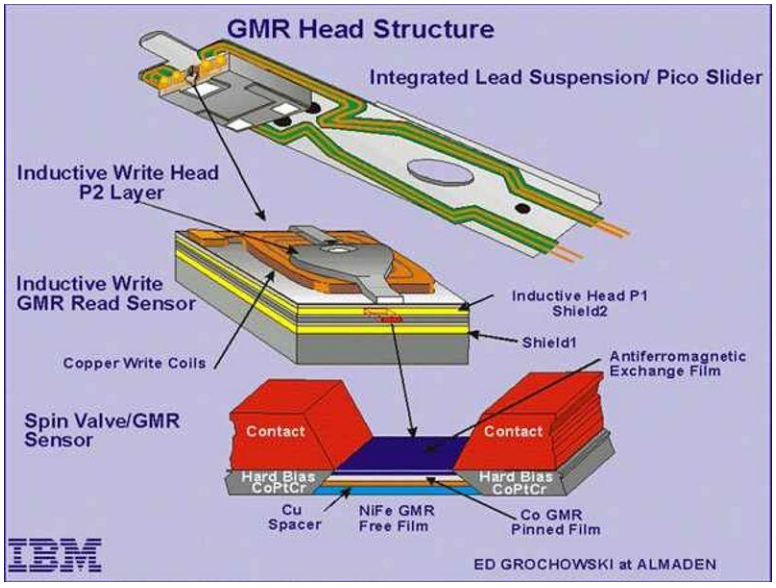

Figure 1.4 Recording head structure with inductive write element and GMR read sensor [20], [21]

In the magnetic recording technology, the transition from longitudinal magnetic recording to perpendicular magnetic recording marks another milestone. In perpendicular magnetic recording, the orientation of the magnetic grains on the disk surface allows the areal density on the hard disk drives to increase by more than tenth fold compared to the longitudinal magnetic recording [22]–[28]. Perpendicular magnetic recording technology yielding an areal density of 100 gigabits per square inch (100Gbits/in^2) was first introduced by Seagate in 2002 [26]. Currently, perpendicular magnetic recording is approaching 1 terabits per square inch (1Tbits/in^2) and will soon reach a physical limit, the so-called "superparamagnetic" limit [28], [29]. To overcome the superparamagnetic limit, new technologies such as shingled magnetic recording (SMR), microwave-assisted magnetic recording (MAMR), heat-assisted magnetic recording (HAMR), bit pattern media (BPM), and two-dimensional magnetic recording (TDMR) are under development that potentially increase the areal density of the hard drives to reach 10 terabits per square inch (10Tbits/in^2) [29].

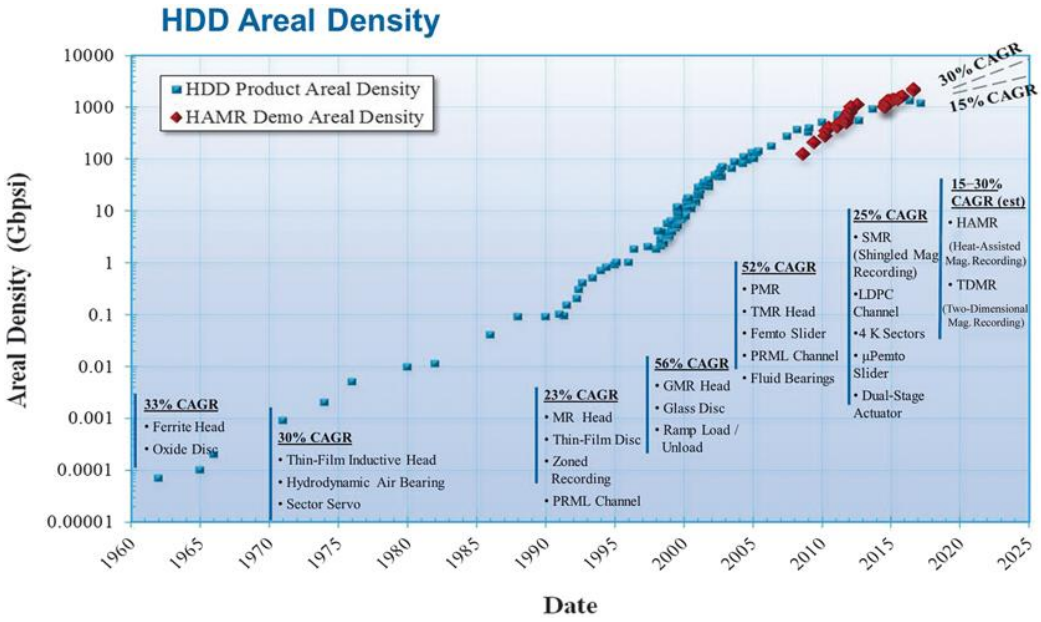

Figure 1.5 Hard Disk Drive (HDD) areal density increases at an average of 30% for the last five decades. The areal density of the hard disk drive is expected to keep increasing with the development of Microwave and Heat-Assisted Magnetic Recording (MAMR/HAMR) [29]

1.4 Recording Technologies in Hard Disk Drives

Data on hard disk drives is recorded by magnetizing a thin film of ferromagnetic material, made of granular Cobalt-Chrome-Platinum (Co-Cr-Pt), on the disk surface [30], [31]. In modern hard disk drives, the magnetic film is approximately 15-20 nanometers thick and composed of isolated crystalline grains with inter-granular nonmagnetic chromium and oxide materials boundaries as shown in Figure 1.6.

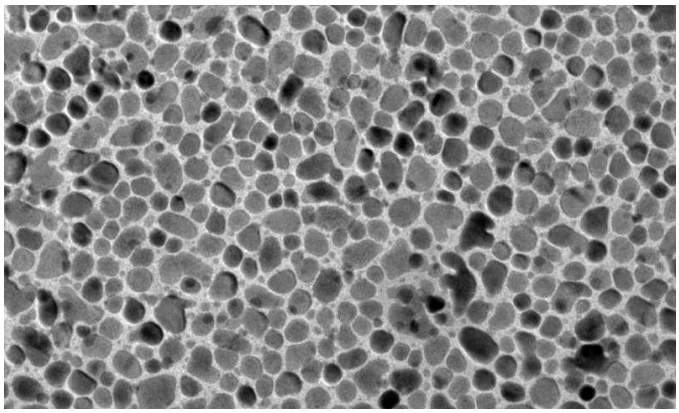

Figure 1.6 Granular magnetic grains on the disk surface. Boundaries of the grains are made of nonmagnetic chromium and oxide materials. [32]

To read and write data on the disk surface, a slider containing read and write elements is designed to fly on an air film [31]. Inside the slider, an inductive write element is used to create a strong magnetic field by applying an electrical current through the write coils. A magnetic flux is generated that flows through the magnetic core and penetrates the magnetic medium, orienting the magnetic grains on the disk surface [33], [34]. This process is called magnetization process, or writing process (Figure 1.7).

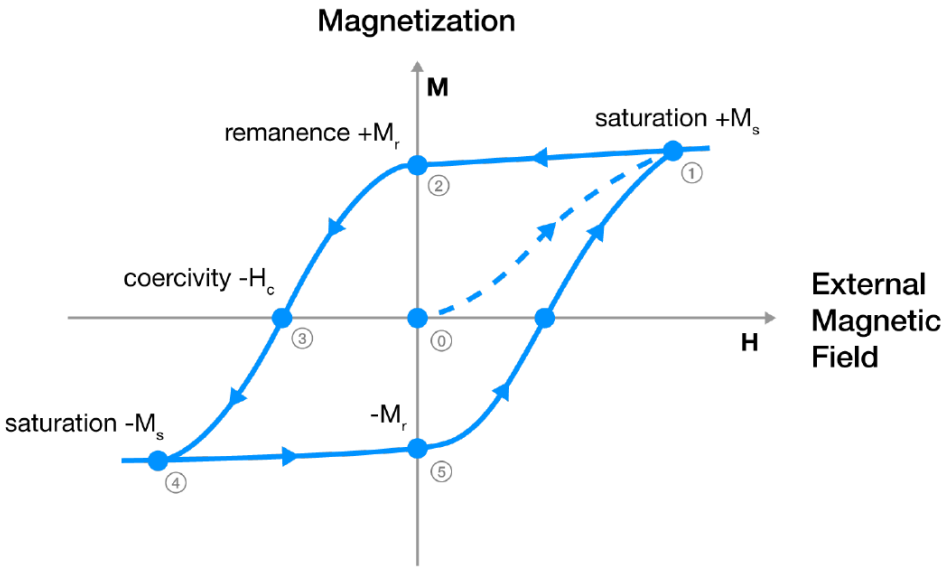

Figure 1.7 A hysteresis loop during the writing process. Remanence magnetization $+M_r$ and $-M_r$ correspond to two stable states in hard disk drives (0s and 1s) while the external magnetic field is removed. [33]

For ferromagnetic materials, the magnetization M is a strong function of the magnetic field H from the write element. In the absence of a magnetic field (point 0), the magnetic dipole moments of the material are disoriented, i.e. the magnetization of the material is zero or the material is not magnetized. When the applied magnetic field increases, the magnetic dipole moment orients into the same direction, leading to an increase of the material magnetization until reaching a saturation level $+M_s$ (point 1). Removing the magnetic field in the opposite direction after the saturation reduces the magnetization of the material to $+M_r$, the so-called a remanent magnetization or remanence (point 2). The remanent magnetization of the magnetic grains allows data to be stored on the disk surface when electrical power is removed. A further decrease of the magnetic field H eventually demagnetizes the material (point 3). The magnetic field that is required to demagnetize the material is called the coercivity H_c of the material. Ferromagnetic materials are called magnetically hard or magnetically soft depending on the magnitude of the coercivity of the materials, i.e., on how strong of a magnetic field is required to demagnetize the materials. When the magnetic field in Fig. 1.7 decreases further the opposite state of saturation $–M_s$ is reached when the magnetic dipole moment is oriented into the opposite direction (point 4). Increasing the magnetic field from saturation at point 4 causes another state of magnetization of the magnetic grains on the disk surface (point 5). The magnetization and demagnetization process is called the magnetic hysteresis loop [33]. The two points $+M_r$ and $–M_r$ in Figure 1.7 represent the two stable states (denoted as 0s and 1s) of the magnetic material in the absence of a magnetic field. In hard disk drives, the bit length of recorded magnetization is defined by the sharpness of the write field. A

shorter bit length is obtained if the flying height of the slider above the disk surface is decreased [34].

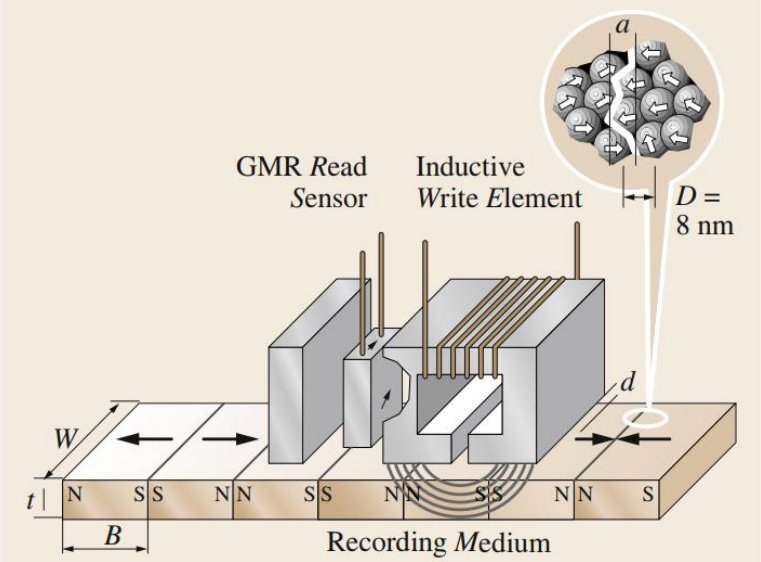

Figure 1.8 A schematic of read and write transducer of the slider [26]

After data is written on the disk surface, the recorded information is read back by sensing the fields emanating from the magnetization transitions (Figure 1.8). Since the width of the magnetic domains is on the order of tens of nanometers in the down track direction, the fields are very weak and highly sensitive materials are required to sense these magnetic fields. Magneto-resistive (MR) [16], giant-magneto-resistive (GMR) [17], and tunnel-magneto-resistive (TMR) [19] materials are materials such that their electrical resistance property changes as the magnetic field changes. The giant-magneto-resistive (GMR) effect was discovered by Albert Fert and Peter Grunberg. This effect is being used in the magnetic recording industry for read elements. The GMR read element is made by sandwiching two layers of ferromagnetic materials of different ferromagnetic properties and a conductor layer [20], [35]–[37] as shown in Figure 1.9. As the read element is exposed to the stray magnetic field, the magnetic direction of the free film layer changes, resulting in a resistance change of the read element by approximately 10% or more.

Measurements of the electrical current between the two ferromagnetic layers (free film and pinned film) allows the detection of magnetic transitions on the disk surface.

Thin film technology improvements of the read and write elements, and the transition from longitudinal magnetic recording (LMR) to perpendicular magnetic recording (PMR) have had a big impact on the increase in areal density [23]–[26], [36], [38]. Since 1956, the areal density has increased by almost eight orders of magnitude from 2,000 bits/in^2 to 1 Terabits/in^2 [38]. In order to continue the increase of areal density, new technologies are presently under development such as shingled magnetic recording (SMR), energy-assisted magnetic recording (HAMR, MAMR), and bit-patterned media (BPM) recording.

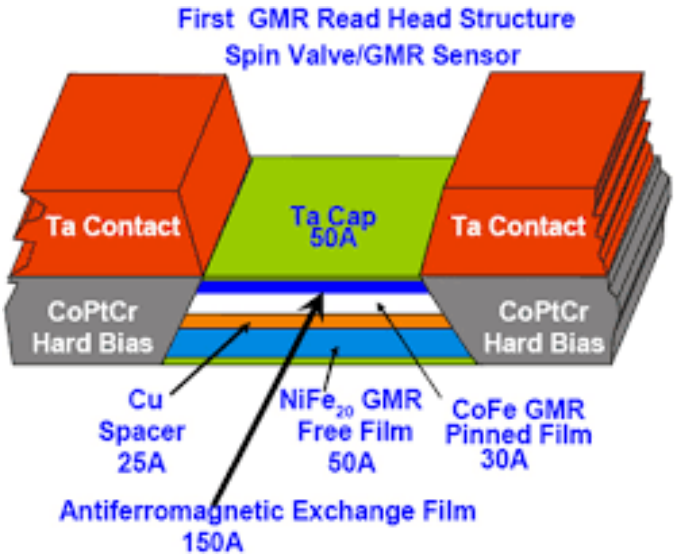

Figure 1.9 A schematic of the first giant-magneto-resistive (GMR) sensor [21]

1.4.1 Longitudinal Magnetic Recording (LMR) and Perpendicular Magnetic Recording (PMR)

For nearly 50 years until 2006, the disk drive industry has focused on longitudinal magnetic recording (LMR). In longitudinal magnetic recording, the bit magnetization on

the disk surfaces is parallel to the disk surface as shown in Figure 1.10(a). However, longitudinal magnetic recording has limitation in terms of the areal densities that can be achieved, i.e., approximately 100-200 Gigabits/in^2 [22]. Perpendicular magnetic recording (PMR) provides a platform for a continuous expansion of areal densities up to 1 Terabit/in^2 [23]–[25]. Magnetization of each data bit in perpendicular magnetic recording is aligned out-of-plane, i.e., perpendicular respect to the disk surface (Figure 1.10(b)). The areal density of longitudinal magnetic recording is limited due to fundamental limits. As the recording areal density increases, repulsive forces occur between the recording bits (magnets) of different magnetization leading to increasingly unstable bits (Figure 1.10(a)). In contrast to the longitudinal magnetic recording, the recorded bits in perpendicular magnetic recording mutually attracts each other, making it appropriate for high areal density recording [26].

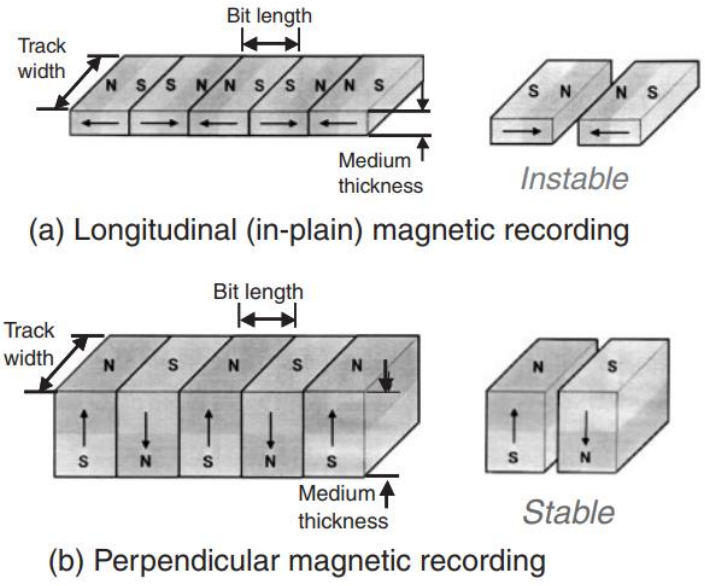

Figure 1.10 Longitudinal and perpendicular magnetic recording [39]

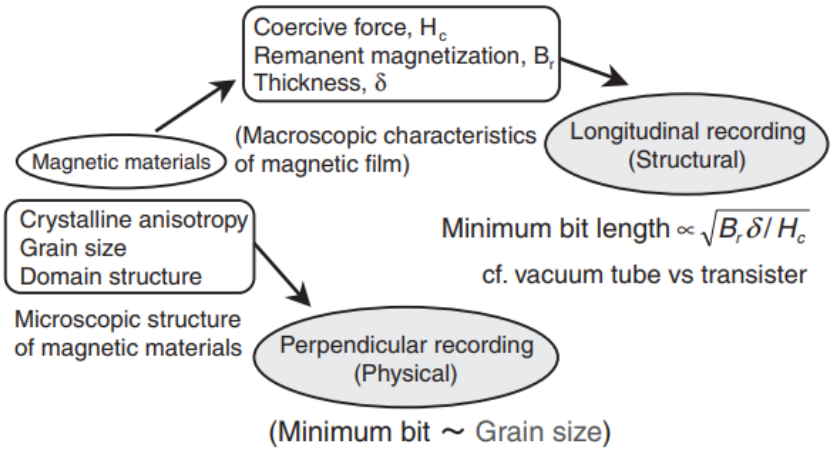

Figure 1.11 Longitudinal and perpendicular magnetic recording areal density limitation [39]

In addition to the magnetic grain orientation, the minimum bit length of longitudinal magnetic recording is a strong function of the thickness of the magnetic layer δ as shown in Figure 1.10 [26], [27]. An increase of the areal density requires a further decrease of the thickness of the magnetic layer. This implies that the volume of the magnetic grain decreases, thereby resulting in the so-called "superparamagnetic" limit [27], [28]. In the superparamagnetic limit, a reduction of the magnetic volume decreases the thermal stability of the recorded data, i.e., the recorded bits on the disk surface can be demagnetized due to temperature fluctuations. Clearly, an increase in the thickness of the magnetic layer as in perpendicular magnetic recording (PMR) allows an increase in the amplitude of the read-back signals compared to the longitudinal magnetic recording (LMR), providing a benefit of packing more data on a given disk area. In addition, the existence of a magnetically soft under-layer (SUL) [27] located under the recording layer in perpendicular magnetic recording increases the effective write field, enabling an increase in the coercivity of the magnetic media. This is very important for the improvement of thermal stability of the recorded data on the disk surface.

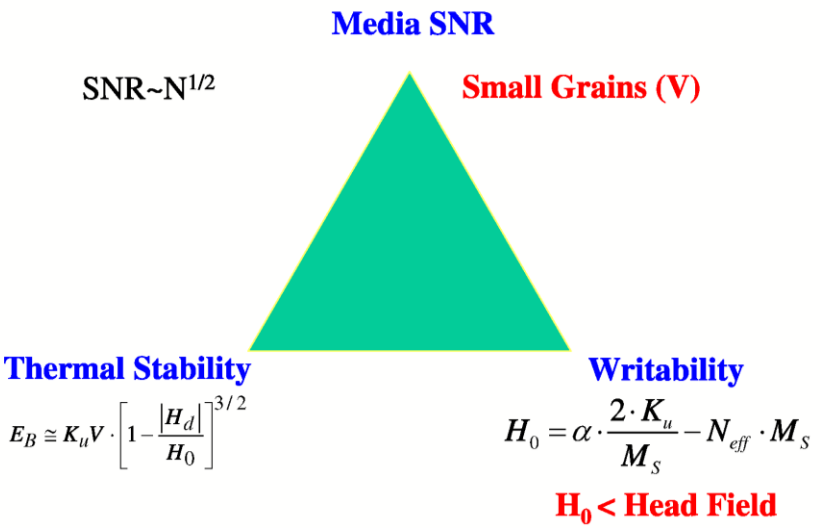

Figure 1.12 Media design constraints "Trilemma" [40]

It is important to note that the introduction of perpendicular magnetic recording delays the occurrence of the superparamagnetic limits, although it does not prevent it. Currently, perpendicular magnetic recording is approaching physical constraints between media signal-to-noise ratio, thermal stability of magnetic grains, and writing capability. These physical constraints are called the media design "trilemma" as shown in Figure 1.12. To increase the areal density, the magnetic grain size needs to be reduced by using highly magneto-crystalline anisotropic materials. This results in an increase of the anisotropy field of the medium, thereby leading to an increase of the material coercivity [28]. This implies that the write field from current inductive write elements is no longer strong enough to write data on the media. Shingled magnetic recording (SMR), energy-assisted magnetic recording (HAMR and MAMR), and bit patterned media (BPM) are different technologies that aims to keep increasing the areal density of the hard drives in the future. These technologies will be discussed in the following sections.

1.4.2 Shingled Magnetic Recording

Shingled magnetic recording (SMR) is a technology that is used to provide an increase of the areal density by approximately 16% compared to conventional magnetic recording [32], [41]–[45]. In conventional recording, a small gap is present between two adjacent tracks to account for track misregistration of the recording head. This gap is removed in shingled magnetic recording technology, allowing more tracks to be placed on the same area so that data can be packed more densely on the disk surface (Figure 1.13). In shingled magnetic recording the width of the write element is increased compared to conventional magnetic recording, producing a stronger magnetic field that can be used to write data on high coercivity materials on the disk surface [43], [45]. Materials with high coercivity allow smaller magnetic grains, which leads to an increase of the areal density on the disk surface.

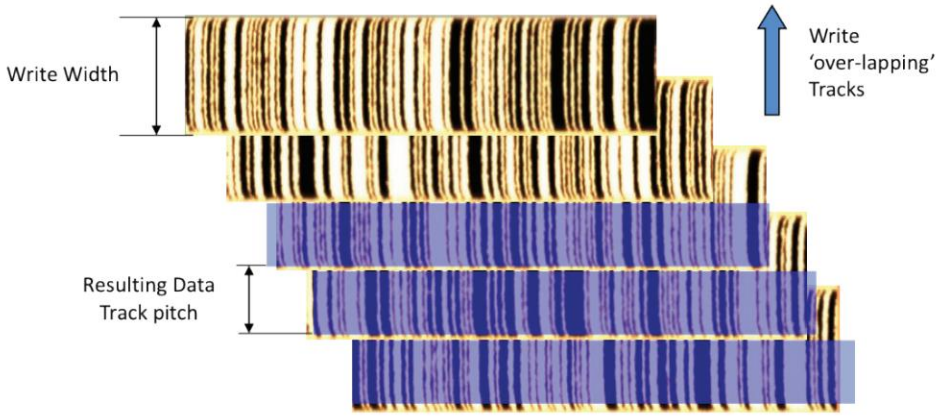

Figure 1.13 A schematic of shingled magnetic recording (SMR) [44], [45]

The advantage of shingled magnetic recording comes with several drawbacks. Because part of the written data needs to be erased and rewritten sequentially if a particular track needs to be modified, the writing process is slower compared to the conventional magnetic recording [44]. A random writing process in shingled magnetic recording also

causes data fragmentation to increase compared to conventional recording. Fragmentation of data results in an increase of data access time during both the read and the write operations. Thus, shingled magnetic recording is a good fit for archival data storage in data centers rather than for use in real time applications. It is estimated that by 2023, shingled magnetic recording will be used by approximately 50% in data center hard drives [46].

1.4.3 Energy-Assisted Magnetic Recording

Energy-assisted magnetic recording is a new technology that aims to increase the areal density of hard disk drives up to 10Tbit/in^2 [47]–[50]. In energy-assisted magnetic recording technology, magnetic recording media with magnetic materials of very high coercivity is used for recording. The advantage of high coercivity materials is that they have high enough magnetic energy barrier that protects magnetic grains from being flipped due to the thermal fluctuation. High energy barrier, however, prevents data to be written on a disk surface using a conventional write head because the inductive magnetic write field is not strong enough to change the magnetization of the ferromagnetic materials on the disk surface. In energy-assisted magnetic recording, external energy is added during the writing process to temporarily reduce the coercivity of the magnetic layer, allowing data to be written on the disk. External energy can be in the form of microwaves, the so-called microwave-assisted magnetic recording (MAMR) [47], [48], or in the form of heat, the so-called heat-assisted magnetic recording (HAMR) [49]–[53]. MAMR may also stand for microwave-assisted magnetization reversal that was proposed in 1970s and rediscovered by different research groups in 2000s [47]. In MAMR, an AC field is generated using a perpendicular spin torque oscillator (PSTO) that is incorporated into the

write element of the recording head as shown in Figure 1.14. A microwave signal is emanated having a frequency from 20-40 GHz that matches the resonance frequency of the recording medium. Because of this, a resonance effect occurs that lowers the resistance of the underlying layer on the recording media, thereby allowing the direction of magnetic grains to tilt about their vertical axis. MAMR is shown to improve the "effectiveness" of the write field by approximately 3 to 4 times while requiring only a fraction of the power consumption.

Figure 1.14 Schematic of microwave-assisted magnetic recording (MAMR). A spin torque oscillator (PSTO) is incorporated into the write element to deliver energy in form of AC field to the disk surface. Thus, the areal density of a MAMR drive can be increased up to 4TB/in^2 [5]

Heat-assisted magnetic recording (HAMR) utilizes external energy from heat for the magnetization reversal. In HAMR, optical power is delivered from a laser diode through a waveguide and coupled to the near-field transducer (NFT) as shown in Figure 1.15. At a particular laser wavelength, surface plasmonic effects or surface charge

oscillations occur and accumulate at the small tip of the near-field transducer. This procedure produces an evanescent wave that couples into the media surface and generates heat [51]–[53]. The final shape of the heated spot size depends on the design of the near-field transducer [53], the layers on the media surface [51], and their distance. By heating the media surface to the Curie temperature of a few hundred Celsius degrees, the coercivity of the magnetic layer is temporarily reduced to near zero, allowing the write element to switch the direction of the magnetic grains using currently available inductive write elements. During the cool down of the temperature within nanoseconds after writing, the magnetization is frozen in the disk in the desired orientation. By doing so, data are written on the disk surface within nanoseconds. This is equivalent to data rate of current perpendicular magnetic recording technology. However, high energy density and an extreme high temperature of the head-disk interface pose critical reliability issues on heat-assisted magnetic recording [54].

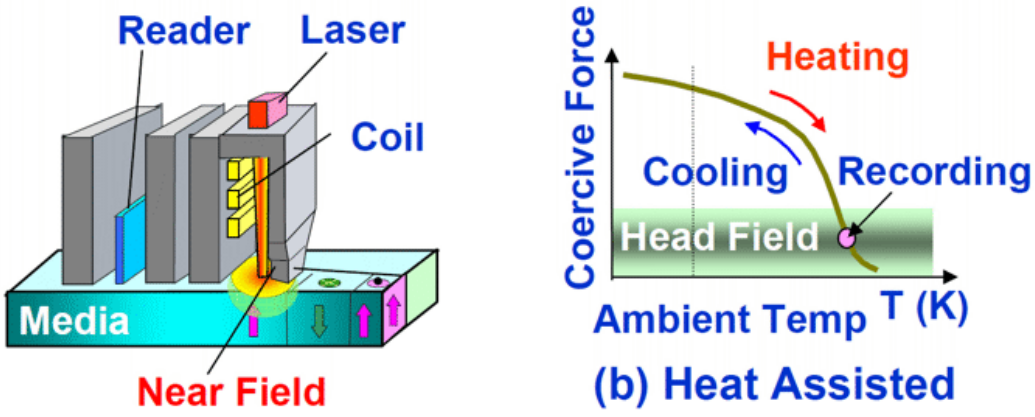

Figure 1.15 A schematic of heat-assisted magnetic recording (HAMR). A laser diode is incorporated on the top of the slider to deliver optical energy to the disk surface [51]

Although microwave-assisted magnetic recording (MAMR) and heat-assisted magnetic recording (HAMR) are different approaches, they both promise to improve the areal density multiple times compared to present perpendicular magnetic recording (PMR). Thus, both techniques will increase the total capacity of hard drives in the near future. To further increase the areal density, additional approaches including bit-patterned magnetic recording and a combination of heat-assisted magnetic recording and bit-patterned magnetic recording have been proposed (Fig. 1.16).

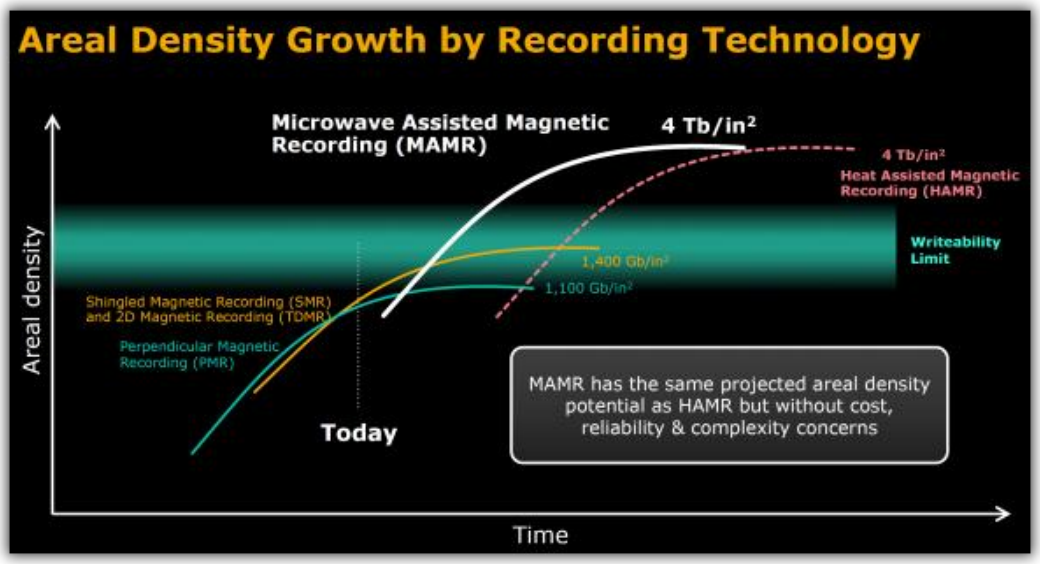

Figure 1.16 A roadmap of the areal density growth of perpendicular magnetic recording, shingled magnetic recording, microwave-assisted magnetic recording, and heat-assisted magnetic recording [42]

1.4.4 Bit-Patterned Media Recording

In conventional magnetic recording, a thin film of granular magnetic grains is used to stored data. Currently, an average of 20 to 30 grains are used to store one bit of data [23]. Since the signal-to-noise ratio (SNR) of the read-back signal is linearly proportional to the square root of the number of the magnetic grains N_{grains} for storing one bit, i.e.,

$SNR \sim \sqrt{N_{grains}}$, the grain size needs to be decreased to maintain an adequate signal-to-noise ratio value while increasing the areal density. Decreasing the magnetic grain leads to thermal instability of the grain, causing spontaneous magnetic flipping or loss of data due to thermal fluctuation. The jaggedness of the magnetization transition that is caused due to the non-uniformity of magnetic grains on the disk surface decreases the thermal stability of magnetic grains. Bit-patterned media is a widely accepted solution to increase the thermal stability of high areal density disk besides energy-assisted magnetic recording. In bit-patterned media, a regular array of uniform magnetic cells is formed on the disk surface (Figure 1.17) instead of a granular magnetic domain in conventional recording [55]–[58]. In bit patterned media recording, each bit is stored in a magnetic cell with non-magnetic grooves that is shown to eliminate transition noise caused by the jaggedness of the granular magnetic domains. More importantly, the volume of each magnetic cell is larger than the magnetic grain volume. This increases the energy barrier for demagnetization, or thermal stability of the magnetization. Therefore, a small diameter bit pattern is allowed for high density recording while maintaining thermal stability.

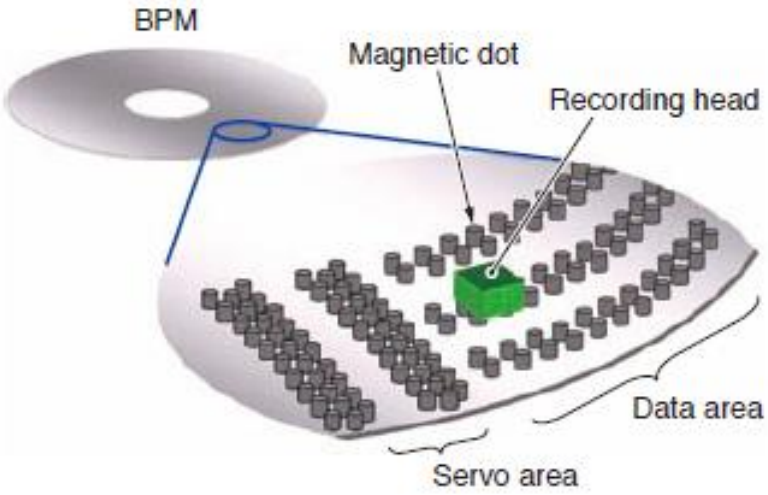

Figure 1.17 Bit-patterned media recording [58]

Magnetic cells on bit-patterned media surface have been fabricated using patterning generation and etching methods [58]. The patterning generation is accomplished with lithography methods (electron-beam, optical, or imprint) using ion-resist materials and stencil masks. Afterwards, magnetic material is deposited onto the pattern by electrodeposition or evaporation. As a result, different combinations of magnetic cells are formed on the disk surface. Using lithography technology allows fabrication of magnetic cells as small as 10nm in diameter, equivalent to an areal density of 5Tbit/in^2. However, fabrication of such small nanostructures over a large area is extremely challenging and expensive. Nano-imprinting, laser interference lithography, and self-assembly patterning have been proposed for large manufacturing of ultra-high density hard drives. Besides cost limitation, small magnetic cells on bit-patterned media require servo tracking improvements during the seeking process compared to conventional magnetic recording. A closed-loop feedback control is required to sample magnetic and location of patterned bits [59]–[61]. It has been proposed that combining bit-patterned magnetic recording and energy-assisted magnetic recording can deliver areal density of up to 10Tbit/in^2 [5].

1.5 Dissertation Objective

The objective of this dissertation is to perform experimental and numerical investigations that aim to improve the tribological performance of the head-disk interface in perpendicular magnetic recording (PMR) and heat-assisted magnetic recording (HAMR) technology. As the head-disk spacing in present day hard disk drives is less than one nanometer, our work focuses on the effects of helium, head-disk interface bias voltage, and relative humidity on wear, material buildup, and lubricant redistribution on the head-disk

interface. Recently, heat-assisted magnetic recording technology has been investigated as a potential technology to increase the areal density of hard disk drives. In this study, we investigate laser current as a function of radius, head-disk clearance, media properties, and their effects on the life-time of the head-disk interface in heat-assisted magnetic recording.

1.6 Organization of Dissertation

Chapter 1 provides an overview of computer memory, including volatile (VM) and non-volatile memory (NVM), and the growth of digital data during the period from 2010 to 2025. Among the available computer storage devices, hard disk drives are the mainstream for storing data especially in data centers due to a low cost per storage benefit. The history and the most prominent technologies in hard disk drives industry are presented.

Chapter 2 introduces main components of the hard disk drives. An overview of tribology of the head-disk interface, including diamond-like carbon and lubricant layers that are used to protect the head-disk interface, is presented. In addition, the effect of helium on the tribology of the head-disk interface is discussed. Finally, different measurement techniques that have been used to measure the head-disk spacing are shown, including optical interferometry and electrical methods.

Chapter 3 presents numerical simulation of the thin air bearing film between the head and the disk surfaces. The Reynolds equation and equilibrium equations of the slider are discussed. The equations are solved simultaneously using finite element analysis to study the flying characteristics of sliders on the disk surface. In this study, the effect of Van-der-Waals and electrostatic forces on the flying characteristics of sliders are shown in air and helium environment.

In *chapter 4*, the effects of air and helium on wear on the slider surfaces and lubricant redistribution on the disk surfaces are investigated. Experimental results show that wear and lubricant redistribution of the head-disk interface are significantly decreased in helium compared to in air environment.

Chapter 5 studies the effect of bias voltage and relative humidity on wear and material build-up at the head-disk interface. Atomic force microscopy (AFM) is used to study wear and material build-up on the slider surfaces. Experimental results show that wear is decreased in the presence of negative bias voltage compared to the case when a positive bias voltage is applied. Pit formation was observed at high relative humidity at positive bias voltage. Different mechanisms, including the presence of pre-existing pits, electrical breakdown, or stray current corrosion, seem to be the cause for the formation of pits.

Chapter 6 shows the effects of operating radius and head-disk clearance on the optimal laser current of a heat-assisted magnetic recording (HAMR) head. The effect of media properties on the optimal laser current is studied. Experiment results show that the optimal laser current increases if the operating radius and head-disk clearance increase. Adding an additional layer on the top of the media surface, the so-called a “capping” layer can decrease the optimal laser current by approximately 15%.

Chapter 7 demonstrates a novel experimental setup to study life-time of heat-assisted magnetic recording (HAMR) head-disk interface as a function of laser current and laser optical power. Our study shows that life-time of heat-assisted magnetic recording (HAMR) decreases exponentially as the laser optical power increases. Optimizing the laser current and its efficiency to heat up a nanometer scale region on the disk surface is

important for improving the reliability of the head-disk interface in heat-assisted magnetic recording.

Chapter 8 presents a summary of the dissertation together with concluding remarks. Future directions of the study are provided with suggestions with regards to how the tribology of the head-disk interface is improved using helium and bias voltage study. In addition, application of bias voltage for heat-assisted magnetic recording (HAMR) head-disk interfaces is discussed.

Chapter 2

Introduction to Hard Disk Drives (HDDs)

2.1 Main Components of Hard Disk Drives

The main components of hard disk drives are the disk enclosure, the disks mounted on a fluid bearing spindle, the voice coil motor, the actuator arm that carries the read and write elements, the load-unload ramp, the air filter, and the circuit board (Figure 2.1). The fluid bearing spindle, located on the right side of the Figure (2.1), is used to rotate the disks. The rotational speed of the disks is important for the access time, mechanical performance, and power consumption of hard disk drives. Increasing the rotational speed of the disks from 5400rpm to 15000rpm decreases the data access time from 15ms to 9ms [62]. Access time is related to rotational latency time, i.e. the time it takes for the spinning disks to bring a particular disk sector under the read write elements for the read and write operations [62], [63]. An increase in the rotational speed of the disk leads to an increase in the power consumption [63] of the hard drive and the so-called "repeatable and non-repeatable runouts" of the disks [64]–[69]. The repeatable runout consists of low frequency disk vibrations and is related to imperfections of the spindle and mounting mechanisms [66], [67]. The repeatable runout can be compensated using feed-forward controls [66], [67]. On the other hand, non-repeatable runout is a flow-induced vibration and is a strong function

of the rotational speed, the number of disks, and the gas composition inside the hard drive enclosure [64], [65]. In modern hard disk drives, helium is used instead of air to reduce turbulence effect, leading to a decrease of the non-repeatable runout and track mis-registration of hard drives [42], [70]. In addition to increasing the rotational speed, adding more disks inside the hard drive enclosure increases the total capacity of the drive. Capacity is very important for data centers. Thinner and stiffer glass media have recently replaced conventional aluminum media that maintain adequate levels of repeatable runout during the operation of a hard drive [71]. Clearly, adding more disks increases the power consumption. Finding optimal conditions for the mechanical performance, total capacity, access time, and power consumption of a hard disk drive is a critical task.

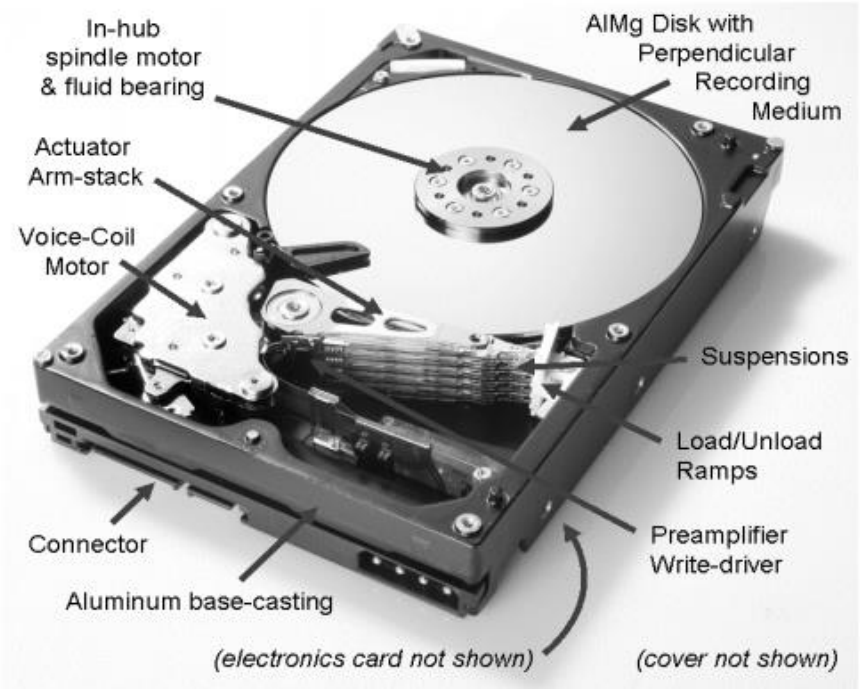

Figure 2.1 Main components of a hard disk drive without top cover [72]

On the left side of Figure 2.1, an actuator arm and a voice coil motor are shown. As presented in section 1.3, the actuator arm is rotated about the pivot using a voice-coil motor, allowing the slider to get access to the whole area of the platter surface. The design of the

voice-coil motor is similar to that of a loudspeaker, consisting of a coil inside a magnetic field generated by two permanent magnets. Controlling the direction and magnitude of the current that flows through the coil controls the Lorentz force that is used to move the actuator arm. A first prototype of a voice coil actuator system was built in 1965 and is still used in present hard disk drives [12]. E-block and heads suspensions, that carry sliders with recording heads, are located near the end of the actuator arm. The sliders are made of ceramic materials (Alumina Titanium Carbide (Al_2O_3-TiC) and are mounted on the suspension using a gimbal-dimple interface mechanism as shown in Figure 2.2. The mechanism allows free movement of the slider in three directions with respect to the suspension, including pitch angle (α), roll angle (β), and vertical displacement (h). The slider surface is etched to form a hydrodynamic air bearing surface. During the operation of the disk drive, an air bearing caused by the shear forces in the fluid film between the slider and the disk lifts the slider to fly on the disk surface. The air bearing surface is designed so that the lift forces and moments caused by the air pressure distribution on the slider surface are in equilibrium with the pre-load from the suspension that apply to the slider, allowing the slider to fly at a few nanometers. The pressure distribution at the head-disk interface is calculated using the Reynolds equation and slider equilibrium equations, to be presented in chapter 3. The read element and write coil are located at the trailing edge of the recording head. The read and write transducers are used to read and write information in concentric tracks on the disk surface.

During the power-off period of a hard drive, the air bearing disappears and the slider is either parked on a designated area on the disk surface [73], or is moved away from the

disk surface and parked on the ramp [74]. In modern hard disk drives, ramp load-unload is used predominantly because it protects the disk from wear, scratches, and lubricant pickup caused by contacts between slider and disk surfaces. Other main components inside the hard drive enclosure includes an air filter and a circuit board. The air filter is made of fibrous materials and used to prevent contamination from the environment to the hard drive enclosure. A circuit board is used to talk to the computer central processing unit (CPU) for the reading and writing operations. Our studies focus on the interface between the slider and the disk surfaces, the so-called head-disk interface (HDI), of hard drives.

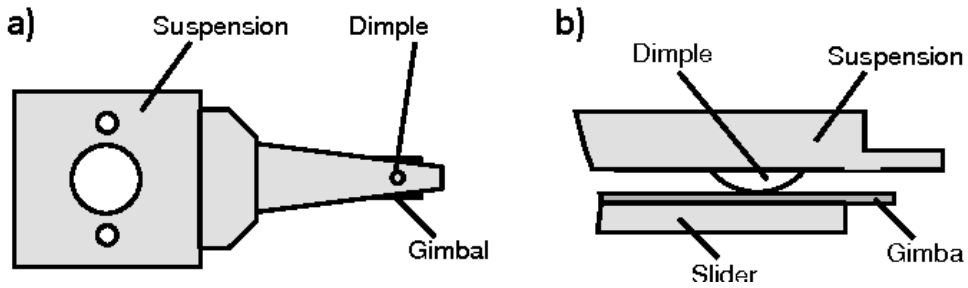

Figure 2.2 A schematic of the actuator arm, suspension, and slider. The slider is mounted on the suspension using a dimple-gimbal interface, allowing the slider to move freely in three degree of freedoms. [75]

2.2 Head-Disk Interface of Hard Disk Drives

In hard disk drives, the recording head is flown on a cushion of air on the top of the disk surface to read and write information. In current hard disk drives, the minimum distance between the slider and the disk is approximately 1nm during read and write operations. At such a small spacing, intermittent contacts between the head and disk are unavoidable, causing wear, scratches, and corrosion on the slider and disk surfaces [76]–[78]. To protect the head-disk interface from wear and corrosion, a thin diamond-like

carbon overcoat layer of approximately 2-3nm is coated on both the slider and media surfaces, respectively [79]. A thin lubricant layer of 1-2nm on the top of the disk carbon overcoat is used to protect the overcoat layer [80]. A schematic of the head-disk interface is shown in Figure 2.3.

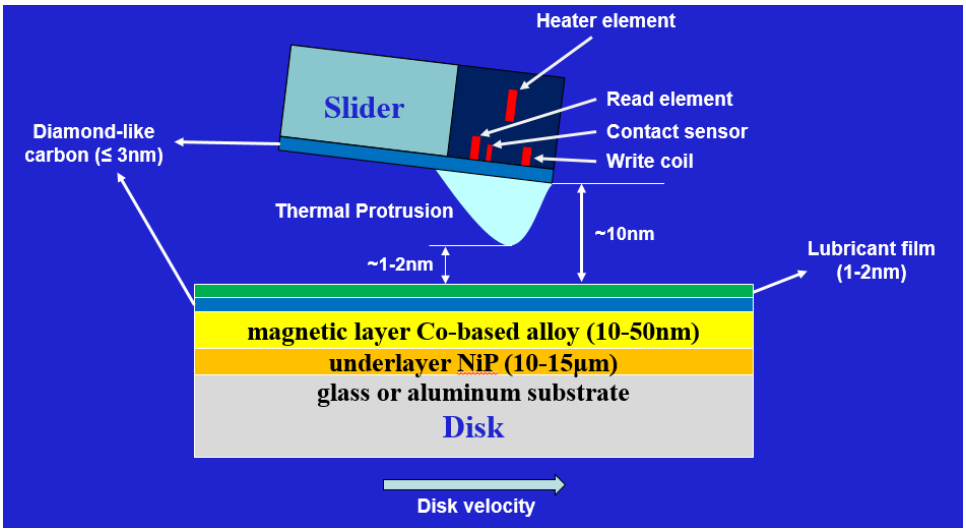

Figure 2.3 A schematic of the head-disk interface (HDI).

The spacing between the read and write transducer and the magnetic layer on disk surfaces (the so-called head-media spacing) is critical for the areal density of hard drive (Figure 2.4). It is estimated that for a 4Tbit/in^2 areal density the total distance the head-media spacing (HMS) needs to be reduced to approximately 4-5nm that requires ultrathin films of carbon overcoat and lubricant layers, and a sub-nanometer flying height of the slider [81]. At such a small spacing, wear and contacts between the head and the disk are extremely important for the reliability of the head-disk interface. More importantly, in heat-assisted magnetic recording, temperature of the head-disk interface reaches approximately 400-500°C and fast thermal cycling may cause deformation and degradation of both carbon overcoat and lubricant layer at the head-disk interface [28]. Clearly, a full understanding

of the flying characteristics, heat transfer, wear, and lubrication properties of the head-disk interface is required to improve the reliability of the head-disk interface.

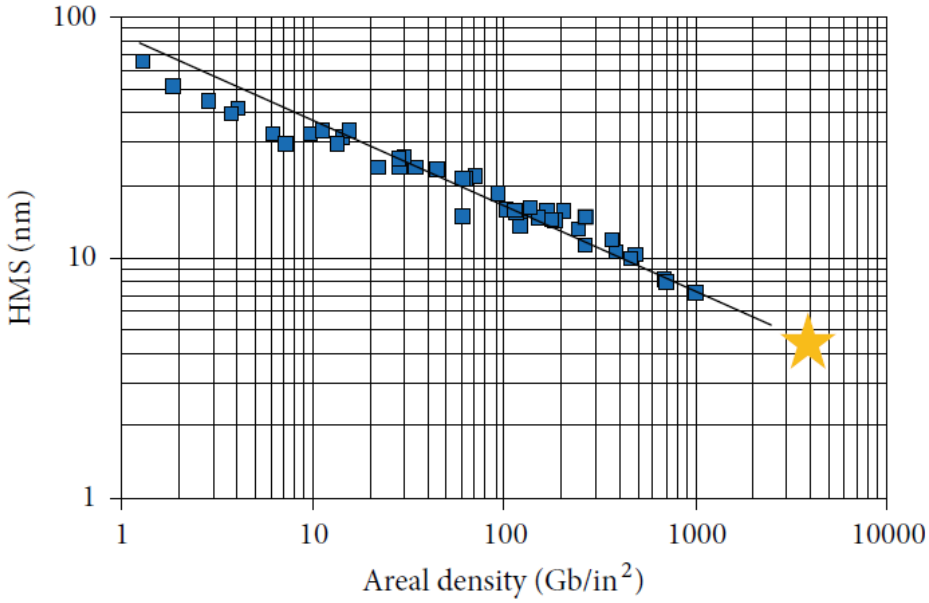

Figure 2.4 Areal density vs. head-media spacing [81]

2.2.1 Tribology of the Head-Disk Interface

Tribology is the science of friction, wear, and lubrication of surfaces in relative motion. It involves interdisciplinary subjects including physics, mathematics, chemistry, material science, and engineering [82]–[84]. Tribology has a long history back to ancient time when humans first made fire by grinding dry wood sticks against each other. Approximately 5,000 or 6,000 years ago, the first machines were invented (potter's wheels) that reduced friction or allowed transportation of heavy items for construction [82]. Over the course of history, many investigations have shown that humans have used friction and wear for the benefit of mankind. During the Neolithic Age (4,000-1,800 B.C.), Sumerians and Egyptians have used different types of "lubricants", including bitumen, animal and

vegetable oils, and water, to reduce friction. During the age of the Pharaohs, Egyptians used roller bearing to replace sliding friction with rolling friction to transport huge stone blocks that were used to build monuments. Sledges and lubricants were found in the pictures dating back to the period around 1880 B.C. (Figure 2.5).

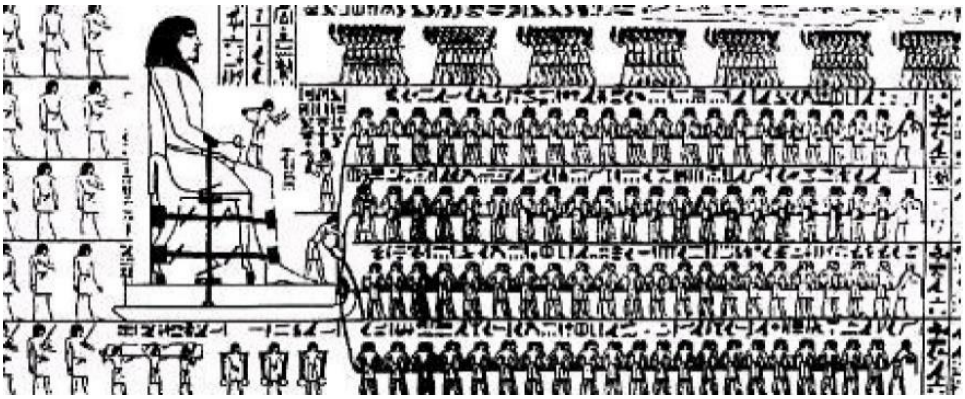

Figure 2.5 Old pictorial records show how humans used greased skids to transport an Egyptian statue to the grave of Tehuti-Hetep, El-Bersheh around 1880 B.C. [82]

However, the science of friction, wear, and lubrication was not quantitatively studied until the fifteen century, when Leonardo da Vinci examined the static coefficient of friction. Leonardo da Vinci spent more than 20 years on this topic and laid the foundation for modern tribology, including the first and the second friction laws for macroscopic scales. However, the development of tribology remained static until the seventeenth century when Guillaume Amontons conducted research in the “mixed” friction. He found that the friction force is a function of the normal force and he proposed the “interlocking” phenomenon between irregularities on the surfaces in sliding motion. Amontons derived laws of friction from an empirical study of tribology, that were similar to the laws that were discovered by Leonardo da Vinci two hundred years earlier [82], [84]. The laws of friction by Amontons are:

- The friction force is directly proportional to the applied load.
- The friction force is independent of the apparent area of contact.

In the seventeen century, John Theophilus Desaguliers found that two well-polished surfaces show higher frictional force, leading to the important discovery of adhesion and cohesion for friction [85]. However, Desaguliers could not fit his discovery to any existing model of friction. The effect of adhesion and cohesion on friction was later defined by Isaac Newton in his adhesion theory in which friction has molecular and mechanical causes that come from dynamic viscosity. Based on the viscous properties of a fluid, Isaac Newton introduced the concept of Newtonian and non-Newtonian fluids. During the eighteenth century, Charles-Augustin Coulomb investigated frictional resistance of a rolling wheel and a cylinder. He found that the frictional resistance is proportional to the applied load, and inversely proportional to the radius of the wheel. At the beginning of the nineteenth century, tribology studies became very popular to satisfy industrial demand. Different types of industrial lubricants were formulated and refined from petroleum, shale, and coal to replace vegetable and animal oils. In 1886, Osborn Reynolds published a fundamental equation about fluid film formation in a narrow gap between two moving solids. This equation is called Reynolds equation and is the basis of the classical lubrication theory [86]. The Reynolds equation will be presented in chapter 3 of this dissertation.

Richard Stribeck published the so-called Stribeck curve (Figure 2.6) in 1902 [87] that was considered a fundamental concept in the field of tribology. The Stribeck curve shows the relationship between the friction coefficient f in fluid-lubricated contacts,

contact load P, viscosity of the lubricant μ, and velocity of the lubricant N. Three regimes of lubrication are defined:

- Boundary lubrication: This type of lubrication occurs when micro asperities of the surfaces touch each other, leading to high friction. The load is supported mainly by surface asperities. The effect of the lubricating oil on the tribological characteristics is small.
- Hydrodynamic lubrication: In this type of lubrication, the fluid completely isolates the friction surfaces, i.e., the oil film thickness is larger than the surface roughness. Negligible contacts occur between asperities from the surfaces and the tribological properties are defined by the internal fluid friction only.
- Elasto-hydrodynamic lubrication and mixed lubrication: The oil film is in the same range with the surface roughness and the load is supported by both asperities and the fluid lubricant.

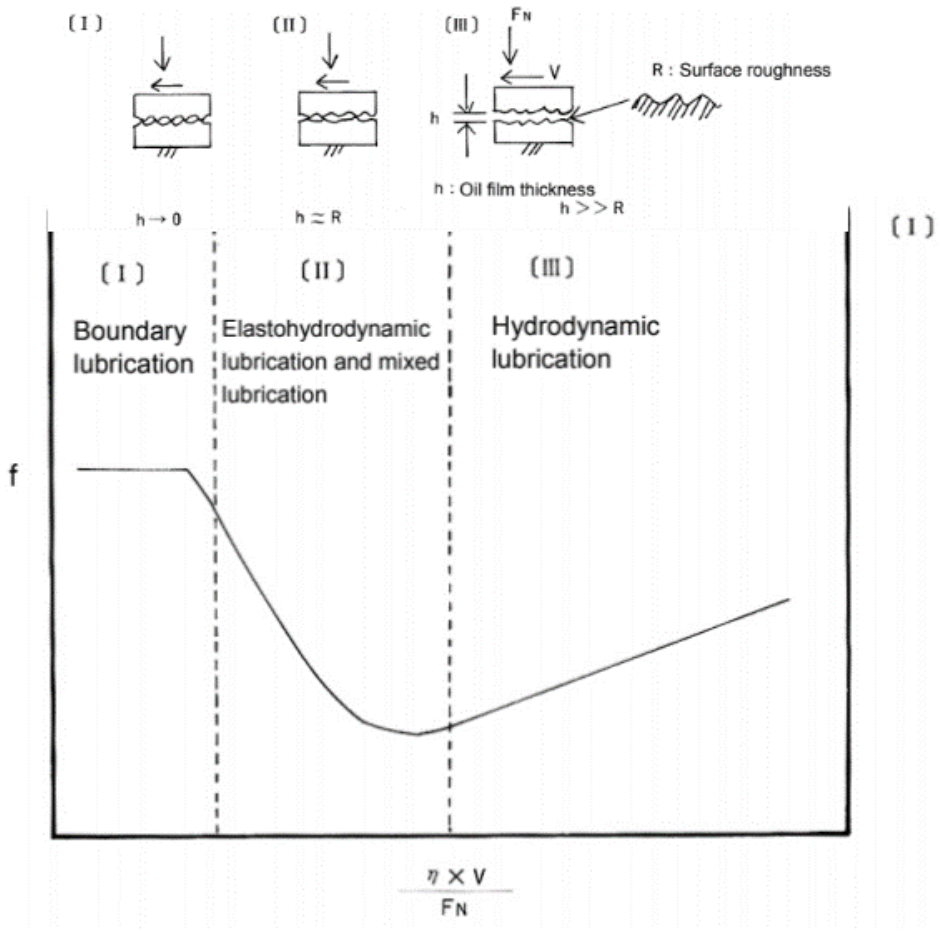

Figure 2.6 Stribeck curve and lubrication regions [87]

Bowden and Tabor studied the laws of friction in their book "The friction and lubrication of solids" [88]. They distinguished the "true area of contact" that is formed by the asperities of the surfaces that are in direct contact, versus the "apparent area of contact". They proposed that contact between two surfaces occur only at the tips of the highest asperities of the surfaces, making the true area of contact to be much smaller than the apparent area of contact. In the presence of normal loads, the tips of the asperities deform plastically, thereby increases the true contact area until the area is large enough to support the normal loads elastically. Bowden and Tabor's adhesion model or plastic junction model

shows the friction force F_f to be linearly proportional to the true contact area A_r, and the shear strength of the contacts σ, given as $F_f = A_r\sigma$. Similar to Bowden and Tabor, Archard found that surface asperities deform first plastically during contact before they reach a steady state condition to support the load elastically. Archard suggested that the number of contact spots increases with normal load [89]. To calculate the true contact area, Hertz [90] proposed a model for non-adhesive and elastic contacts between two spherical surfaces, the so-called Hertzian contact stress theory. However, the radius of the asperities is usually unknown, making a calculation of the true contact area very difficult. Different techniques have been developed and commercialized to quantitatively measure the surface roughness that can be categorized into (a) contact type measurements, and (b) non-contact type measurements. Typical examples are: Talysurf by Abbott and Firestone that has been commercialized in 1933; a non-contact optical profiler using two beam optical interferometry in 1983; and atomic force microscopy in 1985 [82], [91]. Since the invention of the atomic force microscopy, surface properties, wear and buildup of the head-disk interface have been studied extensively. An image of the atomic force microscopy DI-3100 is shown in Figure 2.7.

The understanding of friction, wear, and lubrication is very important for improving the reliability of the head-disk interface in hard drive. It is shown in Figure 2.4 that a reduction of the head-disk clearance is required to increase the areal density of hard drives. However, as the clearance decreases, contacts between the head and disk surface are likely to occur, resulting in surface degradation and possibly failure of the hard drives. For a storage density of 1Tbits/in^2, the distance between head and disk surfaces needs to be

approximately 1 nanometer [81]. Since the relative velocity between head and disk is in the range of 15-30m/s, it is apparent that the head-disk interface is one of the most challenging electro-mechanical systems ever built. Contacts between the head and the disk lead to wear and surface degradation of the head-disk interface. To maintain the integrity of the surfaces, both the disk and the slider are coated with a wear protective layer of diamond-like carbon. In addition, a thin lubricant film on the order of 1 nm in thickness is applied to the disk surface for wear and corrosion protection. The carbon overcoat and lubricant layers are molecularly thin, smooth, and bonded to the surfaces.

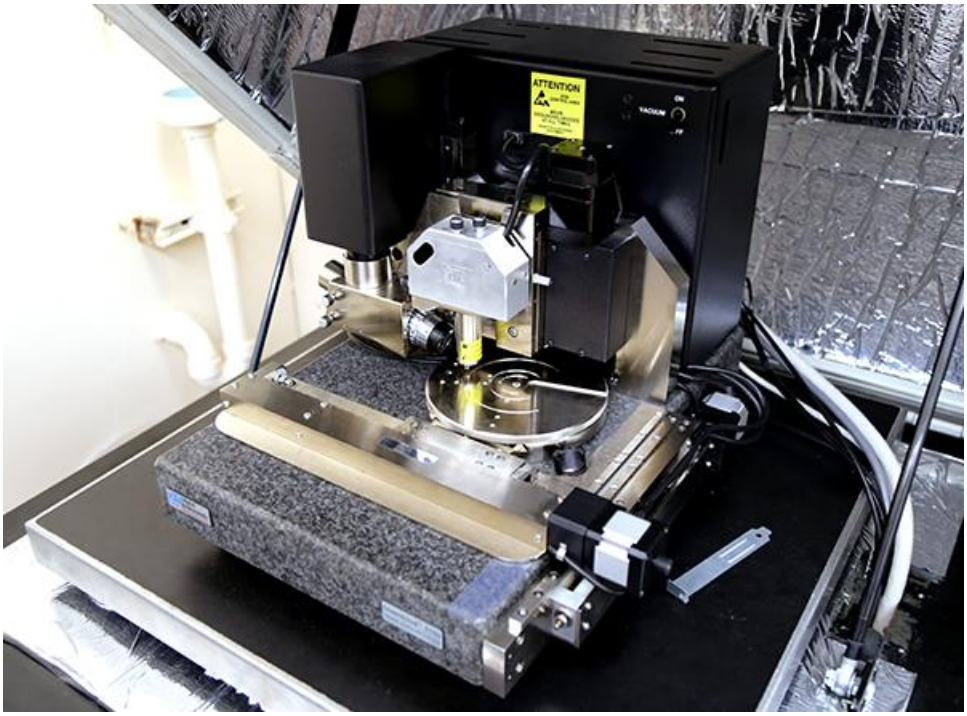

Figure 2.7 Atomic force microscope Digital Instrument 3100

2.2.2 Diamond-like Carbon (DLC) Overcoat

Carbon is one of the most fascinating elements on earth. Carbon is a nonmetal with 4 valence electrons in the s and p orbitals that are involved in chemical bonds. This allows carbon atoms to bond with different carbon atoms or with atoms of other chemical elements, such as hydrogen or nitrogen, etc. Depending on the bonding type, there exists many different allotropes of carbon [92], such as diamond, graphite, and amorphous carbon (Figure 2.8). In diamond, the s orbital mixes with three p orbitals to form four sp^3 hybridized orbitals that can bond to four other sp^3 orbitals of carbon atoms to form a tetrahedral crystalline structure. This bond is called σ bond. It is very strong, allowing diamond to be the hardest and the least compressible material on earth. In contrast, in graphite the s orbital mixes with three p orbitals to form three sp^2 hybridized orbitals in the plane and one p orbital perpendicular to that plane. The sp^2 hybridizations bond to the nearest three carbon atoms in the plane using strong σ bonds while the p orbital bonds to another carbon atom in another plane via weak π bonding. Therefore, graphite has a planar structure of layers that can easily move with respect to each other, providing excellent self-lubricating and thermal conduction properties compared to diamond.

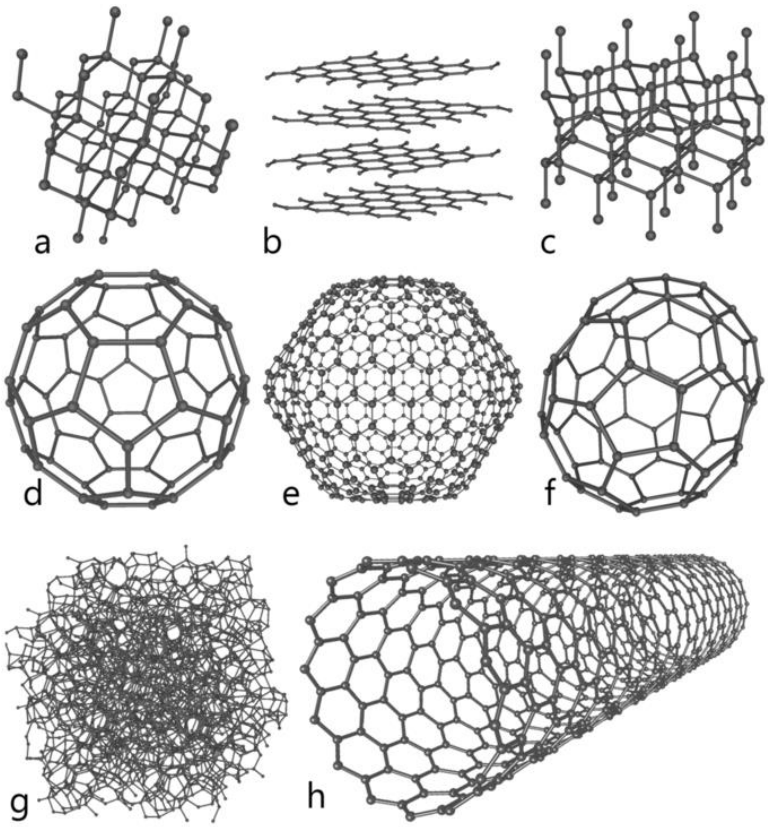

Figure 2.8 Allotropes of carbon (a) Diamond (b) Graphite (c) Lonsdaleite, d) C60 or buckyball, e) C540, f) C70, g) Amorphous carbon, and h) single-walled carbon nanotube, or buckytube. [92]

Amorphous carbon, abbreviated as a-C, is different from diamond and graphite in that it does not have any crystalline structure. Amorphous carbon contains a high fraction of diamond-like carbon sp^3 bonding besides microscopic crystals of graphite-like carbon sp^2 and possibly sp^1 bonds. The properties of amorphous carbon depend on the ratio of sp^2 and sp^3 bonds, the composition of hydrogen and nitrogen, sp^2 clustering and its phase orientation, and the cross sectional nanostructure [79]. Different types of amorphous carbon without nitrogen are shown in the ternary phase diagram (Figure 2.9) that was derived first by Jacob and Moller [79]. Diamond-like carbon, or DLC, is usually amorphous carbon (a-C) or hydrogenated amorphous carbon (a-C:H) with a large fraction

of metastable sp^3 bonds. Diamond-like carbon has similar properties as diamond, in terms of the Young's modulus, hardness, friction, and chemically inertness to both acid and base environments. In hard disk drives, one of the main purposes of the diamond-like carbon overcoat is to protect the surfaces from corrosion. Thus, the diamond-like overcoat film also needs to be smooth, continuous, and pin-hole free [79], [93]–[96]. Different types of diamond-like overcoat have been developed using different techniques. In the 1970s, Aisenberg, Chabot, and Holland used plasma deposition to first grow hard, amorphous carbon film layers [79]. In later studies, hydrogen was added to amorphous carbon, the so-called hydrogenated amorphous carbon or a-C:H, to improve the mechanical properties of thin films with respect to wear. Increasing hydrogen content of the overcoat results in a transformation from sp^2 to sp^3 bonding caused by the passivation of the carbon dangling bonds at the film surface. This leads to a prevention of oxidation and reduces chemical reactivity. On the other hand, it was found that increasing the hydrogen concentration beyond 20% leads to a softer carbon overcoat, and that increasing hydrogen content in the DLC overcoat allows lubricant to adhere better. Hydrogenated amorphous carbon (a-C:H) can be produced by plasma-enhanced chemical vapor deposition (PECVD), by reactive sputtering of graphite in hydrogen environment, or by ion beam deposition. These deposition techniques can produce a-C:H from 20% up to approximately 60% of hydrogen content. Advanced PECVD techniques, including electron cyclotron resonance (ECR), inductive coupled plasma (ICP), plasma beam source (PBS), or electron cyclotron wave resonance (ECWR), can produce dense hydrogenated amorphous carbon a-C:H, generally called tetrahedral hydrogenated amorphous carbon or ta-C:H. A drawback of using hydrogenated carbon overcoats is that contacts between slider and disk surface can result

in a local heating that leads to the outgassing of fluorine from the lubricant layer [79]. Fluorine can react aggressively with hydrogen from the overcoat layer to generate hydrofluoric acid (HF) that greatly affects the properties of the carbon overcoat layer. More recently, nitrogenated amorphous carbon overcoats, denoted as a-C:N, have replaced hydrogenated amorphous carbon a-C:H. Nitrogenated carbon overcoats have been shown to improve wear resistance and lubricant bonding behavior compared to hydrogenated carbon overcoats. Nitrogenated carbon overcoats do not react with fluorine from the lubricant during stress condition. Unfortunately, nitrogenated carbon overcoat layers below 4nm thickness are not continuous and do not work well to protect surfaces from corrosion. Increasing attention is currently paid to tetrahedral amorphous carbon ta-C with both hydrogen and nitrogen, including ta-C:H, ta-C:N, and ta-C:H:N . These materials are manufactured by mass selected ion beam deposition (MSIBD), pulsed laser deposition (PLC), and filtered cathodic vacuum arc (FCVA) deposition in nitrogen environment.

In heat-assisted magnetic recording technology, the disk surface is heated up locally to approximately 450°C within a nanosecond, posing a big challenge on the reliability of the diamond-like carbon overcoat layer. Many studies [28], [51], [81] have shown that at high temperature, sp^3 bonds tend to transform to sp^2 bonds, resulting in oxidation of the diamond-like carbon overcoat. An increase in sp^2 bonding in carbon overcoats results in a decrease in the mechanical properties of the overcoat. Clearly, for heat-assisted magnetic recording, an improved and more stable coating is required. Additional requirements include good optical and thermal conductivity of the overcoat layers on both the slider and disk surfaces.

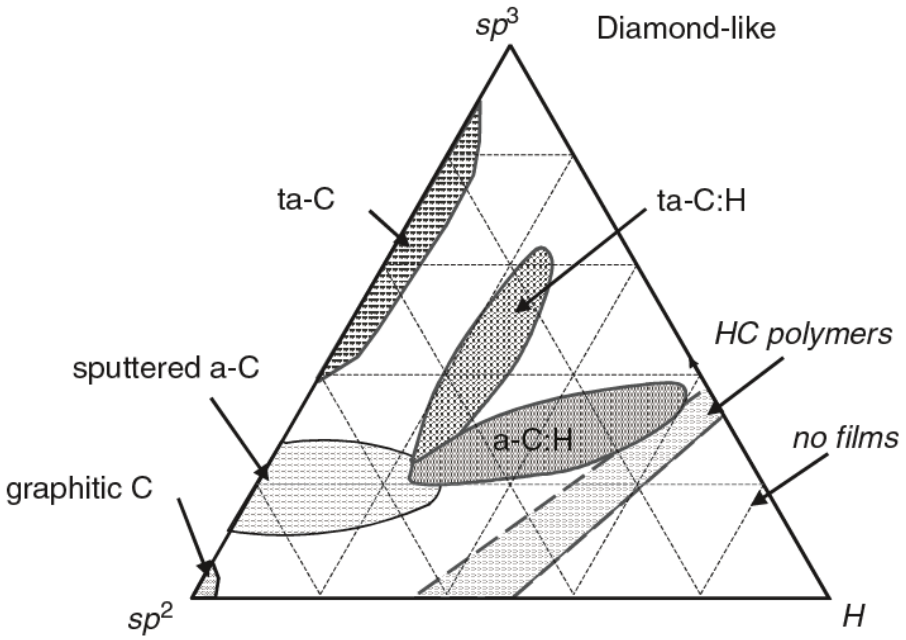

Figure 2.9 Ternary phase diagram of amorphous carbon with three corners corresponding to sp^2, sp^3, and hydrogen contents [79]

In summary, the ideal diamond-like carbon overcoat in hard disk drives should have the following physical and chemical properties: a) good corrosion protection (continuous and chemically inertness properties); b) good lubricant compatibility; c) mechanical and wear resistance; d) surface smoothness; and e) optical and thermal compatibility for the head-disk interface.

2.2.3 Disk Lubricant

As described in section 2.2.1, lubricants are used to protect the disk and slider surfaces from the severity of asperities contacts and to reduce frictional heating between surfaces. Clearly, lubricants play a critical role in the tribology of the head-disk interface as the slider flies at a close proximity over the disk surface. In hard disk drives, the lubricant layer is applied on the top of the DLC overcoat on the disk surface (Figure 2.10) using dip-

coating [84], [97], i.e., the disks are dipped and then pulled away from a lubricant-solvent bath. During the dipping and pulling processes, the solvents ($C_4F_9OCH_3$; $CF_3CHFCHFCF_2CF_3$; etc.) act as carrier of the lubricant to the disk surface before evaporating, leaving a thin lubricant layer of approximately 1-2nm on the disk surface. The thickness of the lubricant layer is controlled by the pull-rate and the concentration of the lubricant in the lubricant-solvent bath. The lubricant layer is designed to bond to the disk surface by annealing the lubricant polar end-group to the polar sites of the carbon overcoat layer on the disk surface at elevated temperature, reducing the lubricant evaporation and lubricant displacement during disk rotation [77], [80], [83], [96], [98]–[100]. The lubricant layer on the disk consists of bonded and the so-called "mobile" lubricant, the latter is an important part for a "self-repairing" property, i.e., the lubricant can reflow and replenish the area where lubricant was displaced due to head-disk contacts. Both bonded and mobile lubricants exist simultaneously on the disk surface and the ratio between bonded lubricant and non-bonded lubricant is called the bonded lubricant ratio (BLR). It typically ranged from 60% to 90% [100]. The bonded lubricant ratio is shown to be greatly affected by temperature and relative humidity conditions [80], [99], [101], [102].

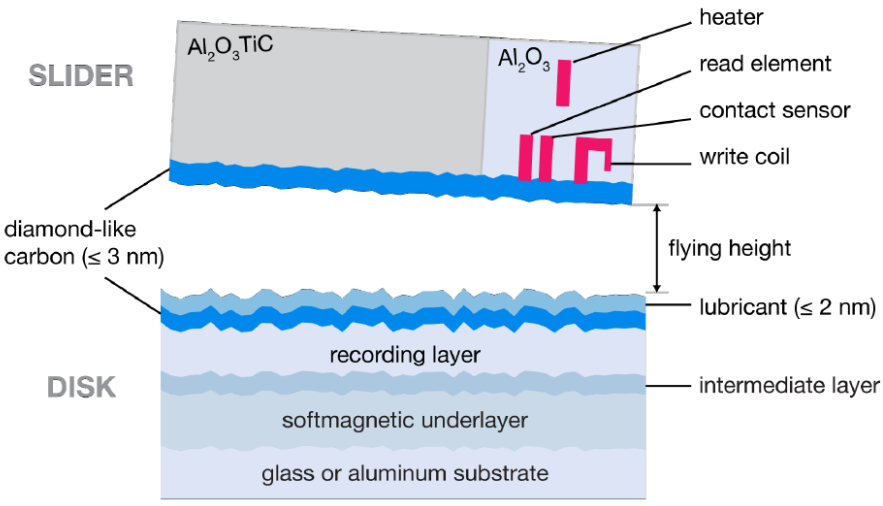

Figure 2.10 Head-disk interface, consisting of head and disk surface. A thin DLC carbon overcoat of approximately 3nm is coated on both the slider and disk surfaces. A thin lubricant layer of less than 2nm is coated on the top of the DLC layer on the disk surface. [103]

In hard disk drives, synthetic fluid lubricants of the perfluoropolyether (PFPE) family have been used extensively since the 1970s due to their extraordinary properties, including:

1. Excellent boundary lubrication properties, providing good wear protection.
2. Good surface adhesion towards the carbon overcoat layer.
3. Very low vapor pressure that prevents lubricant loss by evaporation.
4. High mobility allowing lubricant reflow and replenishment.
5. Low surface energy that decreases stiction between head and disk surfaces.
6. Good thermal and chemical stability.

PFPE lubricants contain carbon, oxygen, and fluorine atoms in their chain. A typical PFPE lubricant is Fomblin-Z and Demnum with the structure shown in Figure 2.11 [104].

$$\mathbf{X - CF_2 - O - (CF_2 - O -)_x - (CF_2CF_2 - O)_y - CF_2 - X}$$

(a) Fomblin Z

$$\mathbf{CF_3CF_2CF_2 - O -(CF_2CF_2CF_2 - O)_y - CF_2CF_2 - X}$$

(b) Demnum

Figure 2.11 Chemical structure of Fomblin-Z and Demnum lubricants [104]

Both Fomblin-Z and Demnum lubricants have the so-called perfluoropolyether (PFPE) backbone with different polar end-groups X (Figure 2.11). Fomblin-Z lubricants are random copolymers that are produced by photo-oxidizing tetrafluoroethylene and hexafluoropropylene [101], [104], while Demnum lubricants are synthesized using polymerization of perfluorpropylene oxide and trimethylene oxide [76], [105]. In the chemical formula, X represents a functional end group, such as $-CF_3$, $-CH_2OH$ (hydroxyl), and -COOH (carboxyl) groups. In Fomblin-Z lubricant, there are two functional end groups at both ends while in Demnum there is only one functional end group. Bonding between the PFPE backbones is weak dispersive bonding while the end groups to the carbon overcoat layer is strong polar bonding, respectively. It has been shown by Tyndall [106] that the polar functional group determines the bonding property between the lubricant and the carbon overcoat layer on the disk surface.

In addition to the bonding property, the molecular weight, the uniformity, and the thickness of the lubricant layer are important for the chemical and mechanical properties

of the PFPE lubricants. High molecular weight lubricants are shown to have an increased stiction [84], [107] and a decreased vapor pressure compared to lubricants with lower molecular weight. Lubricant transfer from the disk to the slider surface is also a strong function of the molecular weight and the thickness of the lubricant layer [98], [107]–[110]. Clearly, designing the lubricant layer to be thin and durable is a critical task for improving the reliability of the head-disk interface.

In heat-assisted magnetic recording, high temperature and fast heating and cooling cycles are present that cause a number of issues for the lubricant [28]. Thermal shear stress and lubricant evaporation are two dominant effects in heat-assisted magnetic recording, leading to decomposition and removal of the lubricant from the disk surface [28], [111]. Decomposition of the lubricant layer may lead to the formation of smear [111], [112] at the head-disk interface that can affect the flying height of the slider and the areal density of hard disk drives.

2.2.4 Effect of Helium on Head-Disk Interface Tribology

Helium has been proposed to be a replacement of air inside the hard disk drives for a long period of time [42], [64], [113]. Since 1960s, the first helium-filled rotating drum was manufactured by Control Data Corporation in Minnesota, United States [113]. An external helium tank was used to maintain and replenish the helium environment inside the drum. This approach was inefficient and very expensive. In the 1980s, IBM, Nippon Telephone and Telegraph (NTT), and Magnetic Peripherals Inc. developed hard disk drives that were located inside a large helium-filled tank of 55 gallon. The disk drive was 12 inches tall and featured disks of 14 inches diameter. Sealing a helium-filled disk drive was

a difficult task in the 1980s, leading to the loss of helium at a fast rate. The research and development of helium-filled hard disk drives slowed down until the late 1990s when the areal density of hard drives increased significantly by decreasing the writing ratio, including both bits per inch (BPI) and tracks per inch (TPI). At the same time, enterprise data storage required an increase in reading and writing performance of hard disk drives, resulting in a production of high speed hard disk drives of 10,000 and 15,000 rpms. An increase of the rotational speed of the disks, however, caused a significant increase of windage and induced vibrations of the disks. Helium-filled hard disk drives were an option that it could potentially solve the problem, allowing higher tracks per inch, and bits per inch. A reduction of disk vibrations in helium is related to the fact that helium is much lighter than air and that the turbulence is low in helium compared to turbulence flow in air environment. In addition, the power consumption that is required to rotate the spindle and disks are significantly less in helium compared to air. Power saving is important for small devices, such as mp3 players, mobile phones, laptops, or for high performance data centers. More importantly, helium has higher thermal conductivity than air, allowing better heat dissipation of helium-filled hard drives compared to air-filled hard drives. As a result,

temperature of helium-filled hard drives is lower than air-filled hard drives contributing to a reduced cost of air conditioning inside data centers.

Figure 2.12 Helium-sealed Hard Disk Drives

In 2006, a compressible tin-coated C-seal was developed that was located between the base and the cover of a hard disk drive to seal helium [113]. Testing showed that tin-coated seals would allow helium to remain sealed for up to 5 years of operations of a hard drive. The drawback of C-seal is that the C-seal was only manufactured in a rough shape that did not fit the shape of the hard drives. Modifying the shape of the C-seal was a difficult task. More seriously, C-seal was shown to be not compatible with shock, leading to helium loss in the presence of mechanical shock over the lifetime of the drives. Another sealing technique was developed that used hot-melt pressure-sensitive adhesives to reach up to 5 years life span of sealing. At the same time, laser welded cover was patented and became

a popular technique for sealing helium inside a hard drive. To further increase the capacity of disk drives, more disks are packed inside the same hard drive enclosure. Helium was again shown to be the only viable technology that allows an increase of the number of disks inside the hard drive enclosure (40% increase compared to conventional air-filled hard drives). In 2012, the first helium-sealed hard disk drives were commercialized (Figure 2.12). Interconnections are hermetically sealed using epoxy-bonding. Sensors are incorporated inside the drive to monitor relative humidity, temperature, and helium pressure.

2.3 Head-Disk Spacing Measurements

Since 1956, the head-disk spacing has decreased from 20 micrometers to approximately 1 nanometer. A number of different measurements methods have been developed and utilized to measure the head-disk spacing. The measurement techniques can be classified into two categories: optical and electrical measurements.

2.3.1 Optical interferometry techniques

Optical interferometry has been used as early as 1919 for the measurement of the thickness of a lubricating film on a glass surface. Since then, optical interferometry has been used exclusively for the measurements of the thickness of thin films, including head-disk spacing measurements using intensity-based [114]–[118] and polarization interferometry [114], [119], [120]. Both white light and monochromatic light of different wavelength can be used as light source for the measurement of head-disk spacing resolution down to 10 nanometers in thickness. The measurement frequency was limited up to 100 kHz [121]. A drawback of using optical interferometry techniques for spacing

measurements is that a transparent glass disk is required instead of a magnetic disk (Figure 2.13).

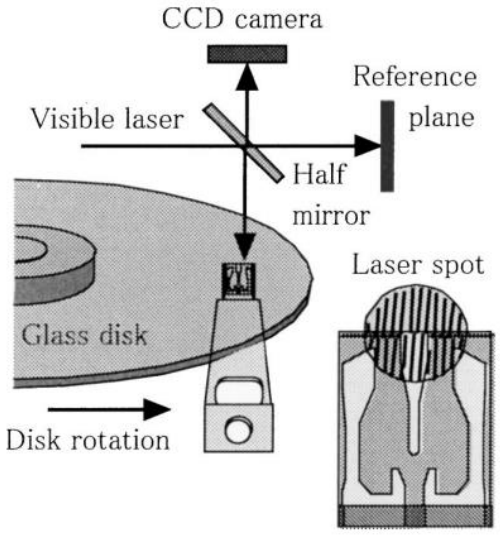

Figure 2.13 Measurement of head-disk spacing using interferometry [122]

An interferometry setup is complicated and expensive, making it unlikely for drive level measurements. For component-level testing, one of the most well-known techniques that have been used to measure dynamic spacing between the head and the disk surfaces since 1990s is using Laser Doppler vibrometry (LDV) with dual-beam interferometry. LDV is used to focus a laser beam to the slider that flies on the disk. Measurements of the frequency shift of the reflected laser beam are used to investigate the velocity and direction of the vibrating slider on the disk surface. Operating principle of the LDV is shown in Figure 2.14. Using laser Doppler vibrometry allows a measurement of dynamical motion of the slider and disk, regardless of slider and disk materials. Laser Doppler vibrometry allows measurements of the head-disk spacing down to sub-nanometer resolution and a measuring frequency up to 40MHz and is used to validate different measurement techniques [121], [123].

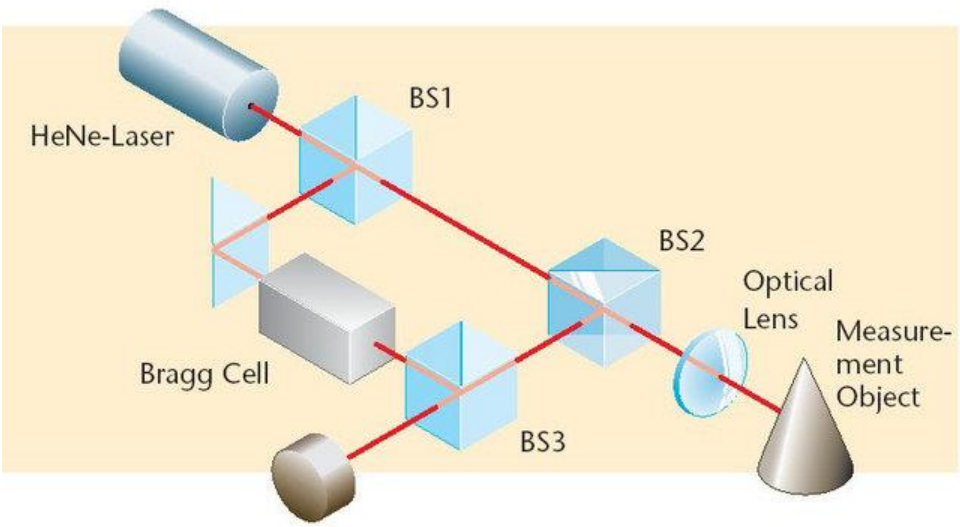

Figure 2.14 Operating principle of Laser Doppler vibrometry (LDV) [103]

2.3.2 Electrical techniques

Popular measurements of the head-disk spacing using electrical techniques include capacitance probe, Wallace spacing measurements, and thermal-flying height control (TFC) sliders. Capacitance probe measurements can be performed by mounting a capacitance probe on one of the surfaces [124]–[126] and monitor the change of capacitance due to flying height changes of the slider. The drawback of the capacitance probe measurements method is that the surface needs to be conductive and that the technique is difficult and expensive to implement in a hard drive. In capacitance probe measurement, the capacitance between two parallel flat surfaces is a function of the area of the probe and the minimum flying height of the slider. In the presence of a pitch angle α and a roll angle β of the slider, the capacitance of the plate can be calculated as [127]

$$C = \varepsilon_0 \int_0^B \int_0^L \frac{dxdy}{h'_m + xtan(\alpha) - ytan(\beta)}$$

where ε_0 is the dielectric constant of the ambient air, *L* and *B* are the length and width of the slider, respectively, and h'_m is the effective film thickness. The effective film thickness h'_m is a function of the minimum flying height h_m of the slider and the dielectric constants of the lubricant and the coating layers ε_l and ε_c, and t_l and t_c are the thickness of the lubricant and the carbon overcoats.

$$h'_m = h_m + \frac{t_l}{\varepsilon_l} + \frac{t_c}{\varepsilon_c}$$

Another "electrical" technique for measuring the head-disk spacing is the so-called Wallace spacing measurements. In this technique, data was first written on the disk surface before reading back using the read and write element. The so-called "readback" signal is used to determine the head-disk spacing. The measurement is named by Wallace after he derived the so-called "Wallace spacing loss" equation [128], [129] that shows the readback signal of the sinusoidal recorded signal $E(t)$ is an exponential function of the spacing between head and disk in 1951. The Wallace spacing loss equation is presented in equation (2.):

$$E(t) = f(M, \delta)e^{-\frac{2\pi d}{\lambda}}$$

, in which E denotes the amplitude of the readback signal, λ is the wavelength of the recorded signal, and d is the head-disk spacing. $f(M, \delta)$ is a function of the peak remanent magnetization M of the recording medium, and its thickness δ. From the equation (), the head-disk spacing change can be measured from the amplitude of the readback signal. Another approach is to use the full width at half maximum (FWHM) of the readback signal

PW_{50} that has been shown to be a linear function of the head-disk spacing. Wallace spacing measurements have been used in hard disk drives industry for the last 60 years and is one of the most popular technique for measuring absolute head-disk spacing in heat-assisted magnetic recording (HAMR).

Recently, thermal-flying height control (TFC) sliders were introduced. In thermal-flying height control (TFC) slider, micro resistive heater elements are embedded inside the sliders which are located near the read and write elements, the so-called reader heater and writer heater, respectively. Applying a power to the heater elements results in a thermal protrusion located near the read and write transducers, therefore bringing the read and write elements closer to the disk surface [130]–[132]. As the heater power increases, the size of the thermal protrusion increases that eventually leads to contacts between the thermal protrusion and the disk surface as shown in Figure 2.15. Contact between the protrusion and the disk surface are detected using acoustic emission, touchdown sensor, laser Doppler vibrometry, or strain gauge methods. The heater power at which an onset of contact between the thermal protrusion and the disk surface is referred to the touchdown power (TDP) or power-to-contact (PTC). Using thermal-flying height control sliders allows a precise measurement of the slider flying height down to Angstrom scale and recently has been popularly used to characterize wear of the slider surfaces. The first thermal flying height control (TFC) sliders were implemented to a hard disk drives in 2007 by Hitachi and have become a standard component in hard disk drives.

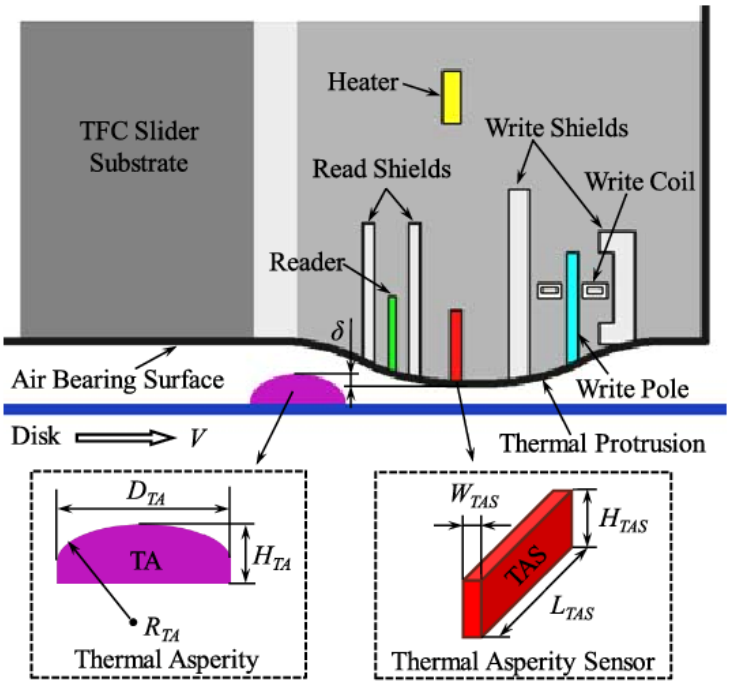

Figure 2.15 A schematic of Thermal-Flying Height Control (TFC) Slider [130]

2.4 Summary

In this chapter, the main components of a hard disk drive and the development of helium-filled hard disk drives were presented. Thereafter, the tribology of the head-disk interface was discussed and an overview of diamond-like carbon (DLC) and lubricant chemistry at the head-disk interface was given. In addition, different measurement techniques were presented for measuring the spacing between head and disk surfaces.

Chapter 3

The Effect of Van-der-Waals and Electrostatic Forces on the Flying Characteristics of Sliders

3.1 Reynolds Equation and Rarefaction Effects for Ultra-Low Head-Disk Clearance

The Reynolds equation is a partial differential equation (PDE) that is used to study the pressure distribution of thin viscous fluid films in lubrication theory. The classical Reynolds equation was derived first by Osborne Reynolds in 1886 [133] from the continuity equation and the Navier-Stokes equations of fluid mechanics using the following assumptions:

- The fluid film thickness is much smaller than the width w and length L of the interface ($h << L$ and $h << w$)
- Newtonian fluid with constant viscosity and no-slip boundary condition
- Laminar and isothermal flow
- The viscous force is dominant compared to inertia and surface tension force

A typical control volume of a pivoted slider bearing, featuring a thin air film [116], [134] between the head and the disk surfaces, is shown in Figure 3.1. In the figure, the head-disk spacing is denoted by *h(x,y)* as a function of x and y coordinates and h_{min} denotes the minimum head-disk spacing. *B* and *L* are length and width of the slider, respectively. The disk velocities in the x and y directions are *U* and *V* with respect to the slider surface. A hydrodynamic air bearing is formed at the head disk interface due to the relative motion between slider and disk. Viscous forces in the air bearing support the normal load of the slider, allowing the slider to "fly" at a constant distance *h* from the disk surface. In the thin air bearing, the velocity of the air flow is denoted as **u** = (u; v; w) corresponding to the velocity components in the x, y, and z directions. In current hard disk drive, the length and the width of the sliders are B = 0.85mm and L = 0.7mm, respectively. It is important to note that the head-disk spacing is on the order of a few nanometers, i.e., the head-disk spacing is five orders of magnitude smaller than the slider length and width, respectively.

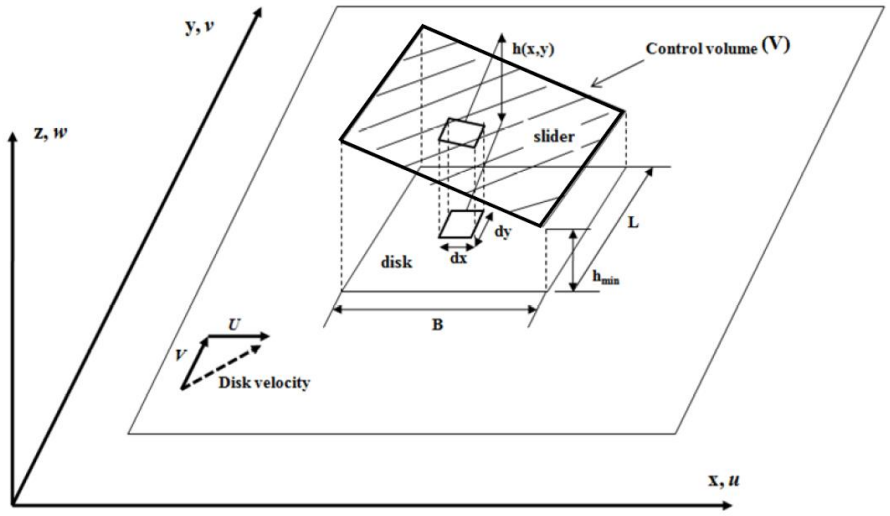

Figure 3.1 A schematic of a pivoted slider bearing control volume [135]

As shown in Figure 3.1, we define the control volume V enclosed by the surface A. The mass enclosed inside the volume V is described as $M(t) = \iiint_V \rho dV$ where ρ is the density of the fluid. The mass of the fluid that flows across the boundary surface A is given as $Flux(t) = \iint_A \rho \vec{u}.\vec{n} dA$ where $\vec{n}$ is the normal to the boundary surface area A (Figure 3.2). The conservation of mass states that the rate of change of the mass inside the control volume V must be equal to the mass that flows across the boundary surface A. Thus,

$$\iint_A \rho \vec{u}.\vec{n} dA = -\frac{\partial}{\partial t} \iiint_V \rho dV$$

$$, \text{ or } \iint_A \rho \vec{u}.\vec{n} dA + \frac{\partial}{\partial t} \iiint_V \rho dV = 0 \qquad (3.1)$$

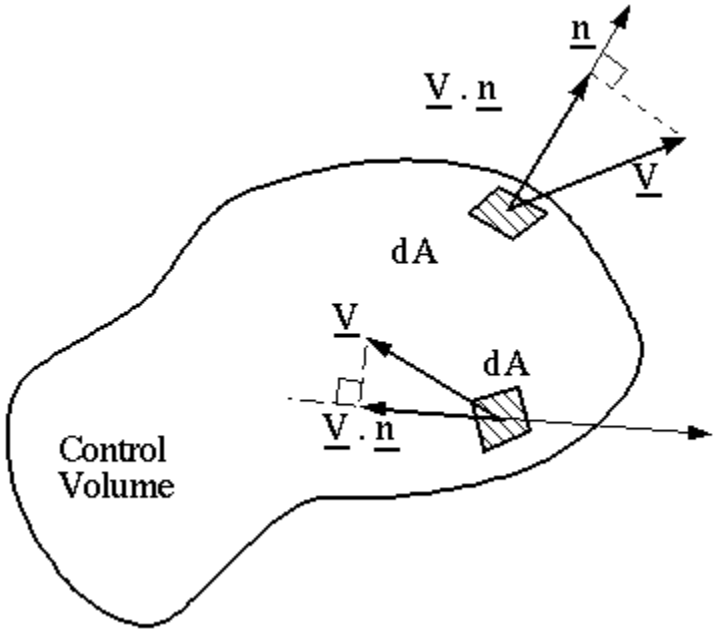

Figure 3.2 Conservation of mass and momentum in the control volume [135]

Thus, the Gauss's theorem (divergence theorem), can be used to relate flux through the surface A to the vector field in the control volume V, i.e.,

$$\iint_A \rho \vec{u}.\vec{n} dA = \iiint_V \nabla.\rho \vec{u} dV \tag{3.2}$$

Applying Gauss's theorem to equation (3.1) we obtain the continuity equation as (3.3):

$$\iiint_V \nabla.\rho \vec{u} dV + \frac{\partial}{\partial t} \iiint_V \rho dV = 0$$

This is equivalent to

$$\iiint_V \left(\nabla.\rho \vec{u} + \frac{\partial \rho}{\partial t} \right) dV = 0 . \tag{3.3}$$

Since the control volume V is chosen arbitrarily, one can write equation (3.3) in differential form as:

$$\nabla.\rho \vec{u} + \frac{\partial \rho}{\partial t} = 0 \tag{3.4}$$

Equation 3.4 is the continuity equation. In addition to the conservation of mass, the conservation of momentum states that the rate of change of linear momentum of a system is equal to the net force that acts on the system [134]. The rate of change of linear momentum includes the instantaneous time derivative of the momentum and the net rate of transport of the momentum across the boundaries:

$$\frac{d}{dt} \iiint_V \rho \vec{u} dV = \frac{\partial}{\partial t} \iiint_V \rho \vec{u} dV + \iint_A \vec{n}.\rho \vec{u} \vec{u} dA \tag{3.5}$$

The net force $\vec{F}$ consists of the surface force τ that acts on the surface A of the control volume and the body force f that applies to the control volume V

$$\vec{F} = \iint_A \vec{n}.\tau dA + \iiint_V \rho f dV \tag{3.6}$$

One can neglect the gravitational force and the body force as being negligibly small compared to the viscous forces in an air bearing. Therefore, the conservation of momentum equation can be written as follows:

$$\iiint_V \frac{\partial}{\partial t}(\rho\vec{u})dV + \iint_A \vec{n}.\rho\vec{u}\vec{u}dA = \iint_A \vec{n}.\tau dA \tag{3.7}$$

In this case, using the divergence theorem in the equation (3.6) and given that the integrand is independent of the control volume V the momentum equation in differential form is given by:

$$\rho\left[\frac{\partial\vec{u}}{\partial t} + \vec{u}.\nabla\vec{u}\right] = \nabla.\tau \tag{3.8}$$

For a Newtonian fluid, the constitutive equation that describes the relation between the deformation and the stress [136] is as follows:

$$\tau = -\left(p + \frac{2}{3}\mu\nabla.\vec{u}\right)\delta + \mu\left(\nabla\vec{u} + \left(\nabla\vec{u}\right)^T\right), \tag{3.9}$$

where p is the pressure, μ is the viscosity of the fluid, and δ is a second-order isotropic tensor.

A scale analysis, or order-of-magnitude analysis, is used to simplify the mass and momentum conservation equations. First, the dimensions and velocities are nondimensionalized as follows:

$$x = \frac{x}{B}; y = \frac{y}{L}; \tilde{z} = \frac{z}{h_{\min}} \tag{3.10}$$

$$u = \frac{u}{U}; \tilde{v} = \frac{v}{V}; w = \frac{w}{W} \tag{3.11}$$

Similarly, the normalized pressure and density are nondimensionalized using ρ_a and P that are the ambient density and pressure of the fluid, respectively.

$$\rho = \frac{\rho}{\rho_a}; p = \frac{p}{P} \tag{3.12}$$

Replacing equations (3.9) (3.10) and (3.11) into the steady-state continuity equation (3.3), i.e., the dependency of time is omitted, we obtain

$$\frac{\rho_a U}{B}\frac{\partial(p^* u^*)}{\partial x^*} + \frac{\rho_a V}{L}\frac{\partial(p^* v^*)}{\partial y^*} + \frac{\rho_a W}{h_{\min}}\frac{\partial(p^* w^*)}{\partial z^*} = 0 \tag{3.13}$$

Given that all the terms in equation (3.13) must have the same scales or units, the velocity component in the z direction W is given by:

$$W \sim \frac{h_{\min}}{B} \text{ and } U \sim \frac{h_{\min}}{L} V \tag{3.14}$$

Similarly, if the scale analysis and the constitutive equation (3.8) is applied to the momentum conservation equation (3.7), the following equation is obtained:

$$\frac{P{h_{\min}}^2}{\mu UB}\frac{\partial p^*}{\partial x^*} = \frac{\partial^2 u^*}{\partial z^{*2}}; \frac{P{h_{\min}}^2}{\mu VL}\frac{\partial p^*}{\partial y^*} = \frac{\partial^2 v^*}{\partial z^{*2}}; \frac{\partial p^*}{\partial z^*} = 0 \tag{3.15}$$

In dimensional form, we obtain the following equations:

$$\frac{\partial p}{\partial x} = \frac{\partial}{\partial z}\left(\mu\frac{\partial u}{\partial z}\right); \frac{\partial p}{\partial y} = \frac{\partial}{\partial z}\left(\mu\frac{\partial v}{\partial z}\right); \frac{\partial p}{\partial z} = 0 \tag{3.16}$$

Using no-slip boundary conditions, where the velocities of the fluid flow at the disk surface are the same as the velocities of the boundary surfaces, gives

$$\begin{cases} z = 0 : u = U; v = V \\ z = h : u = 0; v = 0 \end{cases} \tag{3.17}$$

Integrating equations (3.15) and applying the boundary conditions (3.16), the velocities of the fluid in the x and y direction are given by:

$$\begin{cases} u = \dfrac{1}{2\mu}\dfrac{\partial p}{\partial x}\left(z^2 - zh\right) + U\left(1 - \dfrac{z}{h}\right) \\ v = \dfrac{1}{2\mu}\dfrac{\partial p}{\partial y}\left(z^2 - zh\right) + V\left(1 - \dfrac{z}{h}\right) \end{cases} \tag{3.18}$$

Using the ideal gas law and velocity equations above to the continuity equation (3.3), we obtain the so-called 2D Reynolds equation for compressible gases as follows:

$$\frac{\partial}{\partial x}\left(ph^3\frac{\partial p}{\partial x}\right) + \frac{\partial}{\partial y}\left(ph^3\frac{\partial p}{\partial y}\right) = 6\mu\left(U\frac{\partial ph}{\partial x} + V\frac{\partial ph}{\partial y}\right) + 12\mu\frac{\partial ph}{\partial t} \tag{3.19}$$

In differential form, expression (3.18) can be rewritten as

$$\nabla.\left(ph^3\nabla p\right) = 6\mu u.\nabla\left(ph\right) + 12\mu\frac{\partial\left(ph\right)}{\partial t} \tag{3.20}$$

For current hard disk drives, the head-disk spacing is reduced to less than 10nm. This spacing is much smaller than the mean free path of air (~65nm) and helium (~175nm) at normal temperature and pressure conditions. In this case, the no-slip boundary condition is not applicable and "rarefaction" effects must be considered to simulate the pressure distribution of the air bearing [134], [137]. Rarefaction effects are a function of the Knudsen number, which is a function of the ratio between the mean free path and the spacing between slider and disk, i.e., Knudsen number $Kn = \dfrac{\lambda}{h}$. As the head-disk spacing decreases, the Knudsen number increases. It can be shown that if the Knudsen number Kn exceeds 0.01, the continuum theory of fluid with no-slip boundary condition is no longer applicable, and the so-called "slip" boundary conditions need to be considered. Different

slip correction models have been developed and used to correct the Reynolds equation, including the first-order slip flow correction, the second-order slip flow, and the Bolzmann correction [137]. The first-order slip boundary correction is applicable for Knudsen number in a range $0.01 < Kn < 0.1$ or equivalently, if the head-disk spacing is larger than 600nm and less than 6 micrometers. In the first-order slip boundary condition, the boundary conditions are corrected using the mean free path λ of the fluid:

$$\begin{cases} u(z=0) = U + \lambda \left.\dfrac{\partial u}{\partial z}\right|_{z=0} ; v(z=0) = \lambda \left.\dfrac{\partial v}{\partial z}\right|_{z=0} \\ u(z=h) = -\lambda \left.\dfrac{\partial u}{\partial z}\right|_{z=h} ; v(z=h) = \lambda \left.\dfrac{\partial v}{\partial z}\right|_{z=h} \end{cases} \tag{3.21}$$

As the head-disk spacing is reduced to less than 100nm, the so-called second-order slip model is more accurate compared to the first-order slip model.

$$\begin{cases} u(z=0) = U + \lambda \left.\dfrac{\partial u}{\partial z}\right|_{z=0} - \dfrac{\lambda}{2} \left.\dfrac{\partial^2 u}{\partial z^2}\right|_{z=0} ; v(z=0) = \lambda \left.\dfrac{\partial v}{\partial z}\right|_{z=0} - \dfrac{\lambda}{2} \left.\dfrac{\partial^2 v}{\partial z^2}\right|_{z=0} \\ u(z=h) = -\lambda \left.\dfrac{\partial u}{\partial z}\right|_{z=h} - \dfrac{\lambda}{2} \left.\dfrac{\partial^2 u}{\partial z^2}\right|_{z=h} ; v(z=h) = \lambda \left.\dfrac{\partial v}{\partial z}\right|_{z=h} - \dfrac{\lambda}{2} \left.\dfrac{\partial^2 v}{\partial z^2}\right|_{z=h} \end{cases} \tag{3.22}$$

If the head-disk spacing is on the order of a few nanometers, the so-called Boltzmann correction must be used to derive the Reynolds equation. Applying the velocity boundary conditions to equations (3.16), Fukui and Kaneko [75] generalized the Reynolds equation with rarefaction effects in the following form:

$$\nabla.\left(\overline{Q} ph^3 \nabla p\right) = 6\mu u.\nabla(ph) + 12\mu \frac{\partial}{\partial t}(ph) \tag{3.23}$$

, where $\overline{Q}$ is the correction term, describing the ratio of the Poiseuille flow rate $Q_p(D)$ and the continuum flow rate $Q_c(D)$, and D is the modified inverse Knudsen number $D = \dfrac{\sqrt{\pi}}{2Kn}$.

The correction terms for the first-order, second-order, and Boltzmann slip boundary conditions are expressed by equations (3.24-3.26):

$$\overline{Q} = \frac{D}{6} + \frac{\sqrt{\pi}}{2} \tag{3.24}$$

$$\overline{Q} = \frac{D}{6} + \frac{\sqrt{\pi}}{2} + \frac{\pi}{4D} \tag{3.25}$$

$$\overline{Q} = \begin{cases} \dfrac{D}{6} + 1.0162 + \dfrac{1.0653}{D} - \dfrac{2.1354}{D^2} & (5 \le D) \\ 0.13852D + 1.25087 + \dfrac{0.15653}{D} - \dfrac{0.00969}{D^2} & (0.15 \le D \le 5) \\ -2.22919D + 2.10673 + \dfrac{0.01653}{D} - \dfrac{0.0000694}{D^2} & (0.01 \le D \le 0.15) \end{cases} \tag{3.26}$$

3.2 Slider Equilibrium Equations in the presence of the Van-der-Waals and Electrostatic Forces

An air bearing slider has three main degrees of freedom. They are the vertical displacement in the z-direction (h), the pitch angle (α), and roll angle (β) around the pivot point at the dimple-gimbal interface.

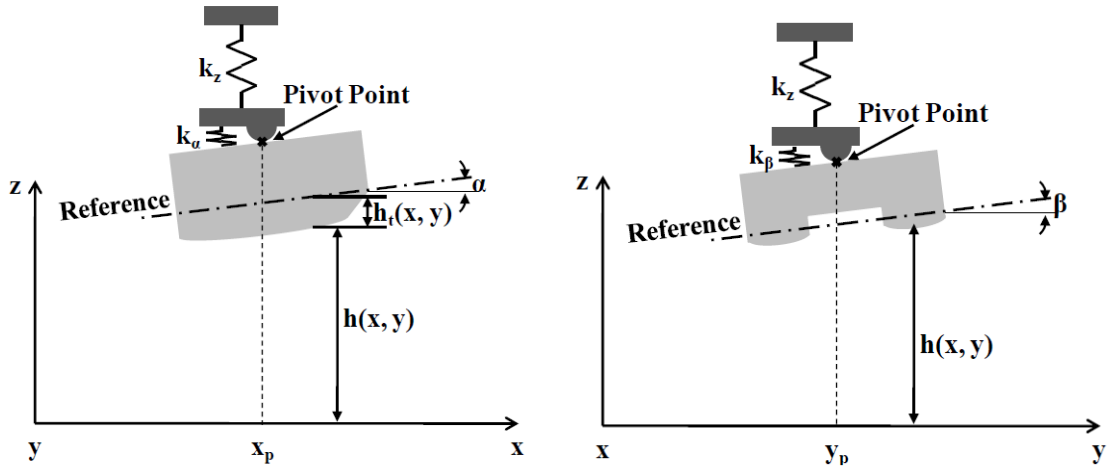

Figure 3.3 (a) A schematic of the slider from (a) the side and (b) the trailing edge [135]

A schematic of the head-disk interface is shown in Figure 3.3, where the vertical displacement of the slider is modelled by the spring k_z, while the pitch and roll displacements of the sliders are modelled by the springs k_α and k_β, respectively. At the head-disk interface, the spring k_z corresponds to the vertical stiffness of the suspension of the slider and springs k_α, k_β are related to the flexural stiffness of the suspension. During operation of the hard drive, the total forces that are applied to the slider from the suspension is in equilibrium with the air bearing forces and moments, i.e.

$$\begin{cases} \sum F_z = F_{airbearing} - F^{pre-load} = k_z dh \\ \sum M_\alpha = M_{airbearing\_y} - M_\alpha^{pre-load} = k_\alpha d\alpha \\ \sum M_\beta = M_{airbearing\_x} - M_\beta^{pre-load} = k_\beta d\beta \end{cases} \tag{3.27}$$

where $F^{pre-load}$ denotes the load of the suspension on the slider body in the z-direction, and $M_\alpha^{pre-load}$ and $M_\beta^{pre-load}$ are the pre- load moments about the x- and y- directions (pitch and roll). The force that an air bearing acts on the slider surface is calculated by integrating the pressure distribution over the slider surface area, i.e.

$$F_{airbearing} = \iint_A p(x,y)dA \tag{3.28}$$

Given that the coordinates of the pivot point are x_p and y_p, respectively, the moments of the air bearing acting on the slider surface about the pivot point P are:

$$M_{airbearing\_x} = \iint_A p(x,y)(x - x_p)dA$$

$$M_{airbearing\_y} = \iint_A p(x,y)(y - y_p)dA$$

Rewriting equations (3.26) in matrix form we obtain

$$\begin{bmatrix} k_z & 0 & 0 \\ 0 & k_\alpha & 0 \\ 0 & 0 & k_\beta \end{bmatrix} \begin{Bmatrix} dh \\ d\alpha \\ d\beta \end{Bmatrix} = \begin{Bmatrix} \iint_A p(x,y)dA - F_z^{pre-load} \\ \iint_A p(x,y)(x - x_p)dA - M_\alpha^{pre-load} \\ \iint_A p(x,y)(y - y_p)dA - M_\beta^{pre-load} \end{Bmatrix} \tag{3.29}$$

Solving the Reynolds equations and the slider equilibrium equations allows calculation of the steady-state air bearing pressure distribution *p(x,y)* and the flying characteristics of the slider, *h(x,y)*, α, and β.

At a flying height of approximately 5 nm, additional forces between slider and disk surfaces become increasingly more important and cannot be neglected anymore. Among the intermolecular forces, the Van-der-Waals force [84], [138]–[142] is the dominant one that is caused mostly from the dispersion force between the atoms. Even though the dipole moment of an atom is zero, instantaneous positions of the electrons around the nuclear proton induces an electrical dipole, allowing the two atoms to attract each other. At infinite distance between two atoms, the intermolecular force is negligibly small. As the distance decreases, the intermolecular force is first an attractive force. Its strength increases with

decreasing distance until it reaches a maximum. If the distance is further decreased, the intermolecular force decreases and becomes a repulsive force. Its strength increases significantly if the distance approaches zero. The Van-der-Waals force is derived from the Lennard-Jones potential energy [139], [143], in which the attractive force and repulsive force *w* are generally described using an inverse sixth and twelfth order power term as follows:

$$w = -\frac{C}{r^6} + \frac{D}{r^{12}} \tag{3.30}$$

, where $C = 10^{-77}\, Jm^6$ and $D = 10^{-134}\, Jm^{12}$ are two constants in vacuum and *r* is the distance between two molecules of the slider and the disk. Integrating equation (3.28) through the disk surface area, we obtain the potential energy between the slider and the disk as shown below:

$$W = -\frac{\pi C \rho_1}{6h^3} + \frac{\pi D \rho_1}{45h^9} \tag{3.31}$$

In equation (3.29), ρ_1 is the density of the disk, and h is the spacing between the slider and the disk. Integrating again over the slider volume, we obtain the total potential energy between the slider and the disk given as:

$$W_{slider-disk} = -\frac{\pi C \rho_1 \rho_2}{6} \iint_A dA \int_h^\infty \frac{1}{z^3} dz + \frac{\pi D \rho_1 \rho_2}{45} \iint_A dA \int_h^\infty \frac{1}{z^9} dz \tag{3.32}$$

, where ρ_2 is the density of the slider. The potential energy between the slider and the disk is rewritten as:

$$W_{slider-disk} = -\frac{\pi^2 C \rho_1 \rho_2}{12\pi} \iint_A \frac{1}{z^3} dxdy + \frac{\pi^2 D \rho_1 \rho_2}{360\pi} \iint_A \frac{1}{z^9} dxdy \tag{3.33}$$

Differentiating the total potential energy, we obtain the intermolecular force between the slider and the disk as:

$$F_{Van-der-Waals} = \frac{\partial W_{slider-disk}}{\partial z} = \frac{\pi^2 C \rho_1 \rho_2}{6\pi} \iint_A \frac{1}{z^3} dxdy - \frac{\pi^2 D \rho_1 \rho_2}{45\pi} \iint_A \frac{1}{z^9} dxdy \qquad (3.34)$$

In equation (3.32), the first term is the attractive Van-der-Waals force, and the second term is the repulsive Van-der-Waals force. As the head disk spacing is approximately 10nm, the Van-der-Waals force is an attractive force. It becomes a repulsive force only when the head disk spacing is below 0.32nm [138], [139], [144].

In recent years, a significant improvement of the tribological performance has been observed after voltage biasing is applied to the head-disk interface. Knigge et al [144] showed that the application of voltage across the head-disk interface reduced wear of the slider surface. Tani et al [145] performed "flyability" testing using different types of lubricants and different bias voltage levels to the slider with respect to the disk. They observed that lubricant pickup was decreased when the slider is negatively biased with respect to the disk. Clearly, in the presence of a bias voltage, there exists an electrostatic force between head and disk surfaces. The electrostatic force between head and disk is similar to the force acting on capacitor plates. The electrostatic force is given by the equation below, where ε_0 and ε_r are vacuum and relative permittivity of an air bearing, V is an applied voltage, h is the distance between the head and the disk, and A is the interfacial area of the head:

$$F_{Electrostatic} = \varepsilon_0 \varepsilon_r V^2 \iint_A \frac{1}{2h^2} dA \qquad (3.35)$$

In the presence of Van-der-Waals and electrostatic forces between the head and the disk surface, the Reynolds equation with slip boundary conditions and the slider equilibrium equations can be rewritten as:

$$\nabla.\left(\overline{Q}ph^3\nabla p\right) = 6\mu u.\nabla(ph) + 12\mu\frac{\partial(ph)}{\partial t} \tag{3.36}$$

$$\begin{bmatrix} k_z & 0 & 0 \\ 0 & k_\alpha & 0 \\ 0 & 0 & k_\beta \end{bmatrix} \begin{Bmatrix} dh \\ d\alpha \\ d\beta \end{Bmatrix} = \begin{Bmatrix} \iint_A p(x,y)dA - \iint_A (F_{Van-der-Waals}(x,y) + F_{Electrostatic}(x,y))dA - F_z^{pre-load} \\ \iint_A \left[p(x,y) - F_{Van-der-Waals}(x,y) - F_{Electrostatic}(x,y) \right](x - x_p)dA - M_\alpha^{pre-load} \\ \iint_A \left[p(x,y) - F_{Van-der-Waals}(x,y) - F_{Electrostatic}(x,y) \right](y - y_p)dA - M_\beta^{pre-load} \end{Bmatrix}$$

As a result, the flying characteristics of a slider, including the minimum flying height, as well as the pitch and roll angles, can change in the presence of Van-der-Waals and electrostatic forces.

The Reynolds equation is a nonlinear partial differential equation which does not have a closed form solution. As the slider designs become increasingly more complicated, numerical methods must be used to solve the Reynolds equation and the slider equilibrium equations simultaneously. In our research group at the Center for Memory and Recording Research (CMRR), University of California San Diego, we have developed a software package has been developed to simultaneously solve the Reynolds equation and the slider equilibrium equations using Finite Element Analysis (FEA) [146]. The slider surface is discretized into small elements which are assembled and used to solve the unknown pressure at each node.

3.3 Effects of Van-der-Waals and Electrostatic Forces on the Flying Characteristics of a Slider

In this study, a commercially available slider design is used (Figure 3.4). The air bearing surface of the slider features multiple areas with different shapes and depths. High and low pressure distribution on the slider surface are formed at the air bearing, allowing the slider to fly over the disk surface at just a few nanometers. The air bearing contour is designed so that the flying height of the slider is nearly independent of the disk radius and disk velocity.

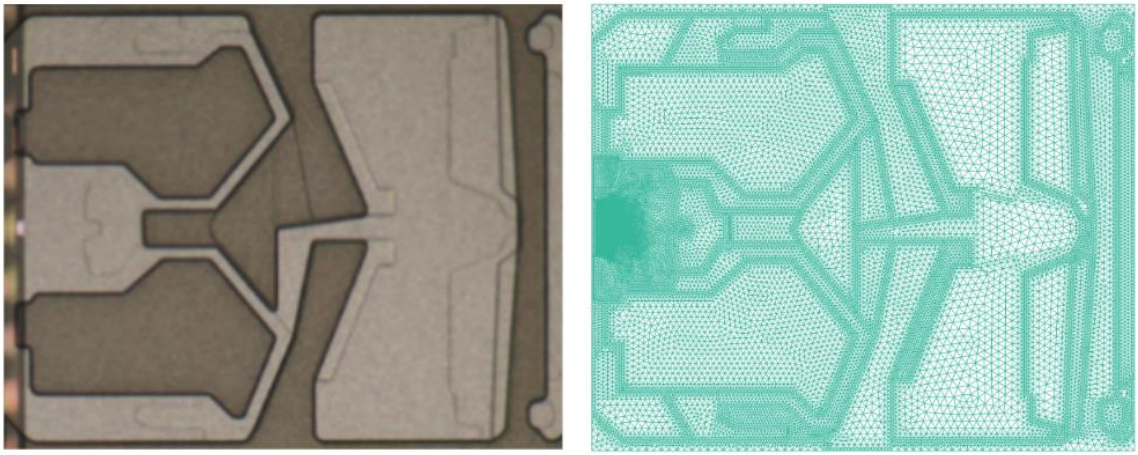

Figure 3.4 Air bearing surface and its mesh using HyperMesh software

Discretization of the slider surface into small triangular elements is performed using a commercially available meshing program (Altair Hypermesh) as shown in Figure 3.4. The disk surface is assumed to be flat. Simultaneously solving the Reynolds equation and slider equilibrium equations is performed using the CMRR air bearing simulator [116], [130]. Figure 3.5 shows a typical pressure distribution for the slider air bearing obtained with the CMRR air bearing simulator. We observe that the pressure distribution is highest at the read and write transducer element where the flying height is a minimum. The pressure at the recessed area is smaller than the ambient pressure.

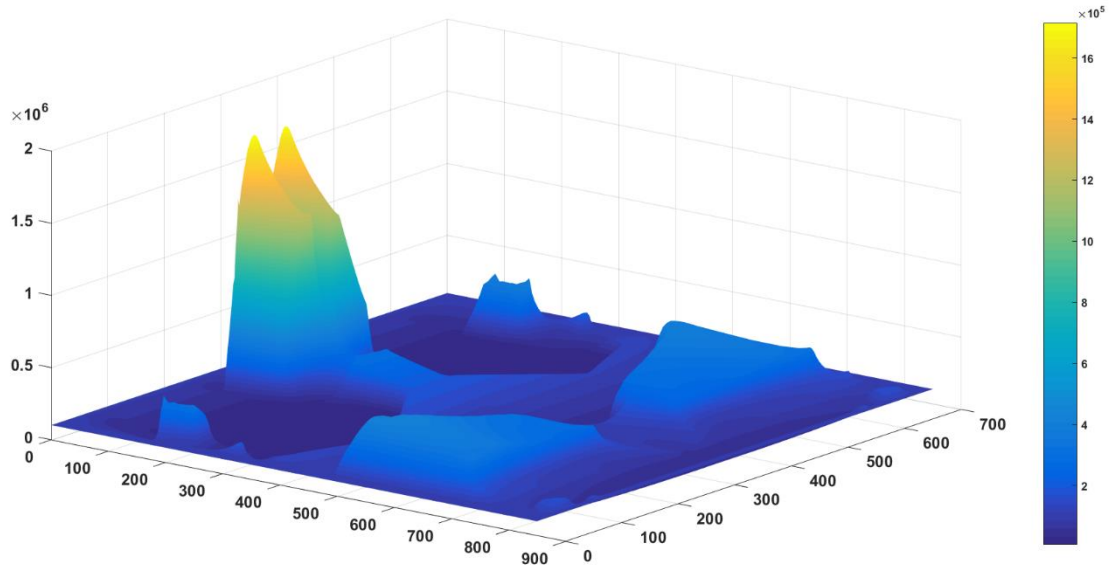

Figure 3.5 Pressure distribution over the air bearing surface of the slider. Maximum pressure is observed at the read and write transducer area near the trailing edge of the slider

Table 1 shows the change of the minimum flying height of the slider due to the presence of the Van-der-Waals and electrostatic forces. We observe that the flying height of the slider decreases by only 0.03nm in the presence of Van-der-Waals force. If a bias voltage of 1V is applied across the head-disk interface, the minimum flying height of the

slider changes by approximately 0.5nm (Figure 3.6 (a)). In addition, the pitch angle decreases, and the roll angle increases as the bias voltage increases as shown in Figure 3.6 (b) and (c). Figure 3.6 (d) shows that the electrostatic force increases faster than the Van-der-Waals force when the bias voltage increases from 0 to 2V.

Table 3.1 The effect of Van-der-Waals and Electrostatic Forces on minimum flying height of the slider

Molecular Effect	Voltage (V)	Minimum Flying Height (nm)	Van-der-Waals Force (N)	Electrostatic Force (N)
NO	0	12.17931477	0	0
YES	0	12.14818521	3.8753E-05	0
YES	0.1	12.14338117	3.87842E-05	7.445E-06
YES	0.3	12.10486911	3.90363E-05	6.72455E-05
YES	0.5	12.02741389	3.95502E-05	0.000188148
YES	0.7	11.91012554	4.03463E-05	0.000372848
YES	1	11.65622725	4.21471E-05	0.000779441
YES	2	10.00033988	5.71359E-05	0.003679924

From table 1 we observe that the minimum flying height of the slider decreases by approximately 2nm if the bias voltage increases from 0 to 2V. At the same time, the pitch angle decreases by approximately $1\,\mu rad$, while the roll angle increases by $0.5\,\mu rad$. More importantly, we observe that if the bias voltage is less than 0.2V, the Van-der-Waals force is larger than the electrostatic force between the head and the disk. However, if the bias voltage becomes larger than 0.2V, the electrostatic force becomes increasingly larger

compared to the Van-der-Waals forces. Clearly, as the bias voltage is large the effect of the electrostatic forces on the flying characteristics of the slider is no longer negligible.

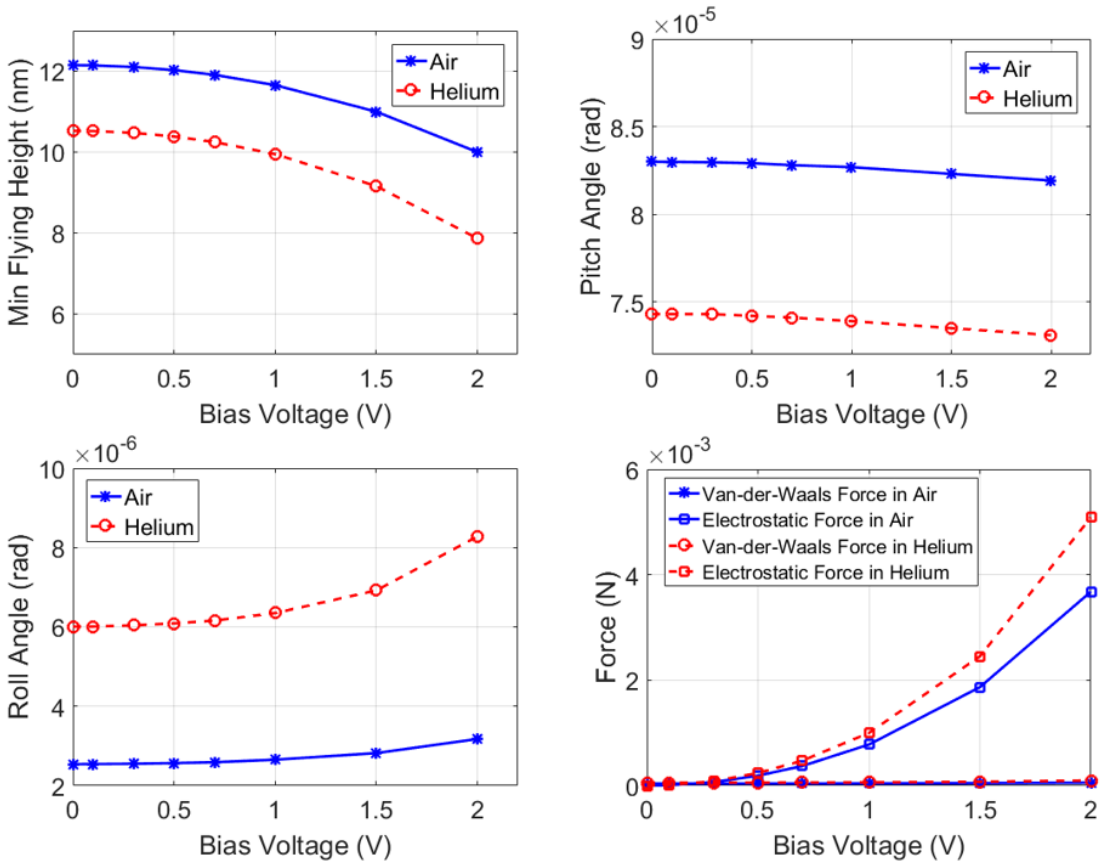

Figure 3.6 The effect of bias voltage on the flying characteristics (a) minimum flying height (b) pitch angle and (c) roll angle of the slider. A comparison of the Van-der-Waals and Electrostatic forces in air and helium is shown in (d)

A similar simulation as the one discussed previously in air was performed in helium environment to study the effect of bias voltage in helium environment compared to in air. As discussed in chapter (2.2.4), helium has similar viscosity as air. Helium is lighter than air. In addition, the mean free path of helium is much larger than that of air. It is seen that in helium, the minimum flying height of the slider under consideration decreased by approximately 1.5nm, while the pitch angle decreased by $1\,\mu rad$ and the roll angle increased by $0.3\,\mu rad$. Similarly, in a helium environment, the Van-der-Walls force is

much smaller compared to the electrostatic force as the bias voltage exceeds 0.2V. Our simulation results show excellent agreement with the results presented by Knigge [144].

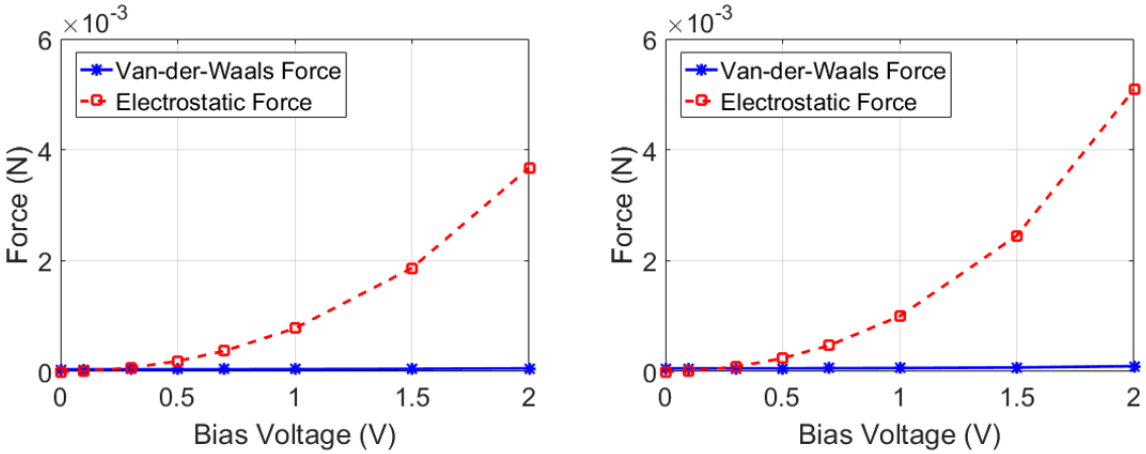

Figure 3.7 Van-der-Waals and Electrostatic Forces in (a) air and (b) helium in the presence of bias voltages

3.4 Summary

In this chapter, the Reynolds and slider equilibrium equations were derived that are used to calculate the pressure distribution at the head-disk interface. The effect of Van-der-Waals and electrostatic forces on the Reynolds and slider equilibrium equations are studied. Our study shows that the electrostatic force is approximately 16 times stronger than the Van-der-Waals force that greatly affects the flying characteristics of the slider. As the bias voltage increases, the minimum flying height of the slider decreases. Similarly, the pitch angle decreases while the roll angle increases.

Chapter 4

Effect of Air and Helium on the Head-Disk Interface during Load-Unload

4.1 Introduction

In the last 60 years, the storage capacity and reliability of the hard disk drives (HDDs) have been improved significantly by incorporating advanced technologies into those small devices. Two of the technologies are helium-filled and ramp load-unload technologies. Helium-filled hard disk drives have recently been commercialized. The low density of helium compared to air reduces turbulence effects inside the disk drive enclosure, allowing greater accuracy in track-seeking and track-following [147]. Aruga et al. [70] showed that flow-induced positioning errors decrease by 50% in helium compared to air due to the laminar flow of helium versus the turbulent flow of air. Bouchard et al. [64] measured the non-repeatable flutter amplitude of recording disks using laser Doppler interferometry and concluded that disk flutter was reduced by more than 30% in helium compared to air. Thus, more disks can be packed in the same space in a helium-filled drive than in an air-filled drive. In addition, the thermal conductivity of helium is six times higher than that of air, resulting in a smaller temperature increase in a helium-filled drive than in a conventional air-filled drive [148]. The reduced power dissipation and lower cooling

costs are important considerations for large data centers. The main drawback for the use of helium in a disk drive are the difficulties encountered in sealing the HDD enclosure.

The ramp load-unload technology is universally used in today HDDs. The ramp load-unload technology has significant advantages in terms of tribological performance of the head-disk interface (HDI), power consumption, and shock robustness in comparison with contact start-stop technology. In ramp load-unload technology, the slider is loaded from a ramp onto the recording disk when the HDD is powered on. During shut-down of the drive, the slider is unloaded from the disk surface and the suspension is supported on the load-unload ramp. The load-unload process is important for the reliability of the head-disk interface and has been the subject of a number of investigations. Levi et al. [149] investigated head-disk contacts during load-unload as a function of vertical load speed of the slider. Weissner et al. [150] studied the effect of load speed and slider design on head-disk contacts during the load-unload process using laser Doppler vibrometry. Tambe et al. [151] experimentally investigated the HDI performance as a function of disk velocity, slider load speed, spindle speed, suspension design and ramp z-height. Lee et al. [152] studied the effect of pitch static angle and roll static angle on the stability of the slider during the load process. Liu et al. [153] used a temperature-dependent thin magnetic film (TbFeCo) on the disk surface to track head-disk contacts during the load-unload process. They concluded that suspension vibrations play a dominant role on head-disk contacts. The ramp load-unload process was simulated numerically by Peng [154] and Hongrui et al. [155]. However, all of the above studies focused on the tribological characteristics of the HDI in conventional air-filled HDDs. No studies have been reported in the literature on the

performance of the head-disk interface in a helium environment during the load-unload process.

In this paper, head-disk contacts are investigated during the load-unload process in air and helium as a function of the pitch and roll static angle between slider and disk. The acoustic emission (AE) signal and the change in the rotational speed of the spindle were used to detect the presence of head-disk contacts. Scanning electron microscopy and optical surface analysis were used to characterize wear of the carbon overcoat on the slider surface and to study lubricant redistribution on the disk surface after 10,000 load-unload cycles in air and helium. Fast Fourier Transform (FFT) of the high speed AE signal was performed to characterize pitch and roll mode frequencies of the slider during load-unload. Head-disk contacts were found to be substantially reduced in helium environment compared to air environment during the load and unload process.

4.2 Experimental Set-up

4.2.1 Experimental Tester and Environmental Chamber

A schematic of the custom-made experimental set-up is shown in Fig. 1, consisting of a disk mounted on a spindle, and an actuator arm carrying the suspension with the slider. The disk can be tilted in two mutually perpendicular planes using goniometers. Tilting of the disk allows a change in the pitch static angle (PSA) and the roll static angle (RSA) between slider and the disk. The definition for positive and negative roll static angles are shown in Fig. 2a and 2b, respectively. An acoustic emission (AE) sensor was attached to the actuator arm to detect head-disk contacts during the load-unload process. The AE signal

was acquired using a high speed analog channel (2 MHz). An optical encoder was mounted on the spindle to measure the spindle rotational speed.

The experimental tester was enclosed in a sealed environmental chamber (Fig. 1). A temperature-controlled plate located under the tester and two temperature probes were used to measure the temperature in the chamber. Two mass flow controllers were used to control the relative humidity inside the chamber. The chamber pressure was adjusted and measured using a pressure sensor. Helium and oxygen sensors were positioned inside the chamber to determine the percentage of helium and air. Both sensors were calibrated before conducting the experiments. Sealed connection boards and O-rings were used to prevent helium from leaking out of the chamber during the experiments.

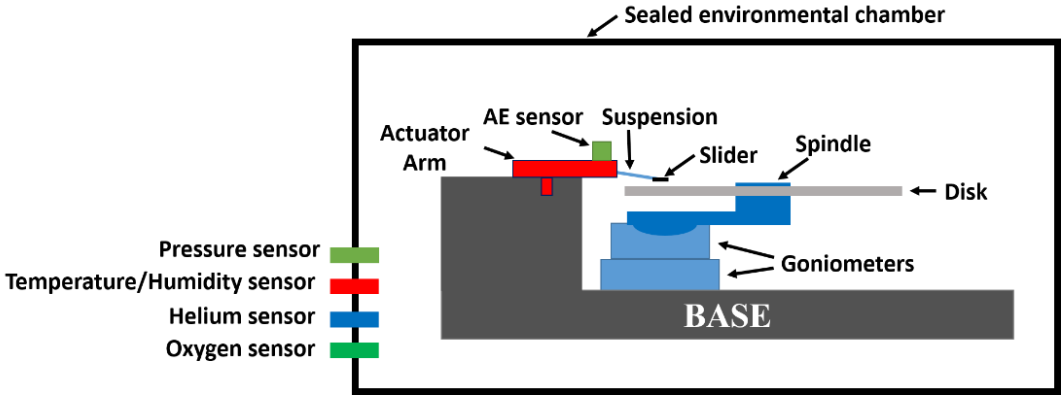

Figure 4.1 Schematic of experimental tester inside a sealed environmental chamber

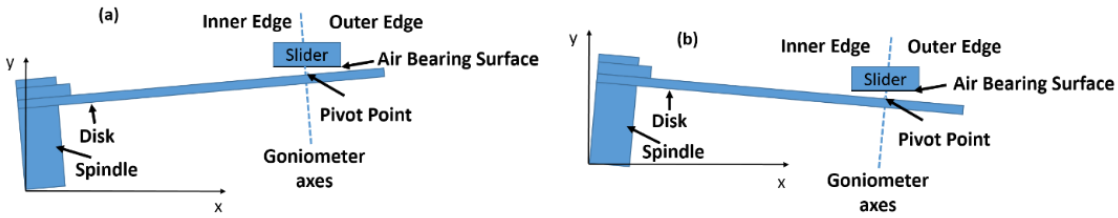

Figure 4.2 Schematic of the head-disk interface at (a) positive RSA (spacing at the inner edge of the slider is larger than at the outer edge) and (b) negative RSA (spacing at the inner edge of the slider is smaller than at the outer edge)

4.2.2 Disk and Slider Samples

Commercially available aluminum disks of 3.5 inches (95 mm) diameter and 50 mils (1.27 mm) thickness were used in the experiments. The disk was coated with an 18 Angstrom thick diamond-like carbon (DLC) protective layer and a 12 Angstrom thin perfluoropolyether (demnum, Daikin Industries, Ltd) lubricant. The bonded-lubricant ratio of the disk was about 80%. The slider surface was coated with a protective carbon overcoat (DLC) of approximately 2 nm. In Fig. 3, the schematic of the air bearing surface of the slider is shown. We denote the leading edge of the slider by LE, the trailing edge by TE, and OE and IE denote the outer and inner edge of the slider, respectively. The nominal pitch and roll static angle of the sliders used in the experiments were 0.9 degrees and 0 degrees, respectively. The same air bearing contour was used for the experiments in air and helium, respectively.

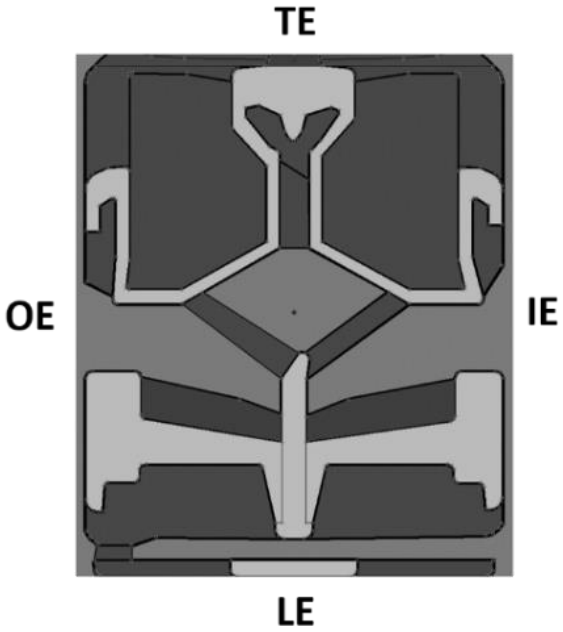

Figure 4.3 Air bearing surface of the slider

4.2.3 Pitch and Roll Angle tests and Load-Unload Tests

In our study, a load-unload cycle consists of the following steps: First, the disk was spun up to 5,400 rpm. Thereafter, the slider was moved from the ramp to the outer diameter of the disk at a speed of 3 inches/s (~75 mm/s). Then, the slider was flown at the outer diameter for 200 milliseconds before it was unloaded at a speed of 3 inches/s (~75 mm/s) onto the ramp. The slider remained on the ramp for 200 milliseconds before the cycle was repeated.

"Pitch and roll angle" tests were performed to investigate the effect of pitch static angle (PSA) and roll static angle (RSA) on head-disk contacts during the load-unload process. The pitch static angle was adjusted from 0.5 degrees to 3.5 degrees in steps of 0.2 degrees, and the roll static angle from -3.0 degrees to 3.0 degrees in steps of 0.2 degrees. For each combination of pitch and roll static angle, five load-unload cycles were performed. During these load-unload cycles, the acoustic emission (AE) signal and the rotational speed of the spindle were measured. The root mean square of the AE signal (AE_{rms}) and the decrease of spindle speed (ΔRPM) were used to characterize the presence of head-disk contacts. During head-disk contacts the rotational spindle speed decreases due to the increased friction force between slider and disk. In this paper, the decrease of spindle speed is measured using a high precision optical encoder. Three pitch and roll angle tests were performed on the same disk and the same slider at different air/helium concentrations. The test conditions are summarized in Table 1. During the tests, the temperature, pressure and relative humidity inside the chamber were kept constant (30°C, 10%RH, 101,000Pa) while the air/helium content inside the chamber was varied.

Table 4.1 Environmental conditions for "pitch and roll angle" (PRA) testing

PRA Test	Chamber Content	
	Air (%)	Helium (%)
1	0	100%
2	40	60%
3	100	0%

"Load-unload" tests consisting of 10,000 load-unload cycles were performed to monitor the presence of head-disk contacts at a fixed pitch and roll static angle combination. In a typical load-unload test, the disk was initially adjusted to the desired pitch and roll static angle. Thereafter, 10,000 load-unload cycles were performed and the AE_{rms} and the ΔRPM signals were measured for every ten successive load-unload cycles. A new disk and a new slider were used for each load-unload test. Load-unload tests were carried out inside the environmental chamber at constant temperature, constant relative humidity and constant pressure (30°C, 10%RH, sea-level pressure 101,000Pa) for air and helium.

4.3 Experimental Results and Discussions

4.3.1 Effect of the Pitch Static Angle and the Roll Static Angle

Fig. 4 shows contour maps of the average AE_{rms} signal as a function of the pitch and roll static angle, while Fig. 5 shows contour maps of the average change in rotational speed ΔRPM as a function of the pitch and roll static angle. The black region in the middle

of Fig. 4 represents the region where the AE_{rms} signal is close to zero, i.e., where contacts are absent between slider and disk. This region is denoted as the "permissible" or "safe" region for the load-unload process. The gray and white regions surrounding the black region represent regions of increasingly larger AE_{rms} values, indicating the presence of head-disk contacts. In Fig. 5, the black region in the middle of the figure corresponds to a region with near zero change in rotational spindle speed ΔRPM. Clearly, in this area head-disk contacts are absent. The black region in Fig. 5 is similar in size and shape to the black region in Fig. 4, indicating that the AE_{rms} and ΔRPM signals are correlated. The gray and white regions in Fig. 5 denote areas of increasing ΔRPM, i.e., regions of increasing change in spindle speed due to head-disk contacts. In this study, the threshold for detecting head-disk contacts during load-unload was chosen based on industry standards to be 0.055V for the acoustic emission signal and 0.6rpm for ΔRPM measurements, respectively.

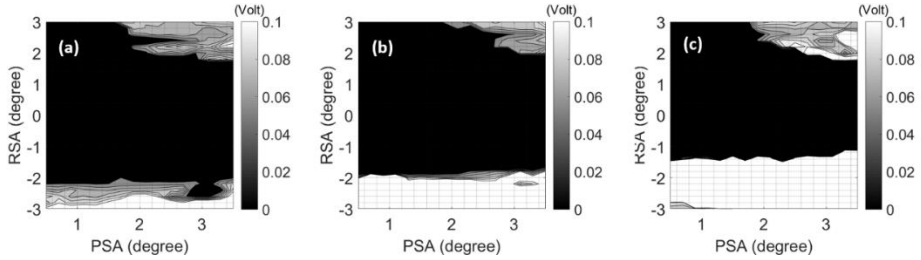

Figure 4.4 Contour maps of the AE_{rms} signal as a function of PSA and RSA in (a) 100% helium (b) 60% helium (c) 0% helium

Figure 4.5 Contour maps of the ΔRPM signal as a function of PSA and RSA in (a) 100% helium (b) 60% helium (c) 0% helium

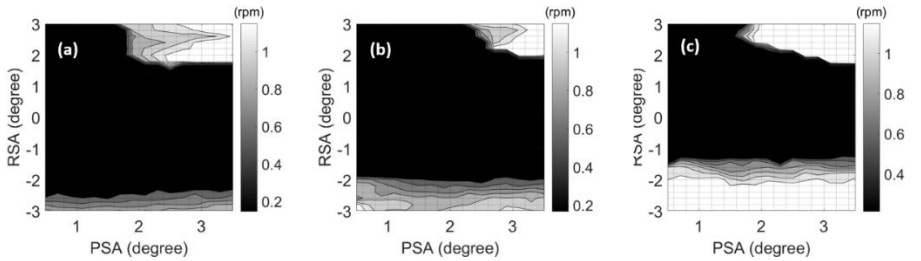

From the contour maps in Fig. 4 and Fig. 5, we observe that head-disk contacts occur at high pitch static angle and high roll static angle and at large negative roll static angle. Clearly, head-disk contacts are a strong function of the pitch static angle and the roll static angle between the slider and the disk. As the helium percentage decreases the permissible region decreases in size. This is especially noticeable at negative roll static angles. At a "nominal" pitch static angle of 0.9 degrees, the roll static angle of the permissible region in helium is -2.2 degrees, while in air the permissible roll static angle is -1.4 degrees. At a nominal roll static angle of 0 degrees, head-disk contacts are absent for all pitch static angles investigated in both air and helium. This result shows that the roll static angle has a stronger effect on head-disk contacts than the pitch static angle. This observation is in agreement with Pan et al. [13] who studied lubricant transfer between disk and slider as a function of pitch and roll static angle of the slider. In their study, they concluded that the roll static angle has a stronger effect on lubricant transfer from the disk to the slider surface than the pitch static angle.

4.3.2 Load-Unload test

The pitch and roll angle results suggest that the flying characteristics of a slider is strongly affected by air and helium during the load-unload process. Load-unload tests were performed at four combinations of the pitch and roll static angle, in which the pitch static angle was kept constant at a nominal value of 0.9 degrees and the roll static angle was adjusted to be 0 degrees;-0.9 degrees;-1.4 degrees; and -1.9 degrees, respectively.

Fig. 6 shows the average AE_{rms} and ΔRPM during 10,000 load-unload cycles as a function of the roll static angle in air and helium. For roll static angles between 0 degrees and -0.9 degrees, the average AE_{rms} and ΔRPM values in air and helium are very small, i.e., head-disk contacts are absent in both air and helium. We note, however, that the average ΔRPM in helium is slightly smaller (0.05rpm) than that in air. This result is explained by the lower density and the laminar flow characteristics of helium, resulting in a smaller drag force on the disk surfaces in helium than in air. As the roll static angle decreases, the average AE_{rms} value increases, indicating increasing head-disk contacts in both air and helium. From Fig. 6, we observe that the average values of the AE_{rms} and ΔRPM signals are larger in air than in helium. This suggests that head-disk contacts in air are stronger than in helium, i.e., the slider flies more stably in helium than in air during load-unload keeping the pitch and roll static angles unchanged.

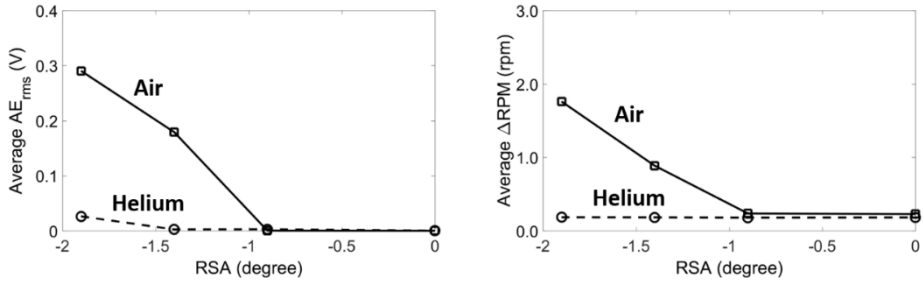

Figure 4.6 Average of the AE_{rms} signal and the ΔRPM signal in air (solid) and in helium (dashed)

Fig. 7 and 8 show the change in spindle speed, ΔRPM, for 10,000 load-unload cycles in air and helium, respectively, as a function of roll static angle. A change in spindle speed of 0.6 rpm was chosen as the threshold for detecting head-disk contacts, i.e., if the change in spindle speed ΔRPM was smaller than 0.6 rpm, head-disk contacts are considered to be absent. We observe from Fig. 6 that the change in spindle speed ΔRPM in air was largest for a roll static angle of -1.9 degrees. At a roll static angle of -1.4 degrees, the change

in spindle speed ΔRPM was smaller than at -1.9 degrees. At roll static angles of -0.9 degrees and 0 degrees, the change in spindle speed ΔRPM is smaller than the threshold, i.e., contacts are absent. In helium, head-disk contacts were absent at all roll static angles investigated. This result confirms that head-disk contacts are stronger in air than in helium for the same combination of pitch and roll static angles.

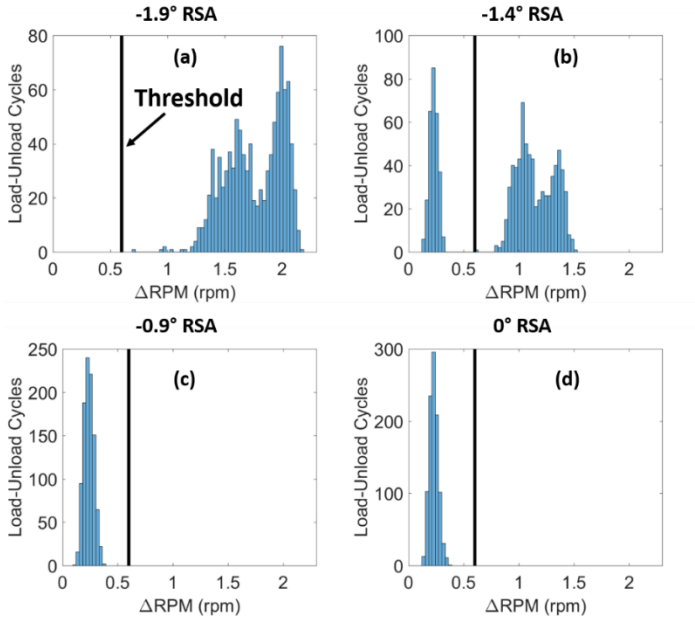

Figure 4.7 Change in spindle speed ΔRPM in air as a function of roll static angle (a) -1.9° RSA (b) -1.4° RSA (c) -0.9° RSA **(d) 0° RSA**

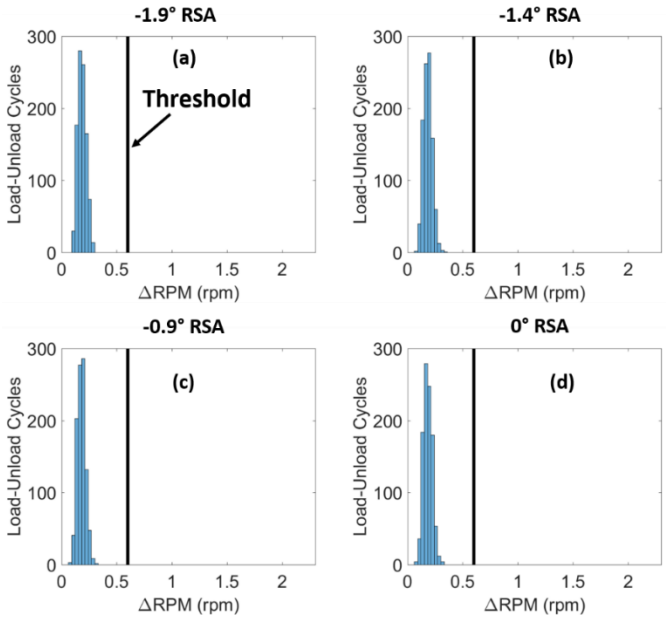

Figure 4.8 Change in spindle speed ΔRPM in helium as a function of roll static angle (a) -1.9° RSA (b) -1.4° RSA (c) -0.9° RSA (d) 0° RSA

4.3.3 Scanning Electron Microscopy and Optical Surface Analyzer Results

After load-unload testing, a high resolution scanning electron microscope (Zeiss, Ultra-60, Germany) and an optical surface analyzer (KLA-Tencor, Candela 6100, USA) were used to analyze slider and disk surfaces. Wear on the slider surface was investigated using a low-energy electron beam of 1.0 kV. A typical SEM image of the air bearing surface is shown in Fig. 9. Wear and scratches are absent near the center region of the sliders, where the read and write elements are located (Fig. 9). Worn areas and scratches can only be seen near the trailing edge and the inner edge of the sliders, marked X, indicating the area where head-disk contacts occurred.

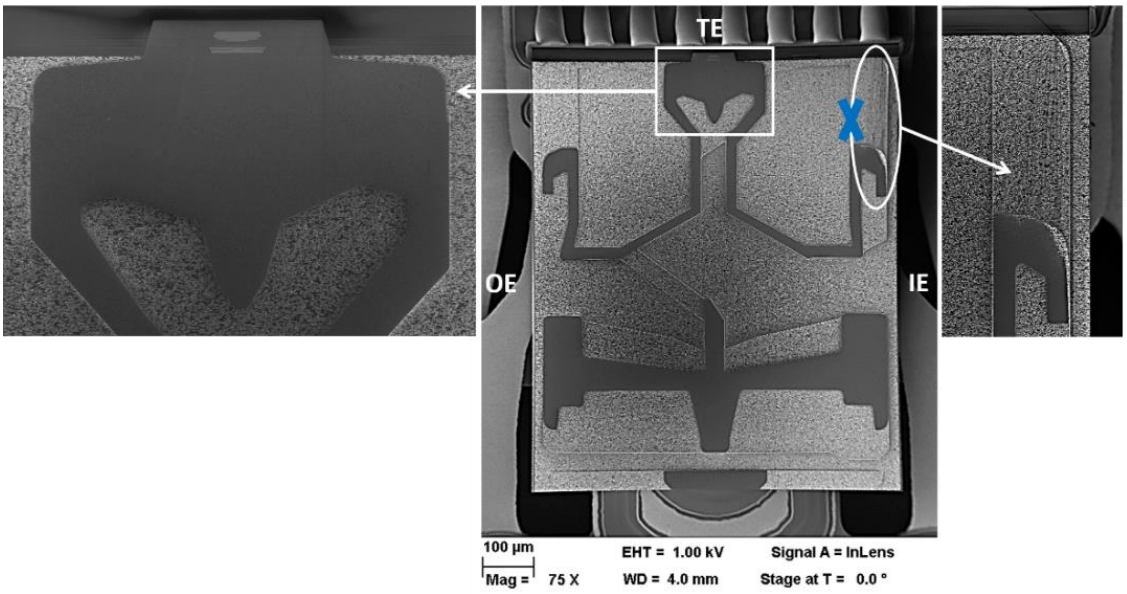

Figure 4.9 Typical SEM image of an air bearing surface after load-unload tests

Figure 10 and Figure 11 show SEM images of the slider surface after load-unload testing in air and helium as a function of the roll static angle. In air, wear and scratches are seen at a roll static angle of -1.9 degrees, indicating contacts between the slider and the disk. At a roll static angle of -1.4 degrees, wear and scratches are still visible but much less severe as compared to those at a roll static angle of -1.9 degrees. Substantially less wear is present and scratches are completely absent at a roll static angle of -0.9 degrees. In helium, wear is visible at a roll static angles of -1.9 degrees, -1.4 degrees and -0.9 degrees but no scratches are visible. We hypothesize that wear of the slider surfaces in helium is due to intermittent contacts during the 10,000 load-unload cycles. At a roll static angle of 0 degrees, wear and scratches are absent in both air and helium. Clearly, wear and scratches of the slider surface in helium are much less pronounced compared to air, indicating that head-disk contacts are reduced in helium compared to air.

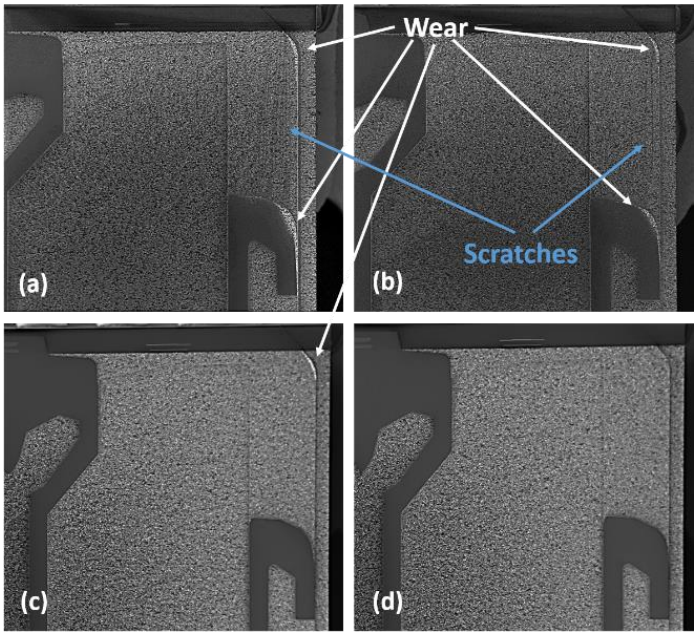

Figure 4.10 SEM images of air bearing surfaces after load-unload testing in air (a) -1.9 degrees RSA (b) -1.4 degrees RSA (c) -0.9 degrees RSA (d) 0 degrees RSA

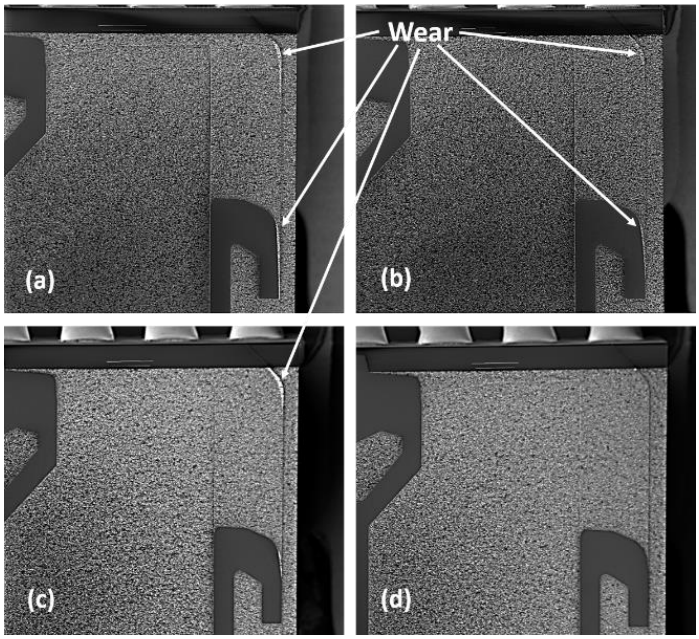

Figure 4.11 SEM images of air bearing surfaces after load-unload testing in helium (a) -1.9 degrees RSA (b) -1.4 degrees RSA (c) -0.9 degrees RSA (d) 0 degrees RSA

During slider-disk contacts, lubricant redistribution is likely to occur. To analyze lubricant redistribution on the disk surfaces after load-unload testing, an optical surface

analyzer (Candela 6100) was used. In our experiments, the so-called “Q phase” channel of the optical surface analyzer was used to measure the thickness variation of the lubricant film on the disk surfaces. Figures 12 and 13 show images of the lubricant film thickness near the outer diameter of the disk, where load-unload testing was performed. In air, lubricant redistribution was observed at roll static angles of -1.9 degrees, -1.4 degrees and -0.9 degrees, respectively. At -1.9 degrees roll static angle, lubricant redistribution was found at locations corresponding to the inner and outer edge of the slider (Fig. 12). Lubricant redistribution at the inner edge of the slider is clearly visible, indicating the location where head-disk contacts occur. At roll static angles of -1.4 degrees and -0.9 degrees, respectively, lubricant redistribution is observed only at the inner edge of the slider. Clearly, the lubricant redistribution is a consequence of head-disk contacts in air. In helium, lubricant redistribution was absent at all roll static angles investigated. This, clearly, indicates that head-disk contacts are either absent in helium or less strong than in air. Interestingly, at roll static angles of -0.9 degrees and 0 degrees, we observe that lubricant moguls appear on the disk surface in a helium environment. It is likely that this result is a consequence of the lower flying height of the slider in helium compared to air (Liu et al. [148]).

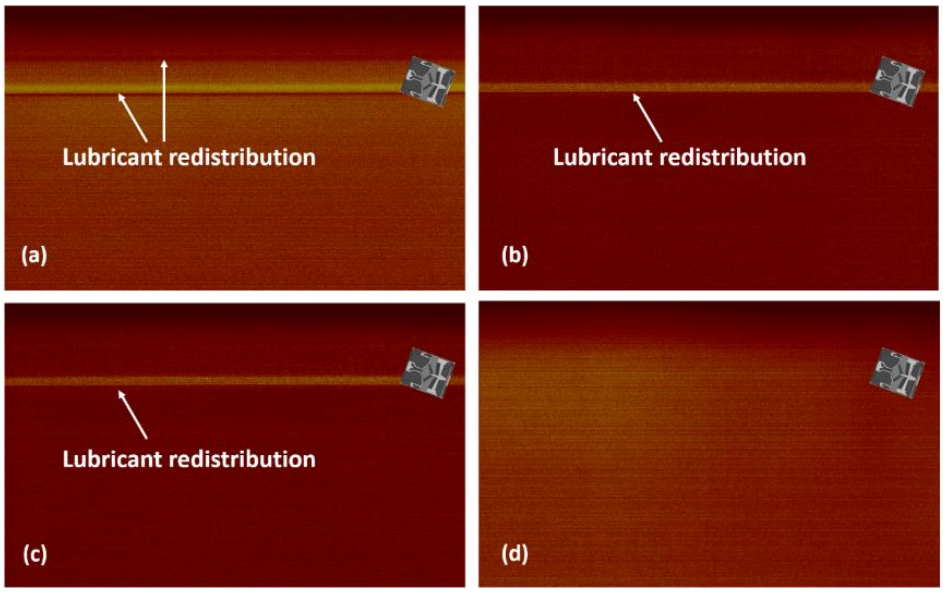

Figure 4.12 Lubricant redistribution after the load-unload tests in air (a) -1.9^0 RSA (b) -1.4^0 RSA (c) -0.9^0 RSA (d) 0^0 RSA

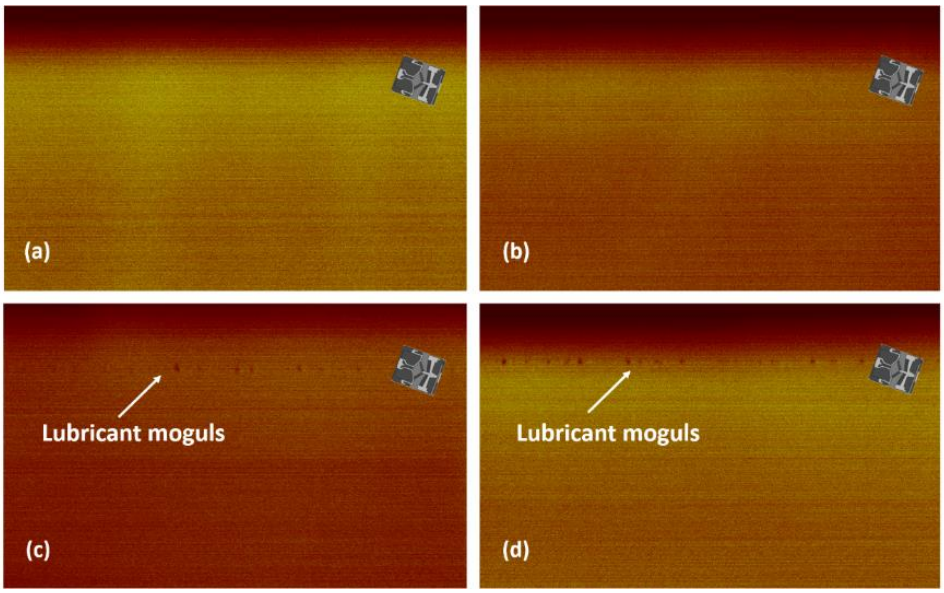

Figure 4.13 Lubricant redistribution after the load-unload tests in helium (a) -1.9^0 RSA (b) -1.4^0 RSA (c) -0.9^0 RSA (d) 0^0 RSA

4.3.4 Slider Vibration Frequencies during Load-Unload

The vibration frequencies of the sliders investigated was studied using Fast-Fourier Transform (FFT) of the AE signal during load-unload testing. Fig. 14 and Fig. 15 show the magnitude of the power spectrum of the AE signal as a function of frequency in air and in helium at a roll static angle of -1.9 degrees. In air, frequencies of 145 kHz, 300 kHz, 380 kHz and 430 kHz were observed. The maximum amplitude occurred at a frequency of 145 kHz corresponding to the first pitch mode of the slider. The frequencies of 300 kHz, 380 kHz correspond to the second pitch and roll modes of the slider in air, respectively. In helium, the frequency at 145 kHz was not excited due to the absence of head-disk contacts. Frequencies of 320 kHz and 360 kHz were observed in helium during load-unload that are likely to correspond to the second pitch and roll mode of the slider in helium. Tang et al. [156] reported the first pitch mode frequency of 142.9 kHz and the second pitch mode frequency of 293.4 kHz in air and the second pitch mode frequency of 352.2 kHz in helium. Xu et al. [157] used laser Doppler vibrometry (LDV) and observed the frequency of 142 kHz during head-disk interaction. Knigge et al. [144] concluded that the first and second pitch mode of the slider were approximately 120 kHz and 320 kHz. Clearly, our first and second pitch mode frequencies of our experimental data are in the same range as previous studies [144], [156], [157].

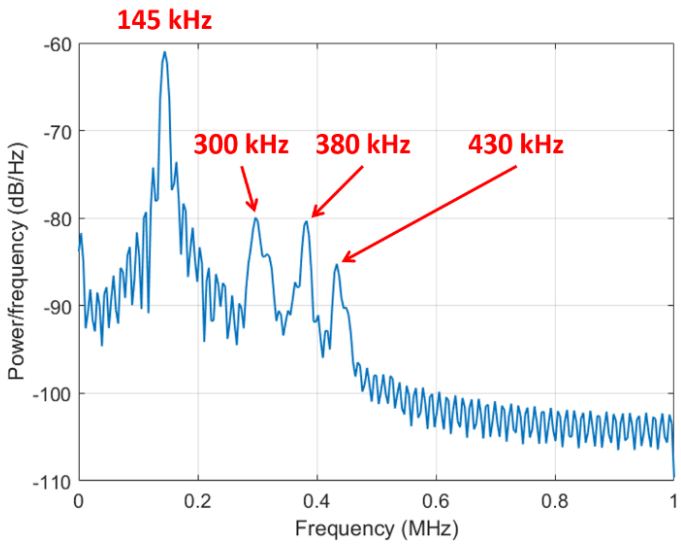

Figure 4.14 Peak frequencies of the slider in air at -1.9 degrees RSA

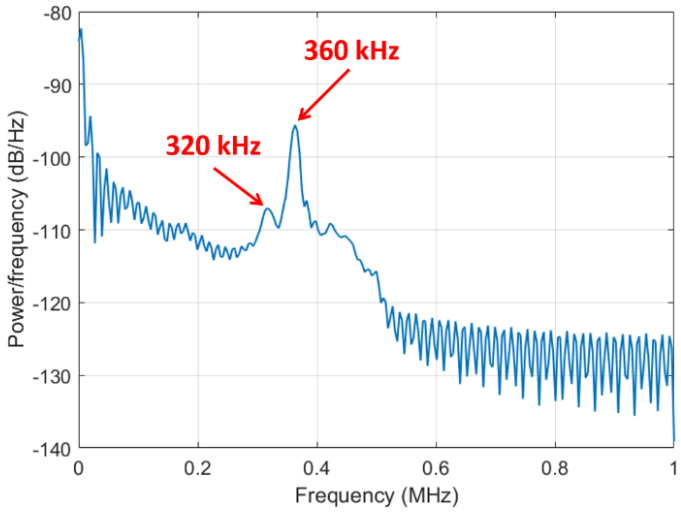

Figure 4.15 Peak frequencies of the slider in helium at -1.9 degrees RSA

4.4 Discussion

Head-disk contacts are investigated in air and helium during load-unload as a function of the pitch static angle and the roll static angle between the slider and the disk. The acoustic emission signal and the change in rotational speed of the spindle were used to characterize head-disk contacts. It was observed that the permissible regions, consisting

of “safe” pitch static angle and “safe” roll static angle during load-unload, increases as the percentage of helium inside the chamber increases. The permissible regions have been integrated and estimated using image processing technique showing an improvement in helium (80%) compared to in air (65%). This finding is new and it shows an advantage of using helium instead of air to improve the robustness of the head-disk interface and to decrease head-disk contacts during load-unload. Our experimental data also showed that the average change of the rotational speed of the spindle is decreased of 0.05 rpm in helium compared to in air when head-disk contacts are absent. The result is consistent with previous reports [70], [148], [156] of diminished turbulent effects in helium than in air due to the lower density and the laminar flow characteristics of helium compared to air.

The SEM images of the sliders showed decreased carbon overcoat wear on the slider surfaces in helium compared to in air after 10,000 load-unload cycles, thus improving the head-disk interface in helium than in air. In the SEM images wear and scratches were absent near the center regions of the slider indicating that the function of the read and write elements were not affected during load-unload. Wear and scratches were observed near the trailing edge and the inner edge of the slider. Carbon overcoat wear of the slider surfaces is due to head-disk contacts during load-unload. However, the apparent ”scratches” seen at the recessed areas of the slider surfaces could also be lubricant traces transferred from the disks to the slider surfaces during head-disk contacts. Our surface analysis images confirmed the presence of lubricant redistribution on the disk surfaces after testing (Fig. 12 and 13). More lubricant redistribution was observed in air than in helium. Lubricant redistribution in air was observed at the roll static angles of -1.9 degrees, -1.4 degrees and

-0.9 degrees due to head-disk contacts. Lubricant redistribution at the inner edge of the slider is clearer than at the outer edge of the slider that agrees with the locations of worn areas and scratches on slider surfaces captured using SEM. Interestingly, in helium, lubricant moguls were absent at the roll static angles of -1.9 degrees and -1.4 degrees. Instead, lubricant moguls were observed at low roll static angles of 0 degrees and -0.9 degrees. We hypothesize that the results are due to the interaction between the slider and the lubricant layer when the slider was stayed on the "dwell track" for 200ms at each cycle. Helium has a much smaller density than air, thus it develops a lower pressure and a lower air bearing force on the slider. The simulation results confirmed that the flying height of the slider is smaller in helium compared to in air (Table 2). In addition, the pressure distribution applied to the lubricant surface is also smaller in helium than in air and the lubricant transfer critical condition may also change in air and in helium. The factors may cause the lubricant moguls to be formed and picked up by the slider in helium. Further investigations beyond the scope of this paper would be required to understand the mechanisms responsible for lubricant transfer and the formation of lubricant moguls in air and in helium during load-unload.

Table 4.2 Simulation results of the flying characteristics of the slider at the outer diameter of the disk

	Radius (mm)	**Skew angle (degree)**	**Minimum flying height (nm)**	**Pitch angle (µrad)**	**Roll angle (µrad)**
Air	45.70	16.80	9.60	83.43	-6.29
Helium	45.70	16.80	6.68	85.70	-19.60

However, it is important to note that the significant difference is observed with the slider mentioned in this paper. In practice, a slider can be designed to fly differently in air and in helium therefore the flying characteristics of the slider can be different

during the load-unload process and it is not obvious that this statement is still true for different designs of the sliders or at different operating conditions.

4.5 Summary

Our experimental results show that:

1) The roll static angle has a larger effect on head-disk contacts during load-unload than the pitch static angle.
2) The regions of "safe" pitch and roll static angles are larger for helium than for air.
3) Fewer head-disk contacts occurred in helium than in air for the same pitch static angle and the same roll static angle.
4) SEM and OSA images confirm that fewer head-disk contacts occur in helium than in air.
5) Slider frequency of 145 kHz was excited as a consequence of the head-disk contacts that corresponds to the first pitch mode of the slider.

Chapter 4, in part is a reprint of the material as it appears in "Effect of Air and Helium on the Head-Disk Interface during Load-Unload," Tan Trinh, Michael Sullivan, Sujit Kiperkar, and Frank E. Talke, *Tribology Letters 2018*. The dissertation author was the primary investigator and primary author of this paper.

Chapter 5

Investigation of Bias Voltage and Relative Humidity on Wear and Nano-Corrosion of the Head-Disk Interface

5.1 Introduction

In current hard disk drives, the spacing between the recording head and the recording disk is less than one nanometer to achieve an areal density of 1Tb/in^2 [81]. At such a small spacing, contacts between the head and the disk are likely to occur, causing wear of the interface and possibly failure of the drive [158]. Peng et al. [159] investigated wear of the head-disk interface as a function of the slider pitch static angle. They observed that at a high pitch angle, the slider preload was not fully supported by the air bearing, causing direct contact between the trailing edge of the slider and the disk surface. They suggested that two-body abrasive wear and adhesive wear were involved to explain the progress of wear at the head-disk interface. Thermal-flying height control (TFC) sliders have recently been used in wear testing performed by Wang et al. [160], Chen et al. [161], and Matthes et al. [162]. In their studies, the spacing between the slider and the disk was controlled by changing the heater power applied to the slider. Applying a heater power

larger than the heater power that causes first contacts, one can study the progression of wear between the thermal protrusion and the disk surface. The heater power applied above the heater power causing initial contacts is generally denoted as “over-push” heater power [100], [161]. In [161], the over-push technique was used to study wear at the read/write transducer area of the slider surface as a function of lubricant type and slider design. Li et al. [163] investigated wear of the head-disk interface by activating the heater power to maintain sub-nanometer clearance. Lubricant depletion was observed to occur at the disk surface. However, wear was absent on the carbon overcoat of the slider surface and the disk surface due to absence of head-disk contacts. To study wear of the head-disk interface, Li et al. simulated adhesion and contact forces at the head-disk interface using the compressible Reynolds equation with a probability model of surface roughness [164]. Their study showed that the contact force increases significantly if the minimum flying height decreases or if the surface roughness increases.

Recently, Knigge et al. [165] showed that application of a bias voltage between the slider and the disk affects the tribological properties of the head-disk interface. Rajauria et al. [166] and Matthes et al. [162] performed wear tests to investigate the effects of bias voltage, relative humidity and gas composition on wear of a thermal flying height control slider surface. Both studies were performed at relative humidity levels below 45%, although humidity levels above 50% are known to be very important for the failure of hard disk drives. Manousakis et al. [167] collected data from nine hyper-scale datacenters and showed that hard drive failure increased significantly at high relative humidity (80-90%) compared to low humidity levels. Corrosion of the controller board and the disk adapter due to high relative humidity were found to be the cause of increased failure rates of hard

disk drives. In the present study, burnishing tests were performed to study wear of the head-disk interface as a function of bias voltage over a range of relative humidity levels from 5% to 85%. Similar to the study performed by Matthes et al. [162], wear of the slider surface was determined by measuring the heater power needed for the onset of head-disk contacts, the so-called "power-to-contact (PtC)". Atomic force microscopy (AFM) was used to analyze wear and contamination of the slider after burnishing tests.

5.2 Experimental Setup and Experimental Procedures

5.2.1 Experimental Setup

A commercially available load/unload tester VS-90plus (VENA, USA) was used after electrically isolating the spindle and the actuator arm from each other and from the base plate. An acoustic emission (AE) sensor glued to the actuator arm was used to detect contacts between slider and disk. Sliders with individual heater elements for both the reader (RH) and the writer (WH) were used to control the flying height of the slider. Applying power to the heater elements of the reader and writer results in the formation of a thermal protrusion on the slider surface, decreasing the spacing between the slider and the disk [130]. The critical heater power that causes first contacts between the thermal protrusion and the disk surface is generally called "power-to-contact" (PtC). The change of the "power-to-contact" value before and after wear experiment can be used to characterize wear of the head-disk interface. A source-meter, Keithley 2400B (Keithley, USA), was used to apply a DC bias voltage to the disk with the slider body being grounded. A

commercially available data acquisition system (MCC, USA) and MATLAB [168] were used to control the heater power and bias voltage and to acquire data from the acoustic emission sensor. A schematic of the experimental setup is shown in Fig. 5.1.

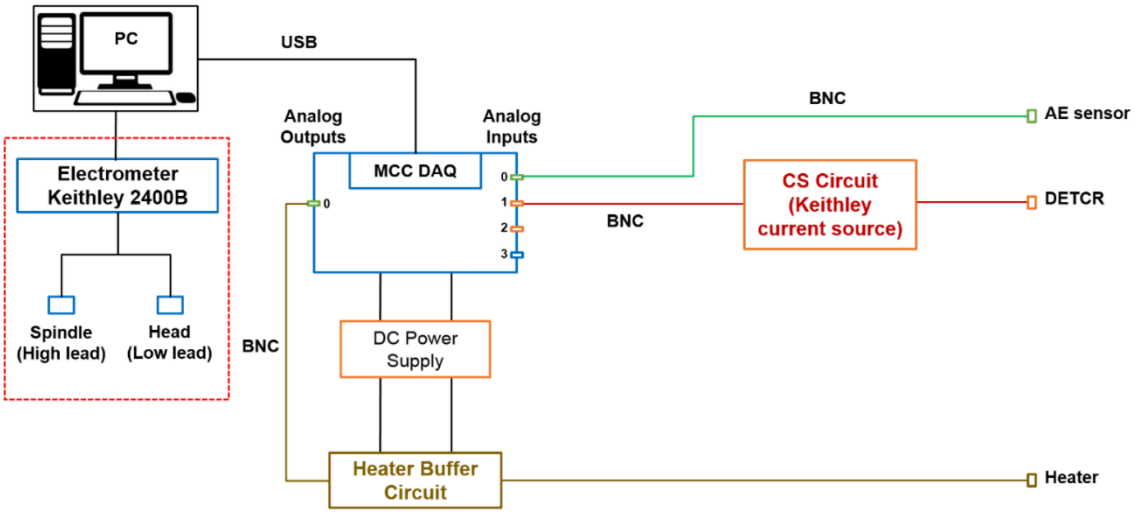

Figure 5.1 Schematic of the experimental setup. Head-disk contacts were measured using acoustic emission sensor. A source meter was used to apply a bias voltage to the disk.

The experimental tester was placed inside a sealed environmental chamber. The temperature and relative humidity inside the chamber were controlled using a commercially available controller (VENA, USA). During the test, the temperature inside the environmental chamber was maintained to be approximately 27°C (±1°C) and the relative humidity level was adjusted from 5% to 45% and 85% (±2%). Environmental conditions were maintained for 2 hours before testing started.

5.2.2 Head-Disk Interface Contact Potential Measurements

The contact potential difference V_{CP} across the head-disk interface is well known to be related to the work functions of the materials between the head and the disk. Introducing an applied bias voltage V_{bias} in combination with the contact potential

difference V_{CP} induces an electrostatic force between the head and the disk as shown in Fig. 5.3a. The electrostatic force across the head-disk interface is given by:

$$F_{elec} = (V_{CP} + V_{bias})^2 \int_{Area} \frac{\varepsilon_0 \varepsilon_r}{2h} dA, \tag{5.1}$$

, where h is the spacing between the slider and the disk, ε_0 and ϵ_r are the vacuum permittivity and relative permittivity of the air, respectively, and dA is an infinitesimal element of area between the slider surface and the disk surface. Changing the applied bias voltage V_{bias} results in a change of the electrostatic force across the head-disk interface. As a consequence, the flying height of the slider and the power-to-contact change as a function of the applied bias voltage. Fig. 5.2 (a) shows power-to-contact as a function of the applied bias voltage. We observe that power-to-contact increases initially with bias voltage, reaches a maximum, and decreases thereafter. The contact potential was determined by performing curve fitting of power-to-contact measurements versus applied bias voltage and determining the highest flying height of the slider. The highest flying height of the slider occurs if the electrostatic force across the head-disk interface is a minimum, i.e., if the applied bias voltage and the contact potential difference cancel each other. Measurements of the contact potential for six different head and media combinations are shown in Figure 2b, indicating a mean value of contact potential difference of approximately 0.35V with a standard deviation of 0.07V. The disk was negatively biased with respect to the head. Knigge et al. [144] measured the contact potential difference of the head-disk interface using laser Doppler vibrometry and a lock-in amplifier. Their measurements showed that the contact potential difference is approximately 0.5V. Trinh et al. [169] used Kelvin probe

measurements to determine the contact potential of the head-disk interface. Their measurements showed that the contact potential is approximately 0.4V. Tani et al. [145] and Matthes et al. [162] found that the contact potential difference is approximately 0.11V and 0.13V, respectively. They observed that the electrical potential of the disk is smaller than the electrical potential of the head surface. Tani et al. [145] hypothesized that a negative electrical potential of the disk is caused by the high electronegativity of the Fluorine in the lubricant layer. Clearly, our measurements fall in the same range with their measurements.

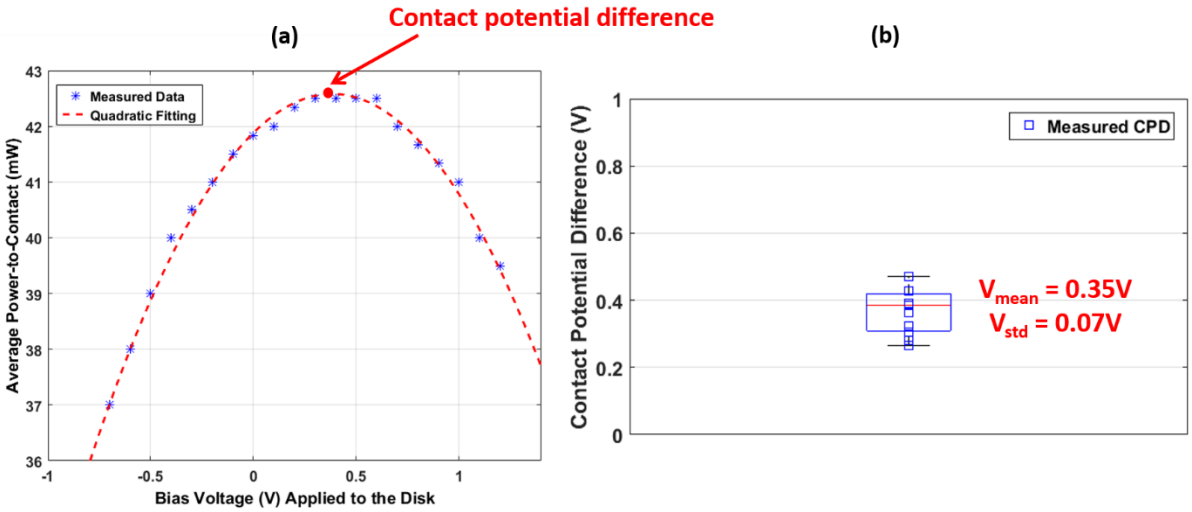

Figure 5.2 (a) Power-to-Contact (PtC) as a function of applied bias voltages (b) Statistical measurements of the contact potential difference

5.2.3 Burnishing Test Procedure

"Burnishing tests" were performed to study the effect of bias voltage and relative humidity on wear of the head-disk interface. In our experiments, the average contact potential difference of the head-disk interface V^* was measured to be approximately 0.35V. For our burnishing tests, different bias voltages of - 0.65V, 0V, 0.35V, and 1.35V were applied, respectively, to the disk, with the slider body being grounded. The relative

humidity inside the chamber was maintained at 5%, 45%, and 85%, respectively, for two hours before the test started. A typical burnishing test proceeded as follows. First, the disk rotational speed was increased to 5,400 rpm from rest and the slider was moved from the load-unload ramp to the outer diameter location on the disk. Thereafter, the heater power was increased from 0mW in steps of 0.5mW until the onset of head-disk contacts occurred. Contacts between the head and the disk were detected by measuring the standard deviation of the acoustic emission signals (Fig. 5.3a). A typical burnishing test consisted of 60 wear cycles. The duration of each wear cycle was 20 seconds. Before each wear cycle, the power-to-contact of the head-disk interface was measured. In each wear cycle, an additional heater power of 30mW was applied above the power-to-contact. After a wear cycle, the heater power was turned off and the cycle was repeated. It is important to note that the worn area on the disk surface is much larger than the worn area on the thermal protrusion on the slider surface. Thus, it is justifiable to assume that the wear depth on the disk surface is small compared to the wear depth on the slider surface and that the change of the power-to-contact (ΔPtC) value can be used to characterize the wear depth of the slider surface (Fig. 3b).

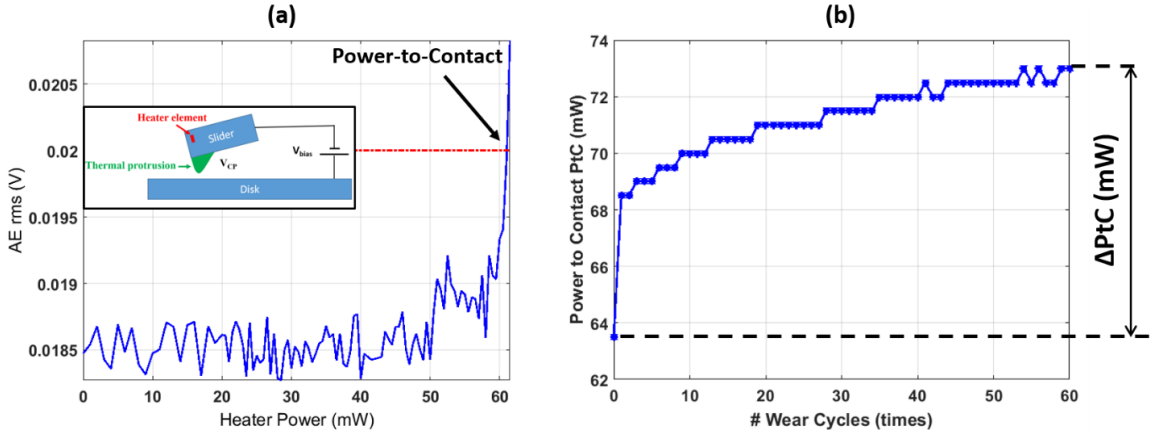

Figure 5.3 (a) Head-Disk contacts detection using acoustic emission (AE) sensor (b) Power-to-contact measurements during burnishing test (1 wear cycle is 20 seconds)

5.3 Experimental Results

Fig. 5.3b shows a typical power-to-contact measurement result as a function of wear cycles. We observe that the power-to-contact curve has a steep slope at the beginning of the test before reaching a steady state value with a much smaller slope. The initially strong change of the power-to-contact curve is related to the wear-in process of the head-disk interface. During the wear-in process, high peaks of individual asperities on the slider and disk surfaces are removed due to contacts between the thermal protrusion area and the disk surface. After a few cycles, wear of the thermal protrusion decreases, resulting in a decreased slope of the power-to-contact curve. In the present study, the change of the power-to-contact (ΔPtC) value was measured to study wear of the slider surface.

Figures 5.4a and 5.4b show the change of the power-to-contact, ΔPtC, as a function of applied bias voltage between the head and the disk at 45% and 85% relative humidity, respectively. We observe that at 45% relative humidity, the change of the power-to-contact value is larger for a bias voltage of -0.65V than for bias voltages of 0V, 0.35V and 1.35V, respectively, i.e., more wear occurs on the slider surface at negative bias voltage than at positive bias voltage. A similar result was observed also at 85% relative humidity level. Knigge et al. [165] observed the same result, i.e., that negative biasing of the slider with respect to the disk, or positive biasing of the disk with respect to the slider, reduces wear on the slider surface compared to the case when a negative bias voltage is applied to the disk. Rajauria et al. [166], [170] and Matthes et al. [162]s performed wear testing at 40% relative humidity and showed reduced wear for negative bias voltage of the slider with

respect to the disk. Our results agree well with the results presented by Knigge et al. [165], Rajauria et al. [166] and Matthes et al. [162].

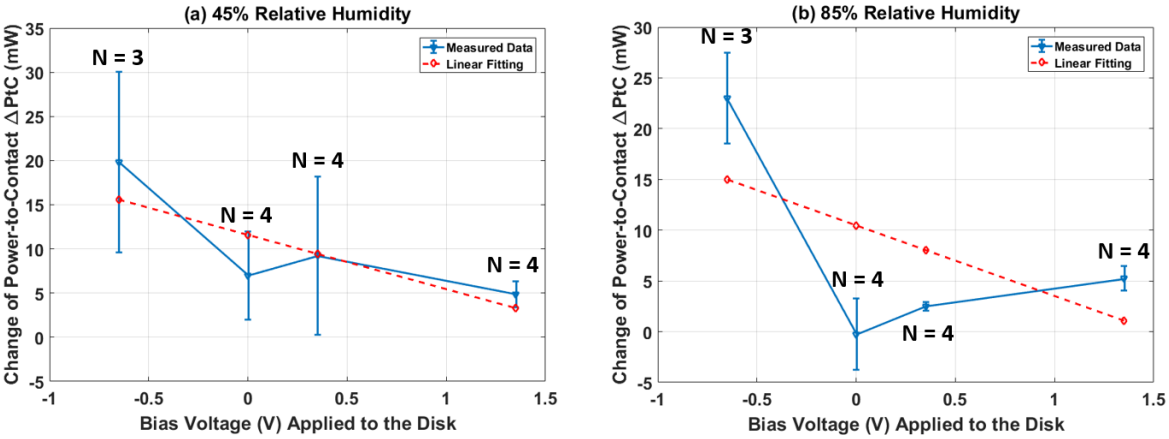

Figure 5.4 Change of the power-to-contact (ΔPtC) as a function of the applied bias voltages at (a) 45% and (b) 85% relative humidity. Number of tested heads N are shown in the figures.

Fig. 5.5 shows the change of the power-to-contact value as a function of the applied voltage between the slider and the disk at 5% relative humidity. We observe that the power-to-contact change is of similar magnitude at 5% relative humidity as at 45% and 85% relative humidity at -0.65V bias voltage. However, at positive bias voltages of 0.35V and 1.35V, the power-to-contact changes are larger at 5% relative humidity compared to the cases at 45% and 85% relative humidity levels. Interestingly, the slope of the power-to-contact versus bias voltage is reversed compared to that of 45% and 85% relative humidity. Clearly, relative humidity plays an important role in wear of the head-disk interface in combination with bias voltage.

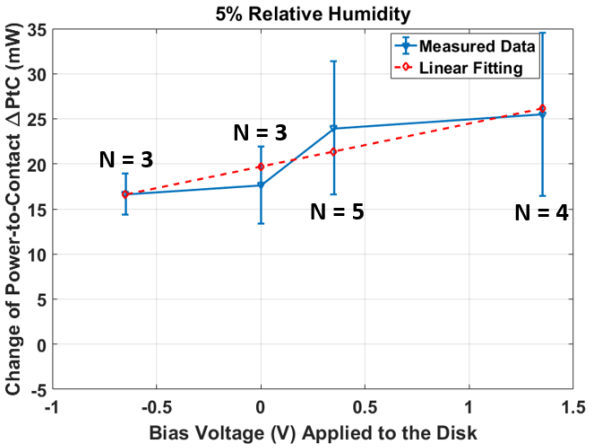

Figure 5.5 Change of the power-to-contact as a function of the applied bias voltage at 5% relative humidity. Number of tested heads N are shown in the figures.

5.4 Atomic Force Microscopy and Electrostatic Force Microscopy Measurements

After completing the burnishing tests, the read and write areas of the slider surface were scanned using Atomic Force Microscopy (Dimension 3100, Bruker, USA) to investigate wear on the slider surface. A typical image of the read and write area and the slider topography of a new (untested) head are shown in Fig. 5.6. The write element consists of the main write pole and the return write poles (on the left side of the image). The read element is sandwiched between the read shields located near the center of the image. The right side of the image shows the slider substrate made of AlTiC (Al_2O_3-TiC). The return poles and the read shields are elevated from the slider surface by approximately 2nm. A thermal resistance sensor, denotes as DETCR in Fig. 5.6a, is located between the

return write poles. This sensor can be used to detect contacts between the thermal protrusion and the disk surface.

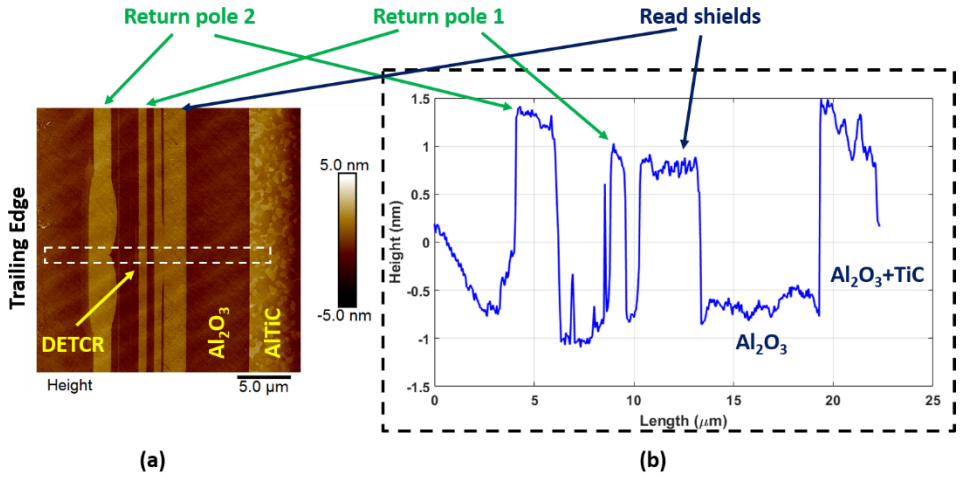

Figure 5.6 (a) Atomic force microscopy images of the read and write area of an untested head. (b) Topography of the centerline of the read and write area.

Figures 5.7a, 5.7b, and 5.7c show images of the slider surfaces at 45% relative humidity and bias voltages of -0.65V, 0.35V and 1.35V, respectively. Wear of the slider surface in the form of an elongated ellipse can be seen in Fig. 5.7a and 5.7b near the return write poles area. During the burnishing tests, the heater of the writer was activated, and the writer elements were brought into contacts with the disk surface, resulting in wear in the write pole area. Contacts between the thermal protrusion and the disk have caused the scratch marks shown in Fig. 5.7, inclined at an angle of approximately 15 degrees. This angle corresponds to the skew angle of the test. A decrease in wear was observed in the write pole area at 45% relative humidity if the bias voltage was changed from negative values to positive values. The topography of the slider surfaces for the cases show in Fig. 5.7a, 5.7b, 5.7c is shown in Fig. 7d, confirming that wear decreased in the main write pole area if a positive bias voltage was applied compared to the case that a negative bias voltage was applied. Clearly, the AFM results agree well with the change of power-to-contact

measurements (Fig. 5.4a). In addition, particle buildup was observed on the slider surfaces after testing.

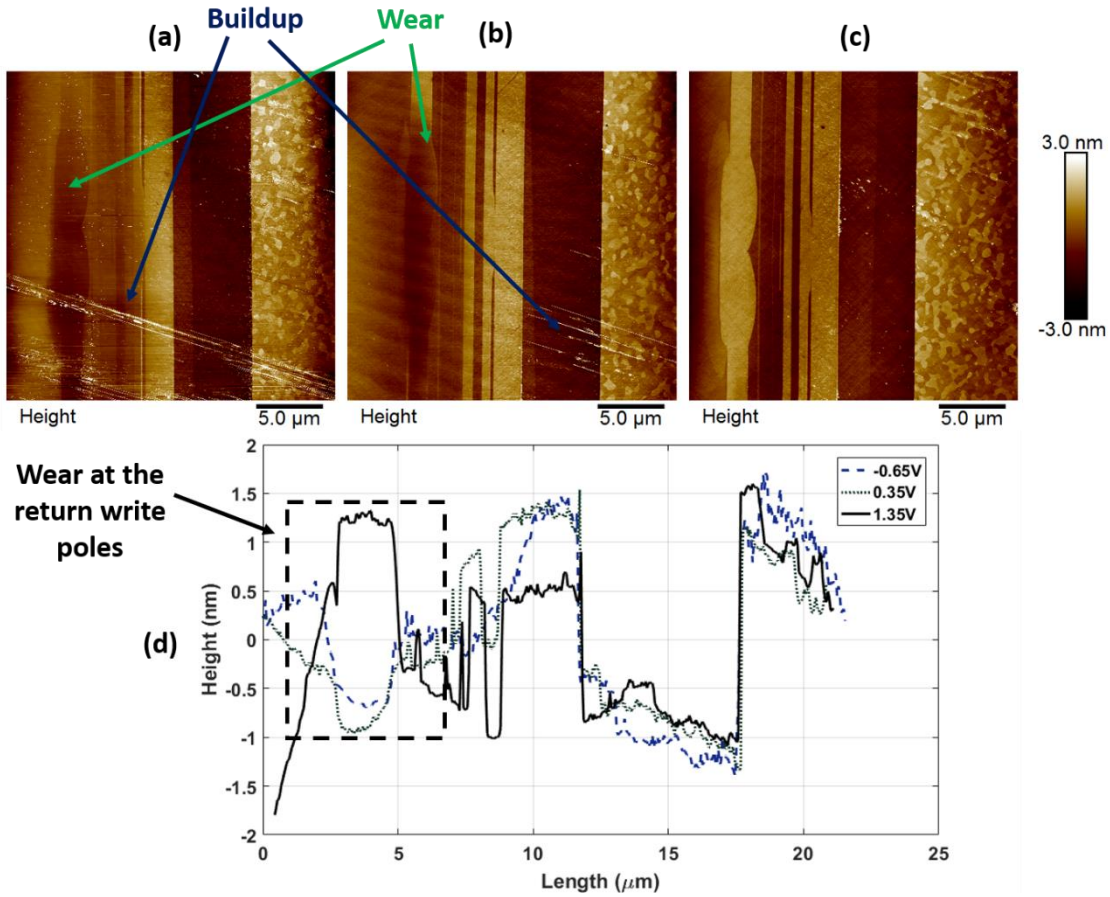

Figure 5.7 Atomic force microscopy images of the slider surface after burnish testing at 45% relative humidity (a) -0.65V (b) 0.35V (c) 1.35V and (d) Topography of the read and write areas of sliders shown in Fig. 5.7a, 5.7b, and 5.7c

Atomic force microscopy images of the slider surfaces at 85% relative humidity levels at different bias voltages are shown in Fig. 5.8. We observe that a decrease of wear occurred at 0.35V and 1.35V compared to at -0.65V. This result agrees well with the previous power-to-contact measurements (Fig. 5.4b). Particle buildup is also present on the slider surfaces. In the presence of a positive bias voltage of 1.35V and 0.35V at 85% relative humidity, we observe multiple "pin holes" on the slider surface, marked by a dashed line in Fig. 5.8b and 5.8c. These holes were seen only at the write pole area of the

slider surface, where the thermal protrusion was in contact with the disk surface. A line scan of the holes shows a depth of approximately 70-100nm and a width of approximately one micrometer (Fig. 5.8d). The holes are typical for pitting corrosion in the presence of positive bias voltage and high relative humidity of 85%. Fig. 5.9 shows AFM images of the slider surfaces after testing at 5% relative humidity. Wear at -0.65V bias voltage is also more severe than wear at 0.35V and 1.35V bias voltages. This result does not agree with the power-to-contact measurements (Fig. 5.5), where the change of the power- to-contact at -0.65V is smaller than at 0.35V and 1.35V. Particle pickup observed at 5% relative humidity, however, is much less pronounced compared to 45% and 85% relative humidity.

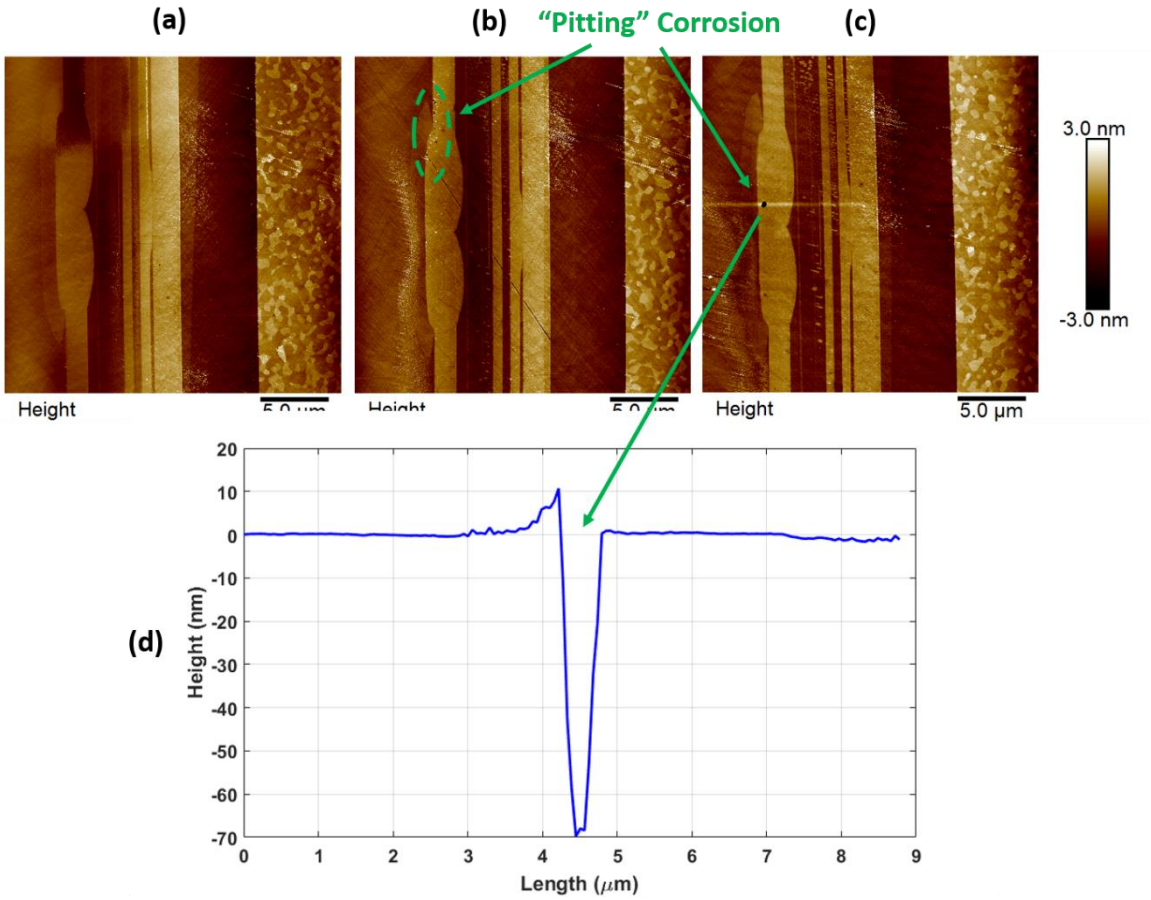

Figure 5.8 Atomic force microscopy images of the slider surface at 85% relative humidity (a) -0.65V (b) 0.35V (c) 1.35V (d) Topography of a typical pitting corrosion

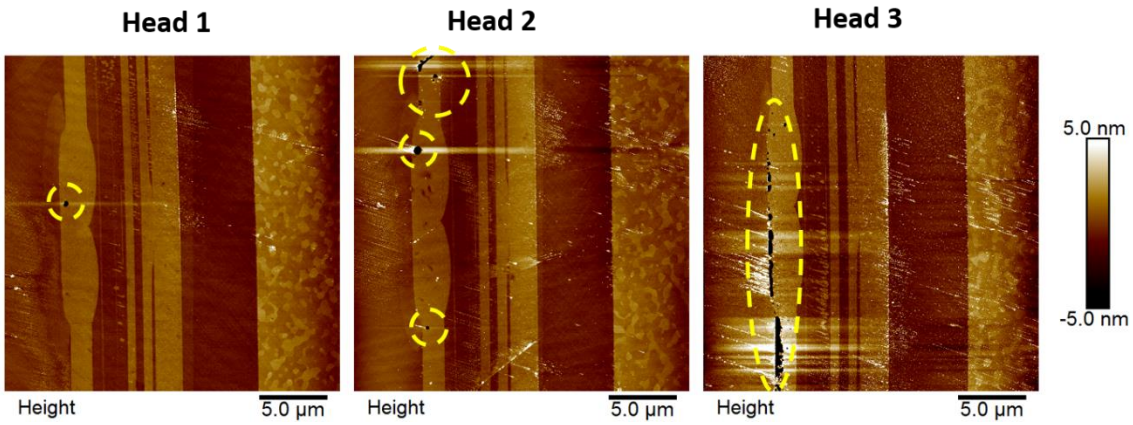

Figure 5.9 Atomic force microscopy images of three slider surfaces at 1.35V and 85% relative humidity

To investigate the influence of bias voltage polarity on pit formation at 85% RH, a burnishing test was conducted with -1.35V disk bias. Although wear was observed at the write pole area of the head surface as previously observed with 1.35V bias (i.e., within the thermal protrusion area), Fig. 5.10 shows that the negative disk bias resulted in corrosion of the reader shield nearest the write return pole and in pitting/corrosion at the interface between the write element and the Al_2O_3 dielectric layer.

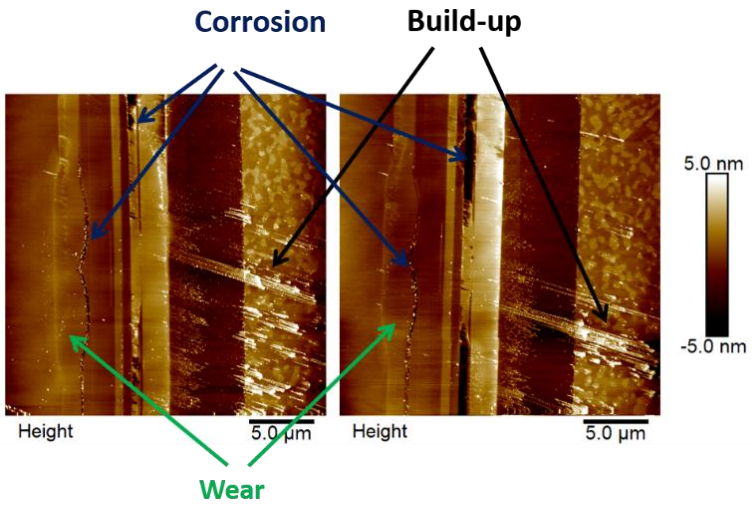

Figure 5.10 Atomic force microscopy images of two slider surfaces at -1.35V and 85% relative humidity

Fig. 11 shows AFM images of slider surfaces after testing at 5% relative humidity. We observe that the size of the wear scar at a bias voltage of -0.65V is larger than at a bias voltage of 0.35V or 1.35V, respectively. This result is surprising, since it does not agree with the power-to-contact measurements (Fig. 5), where the change of the power-to-contact at -0.65V is smaller than at 0.35V and 1.35V.

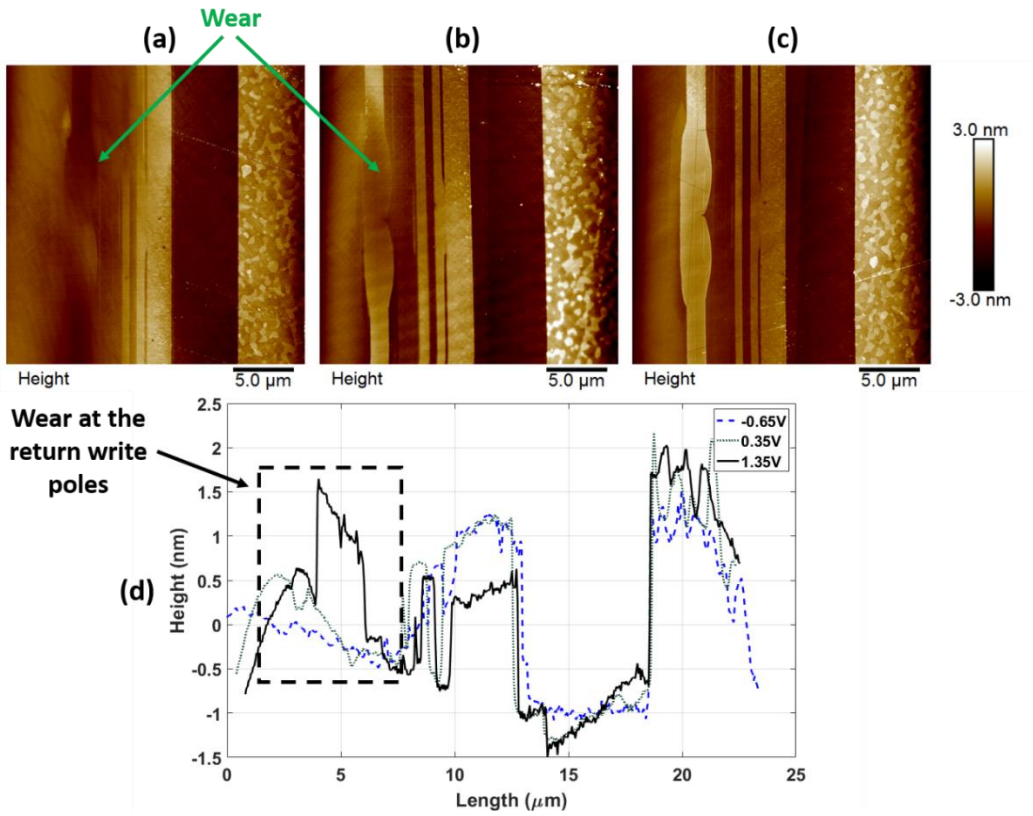

Figure 5.11 Atomic force microscopy images of slider surfaces at 5% relative humidity (a) -0.65V (b) 0.35V (c) 1.35V

5.5 Discussion

The change in power-to-contact trend presented in Sections 3 and 4 agrees with earlier studies [162], [165], [166]. In particular, we observe that at low relative humidity a smaller touchdown-power change ΔPtC occurred at a fixed number of wear cycles at negative bias voltage than at positive bias voltage (Fig.5.5). These results were found to be reversed at high relative humidity (Fig. 5.4), where the change in touchdown power ΔPtC was found to decrease for a fixed number of wear cycles with increasing bias voltage. Thus, to minimize the touchdown power change ΔPtC in a hard disk drive, it is desirable to adjust the bias voltage depending on the relative humidity present, i.e., negative bias should be applied at low relative humidity and positive bias should be applied at high relative humidity. With present sensor technology, this dynamic adjustment of the bias voltage should be feasible.

The benefit of positive disk bias for reducing slider wear at high humidity is limited, however, by pinhole formation in the writer shield regions, as shown in Figs. 5.8 and 5.9. From our studies we have observed that pinholes are likely to form if positive bias is applied at high relative humidity (RH between 45 and 85 % RH). Pinhole formation on the slider surface could be caused by humidity-enhanced corrosion of the writer pole at pre-existing defect sites in the protective overcoat. Local action Faradaic currents on the write pole surface in high humidity environments will enhance electrochemical corrosion at such defects due to currents if the pole tip material is an anodic area and the larger area of surrounding protective overcoat is a cathodic area [171]. Pinhole formation could also result from electrostatic discharge damage at the head-disk interface caused by the high

bias voltage. Wallash [172] studied the electrical properties of diamond-like carbon overcoats and concluded that a potential difference of less than 1V between the head and the disk could lead to a breakdown of the protective carbon overcoat. This breakdown is likely to accelerate at high relative humidity conditions, since water might ionize in high electric fields. In this case, the resistance between head and disk surface decreases, leading to an increase of the electrical current that causes breakdown. Wallash [172] observed crater-like damage of approximately 25nm depth and 1 micrometer diameter caused by electrical breakdown. The crater dimension in his paper is in good agreement with the pit formation in our study.

One last comment with respect to the causes of corrosion applies to the magnetic head design. A change of the bias voltage polarity may cause a stray current to occur, depending on the interconnection impedances of the head. Controlling the impedances of the connections between the read shields and the write poles to the slider substrate could alleviate stray current corrosion on the slider surface. This effect can potentially be used to reduce corrosion of the slider.

5.6 Summary

The following conclusions can be drawn from the study of the effect of bias voltage and environmental relative humidity on wear and pit formations of the head-disk interface:

1. At high relative humidity (45% - 85%), power-to-contact change ΔPtC for a fixed number of wear cycles is smaller at positive disk bias voltage than at negative disk bias voltage.

2. At low relative humidity, the power-to-contact change ΔPtC for a fixed number of wear cycles is larger at positive disk bias voltage than at negative disk bias voltage.
3. Pit formation was observed at high relative humidity at positive bias voltage. Different mechanisms, including the presence of pre-existing pits, electrical breakdown, or stray current corrosion, seem to be the cause for the formation of pits.
4. To minimize the power-to-contact change ΔPtC in a hard disk drive as a function of wear cycles, dynamic adjustment of the bias voltage based on the actually existing relative humidity in the disk drive is needed.

Chapter 5, in part, is currently being prepared for submission for publication of the material. "Investigation of the Effect of Bias Voltages and Relative Humidity on Wear and Buildup at the Head-Disk Interface," Tan Trinh, Christoph Schade, Michael Johnson, and Frank E. Talke, submitted to *IEEE Transactions on Magnetics*, 2019. The dissertation author was the primary investigator and primary author of this paper.

Chapter 6

Effect of Radius, Head-Disk Clearance, and Media Properties on Optical Power in Heat-Assisted Magnetic Recording

In heat-assisted magnetic recording (HAMR), minimization of optical laser power is important for the reliability of the head-disk interface. In this paper, a prototype heat-assisted magnetic recording system is used to investigate the relationship between the needed optical laser power and disk drive design parameters. In particular, the change of optical laser power, which is a function of the laser current, is investigated for different disk radii and write head flying heights while keeping the write width of the recorded signal constant. In addition, the dependence of laser power during writing is studied as a function of the thickness and material properties of a very thin “capping layer” on the top of the recording magnetic layer. The results show that laser power and media design parameters play a crucial role in heat-assisted magnetic recording devices.

6.1 Introduction

Heat-assisted magnetic recording (HAMR) is a new technology that has the potential to improve the areal density of hard disk drives (HDDs) to 10Tbit/in^2 [51], [52], [81], [173]. To achieve areal densities as high as 10Tbit/in^2, the magnetic grain volume on the recording medium must be decreased to maintain an adequate signal-to-noise ratio (SNR). Decreasing the magnetic grain volume leads to instability of the recorded data on the media surface due to thermal fluctuations, described as the "superparamagnetic" phenomenon [51]. To overcome this instability, new materials of high anisotropy and high coercivity have been investigated, such as, FePt, CoPt, CoPd, $SmCo_5$, and $Nd_2Fe_{14}B$ [28], [39], [51]. However, for these materials, the magnetic field from a conventional write transducer is not strong enough to write data on the disk surface. In heat assisted magnetic recording a nanometer-sized area on the disk surface is heated to near or beyond the Curie temperature (T_C) of approximately 450°C by using near-field coupling effects [52]. At the Curie temperature, the coercivity of the magnetic layer is reduced to zero, which then allows to write data with the magnetic field produced by state-of-the art magnetic writer. To deliver power from a laser diode mounted on the top of the slider, a plasmonic optical device, "near-field transducer" (NFT), located on the slider air-bearing surface is used. Controlling the optical laser power in HAMR is critical for the following reasons: low optical power produces insufficient media temperature thereby a poor writing performance on the disk surface. On the other hand, if the optical power is too high, very high temperatures of both the head and disk surface affect reliability of the NFT device and head-disk interface.

In this investigation, a prototype HAMR system is used to investigate the relationship between laser optical power and disk drive design parameters. In particular, the change of laser power is investigated for different disk radii and write head flying heights while keeping the write width of the recorded signal constant. In addition, the dependence of laser power during writing is studied as a function of the thickness and material properties of a very thin "capping layer" on top of the recording layer. The results show that laser power and media design parameters play a crucial role in the performance of heat-assisted magnetic recording devices.

6.2 Experimental Setup and Procedures

A commercially available spin stand tester (Guzik Enterprise, USA) was used for testing as shown in Figure 1a. A HAMR recording head was mounted on the actuator arm to read and write data on the HAMR disk. The reading and writing process was controlled by a read and write analyzer (Guzik Technical Enterprises, USA). During testing, the rotational speed of the 3.5" (95 mm) HAMR disk was kept constant at 7200 rpm. The HAMR head was mounted on the actuator arm, allowing control of the head operating radius and skew angle. In this study, the operating radius was varied from the innner diameter (ID) to the outer (OD) diameter on the disk surface, corresponding to a skew angle range from -12.5 º to 15.5 º degrees (Figure 6.1 (b)).

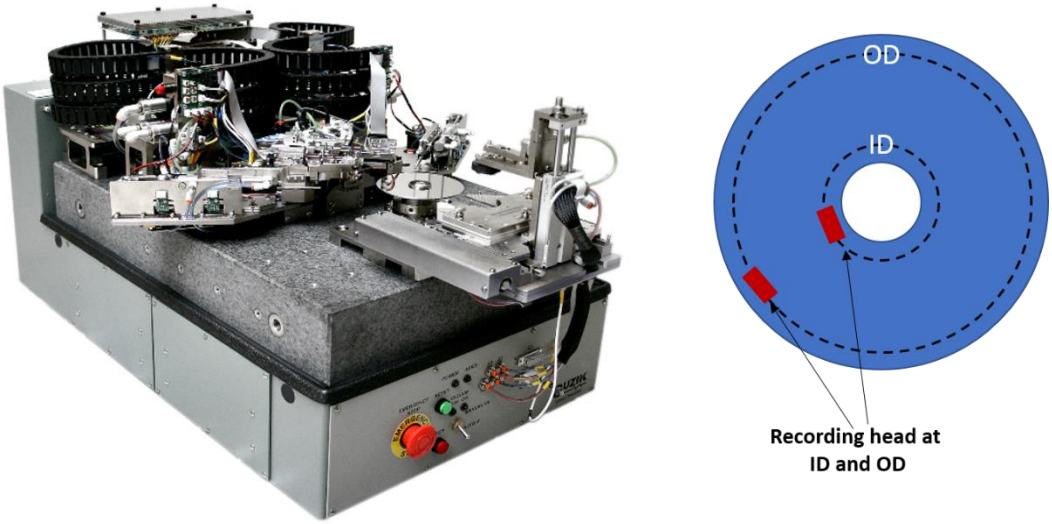

Figure 6.1 Guzik tester with a read and write analyzer

Prior to testing, the recording head was loaded on the disk surface. The minimum flying height between the recording head and the recording media (head-disk clearance) was controlled by applying power to a small heater element embedded inside the recording head [130]–[132]. Increasing the heater power induces a thermal protrusion that decreases the head-disk clearance. The head-disk spacing is calibrated based on touchdown detection using an acoustic emission (AE) sensor that is mounted on the actuator arm. The flying height is obtained by measuring the read-back signal amplitude and applying the Wallace spacing equation [75]. A commercially available software package (WITE32 [174]) was used to control the experimental variables, including rotational speed, the actuator arm position, the read/write analyzer, the laser power, and the acoustic emission signal. The tester is enclosed inside an environmental chamber, in which temperature and relative humidity were controlled. Testing was performed in air at room temperature of 27º C, relative humidity of less than 5%, and at 0.8 atmospheric pressure.

6.2.1 Calibration of Head-Disk Flying Height

One of the challenges in HAMR technology is related to measurement and control of write clearance between the slider and the disk surface [112]. During the writing process, power from the laser diode is delivered through an optical waveguide inside the slider to the near-field transducer (NFT) on the bottom surface of the slider. The power from the laser diode causes an increase in the temperature of the NFT, causing the NFT to protrude towards the disk surface. This protrusion is generally called the NFT protrusion and denoted in this paper as "NFTPtr". In addition, an electrical current is applied to the write coil during the writing process, leading to a write pole induced protrusion. This protrusion is denoted as write pole thermal protrusion "WPTPtr". In addition to the write pole thermal and NFT protrusions, dissipated energy from the laser diode heats the slider body, causing a third protrusion, the so-called laser diode protrusion "LDPtr" [175].

In Figure 2, a schematic of the three protrusions occurring during writing is shown. We note that the LDPtr is broader than the other two protrusions. Furthermore, each protrusion has a different time scale of formation, with time constants ranging from microseconds to milliseconds [111], [176]. The protrusions change the write clearance of the slider during the write process. Since the near-field transducer protrusion is a highly localized protrusion, contact detection using acoustic emission (AE) or touchdown sensors (TDS) is inadequate [112], [177], [178].

During the read process, the laser diode, the write head, and the near field transducer are not energized, and none of the three write process related protrusions are present. To determine the head medium spacing during reading, a micro heater embedded

inside the slider was used. Energizing the heater element results in the formation of a thermal protrusion on the slider surface that moves the read and write elements towards the disk surface (Figure 6.2).

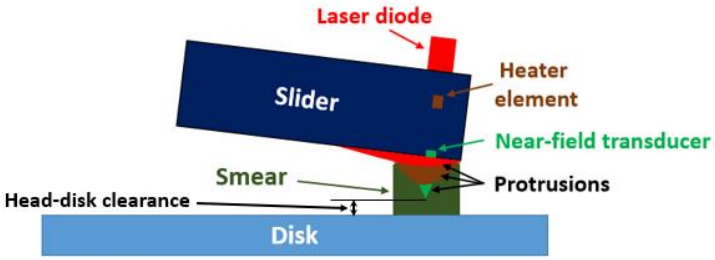

Figure 6.2 A schematic of HAMR head-disk interface

At the beginning of each experiment, the laser diode and the writer coil were both turned off and the head was loaded onto the disk. Thereafter, the heater power was increased in steps of 0.5mW until contact was detected between the thermal protrusion and the disk surface. The flying height of the slider was determined using Wallace spacing measurements (Equation 6.1).

$$E = f \exp(-2\pi d / \lambda) \tag{6.1}$$

In equation (6.1), E is the measured amplitude of the readback signal, d is the spacing between slider and disk surface, λ is the wavelength of the recorded signal, and f is a function of the slider and disk properties. The acoustic emission signal and the Wallace

spacing measurements are shown in Figure 3 for a typical slider used in our experiments. We observe that the AE signal remains low until contact occurs at approximately 135mW.

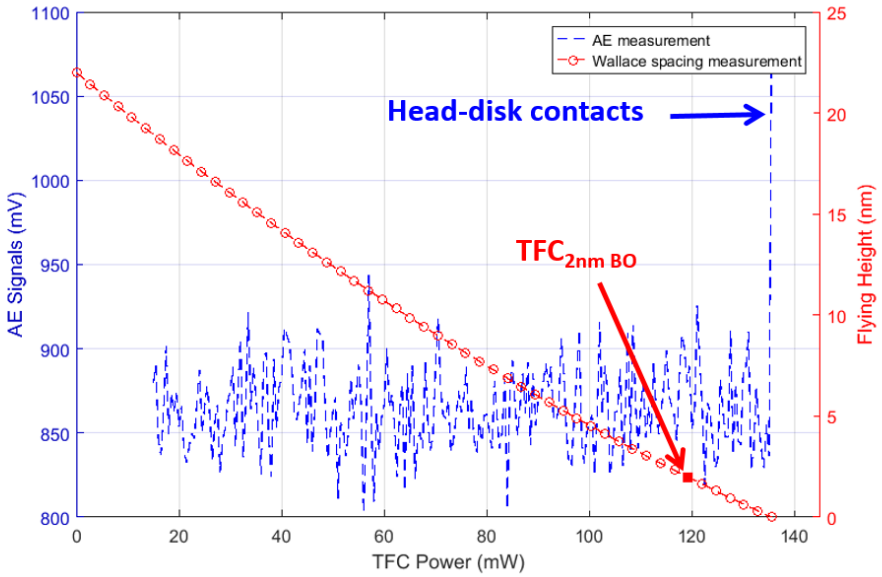

Figure 6.3 Head-disk clearance set up using acoustic emission sensor and Wallace spacing measurements

In Fig. 6.3, the notation $TFC_{2\ nm\ BO}$ corresponds to the heater power that causes a back off (BO) of 2 nm from the touchdown point during reading. This heater power does not account for the flying height changes due to the NFTPtr, the WPTPtr, or the LDPtr during writing. Because of these additional protrusions occurring during writing, the heater power must be adjusted to maintain a constant flying height of approximately 2 nm. This is shown in equation (6.2),

$$\text{Read\_TFC} = TFC_{2\ nm\ BO}$$

$$\text{Write\_TFC} = TFC_{2\ nm\ BO} - (\text{WPTPtr} + \text{NFTPtr} + \text{LDPtr}) \,.\, TFC_{efficiency} \qquad (6.2)$$

where Read_TFC and Write_TFC denote the heater power to maintain a flying height of 2nm during both reading and writing, respectively. $TFC_{efficiency}$ is assumed to be same for the three protrusions.

The write pole tip protrusion (WPTPtr) and the near-field transducer protrusion (NFTPtr) were determined using the so-called burst writing scheme (BWS), proposed by Xiong et. al. [112]. In this approach, the "read-back" signal amplitude is measured as a function of the heater power for short signal bursts and long signal sectors (Figure 6.4). For short bursts the WPTPtr and the NFTPtr are not yet developed, while for sector writing both protrusions have reached steady state. Thus, the difference between both read back signals in Figure 6.4 represents the sum of the heater power due to WPTPtr and the NFTPtr. As is shown in Figure 6.4, the difference between both read signals is approximately 30 mW.

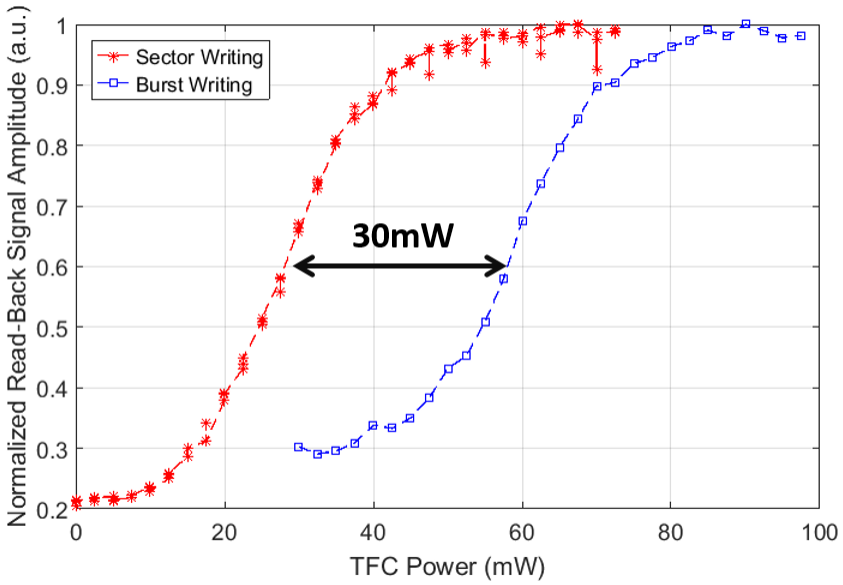

Figure 6.4 Burst writing scheme method. The difference between the blue and the red curve represents the near-field transducer protrusion and the write pole tip protrusion

6.2.2 Magnetic Write Width Measurements

The magnetic write width (MWW) is used as a measure of the width of the magnetic recording track. To achieve an areal density of 1Tbit/in^2, the MWW must be approximately

50 nm [179]. To determine the MWW, we have used the following procedure. We have first adjusted the head-disk flying height during writing to 2 nm by selecting the appropriate heater conditions. Thereafter, the laser diode and the write gate were turned on and data was written on the disk along a single track. After completing the writing of data, "track profile measurement" [180] was performed by measuring the read-back signal amplitude of the written signal as a function of the radial displacement of the head from the center of the track. Figure 6.5 (a) shows the normalized read-back amplitude versus cross track offset. We observe that the read-back signal amplitude decreases with the distance that the read element is displaced from the center of the track. If the read element is positioned at the center of the track, the read-back signal amplitude is at its maximum. The MWW is defined as the width of the cross-track profile at 50% of the peak amplitude. Figure 6.5 (b) shows the MWW as a function of the normalized laser power.

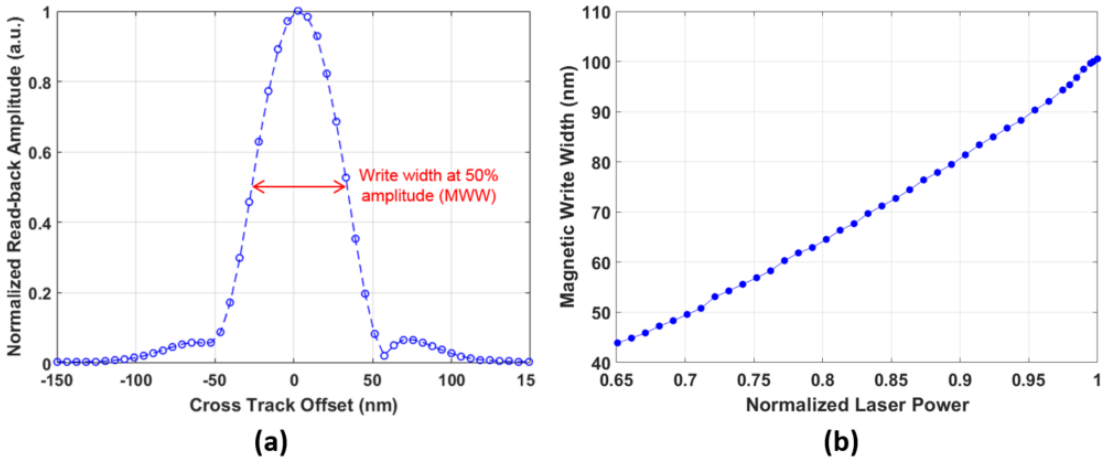

Figure 6.5 (a) Typical track profile measurement. The magnetic write width is determined by measuring the cross-track offset at 50% of the read-back signal amplitude (b) Magnetic write width vs. applied laser power

6.3 Experimental Results

6.3.1 Laser Current versus Operating Disk Radii

In Figure 6.6, the laser power required to achieve a track width of 60nm, 80 nm, and 100nm, respectively, is shown versus disk radius. For this experiment, the flying height of the slider during writing and reading was kept constant at 2 nm. We observe that the laser power increases for all write track widths as the disk radius is increased. In particular, the required laser power at the inner diameter (ID) is approximately 18% lower than the required laser power at the outer diameter (OD) of the disk surface.

Since the linear velocity between the slider and the disk increases as a function of the radius, we hypothesize that cooling effects on the disk surface increase with increasing radius. Thus, higher laser power, or, equivalently, a larger laser current, is needed to reach the Curie temperature at an outer radius location than at an inner radius location under the

same magnetic write track width. In addition, the skew angle difference between inner and outer diameter can influence the laser current needed fsssor achieving a desired track width.

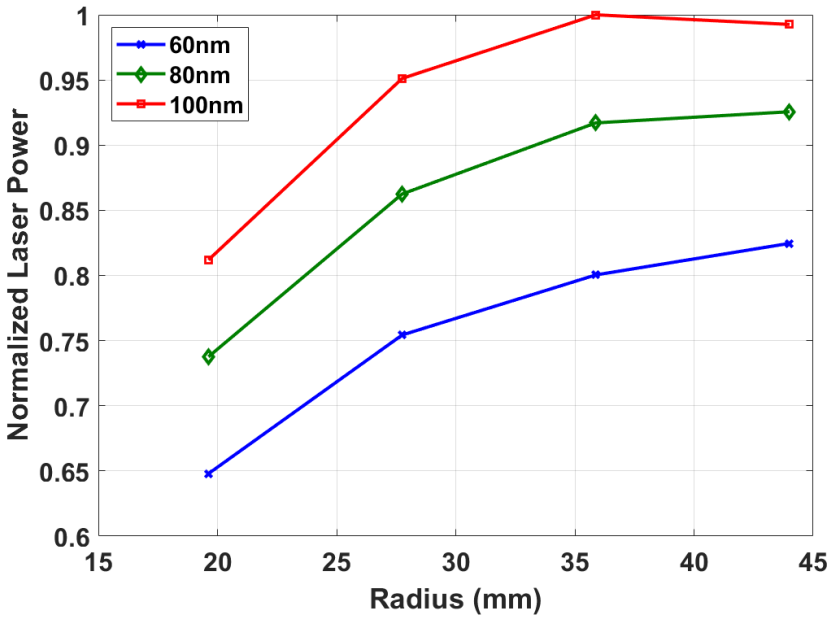

Figure 6.6 Laser current vs. operating radius (ID, MD, and OD) at 60nm, 80nm, and 100nm magnetic write width (MWW)

6.3.2 Laser Current versus Flying Height during Writing

To investigate the laser power as a function of write flying height, the head-disk spacing was adjusted in the range from 1 nm to 8 nm, in increments of 1 nm. The write current was kept constant and the laser power used was increased at each write flying height until a magnetic write track width of 60 nm was obtained on the disk surface. The head disk flying height during reading of the data was kept constant at 2 nm. Four measurements were performed at each head-disk spacing to reduce errors caused by the pressssssence of a thin “smear layer” that was likely formed on the slider surface [111], [112].

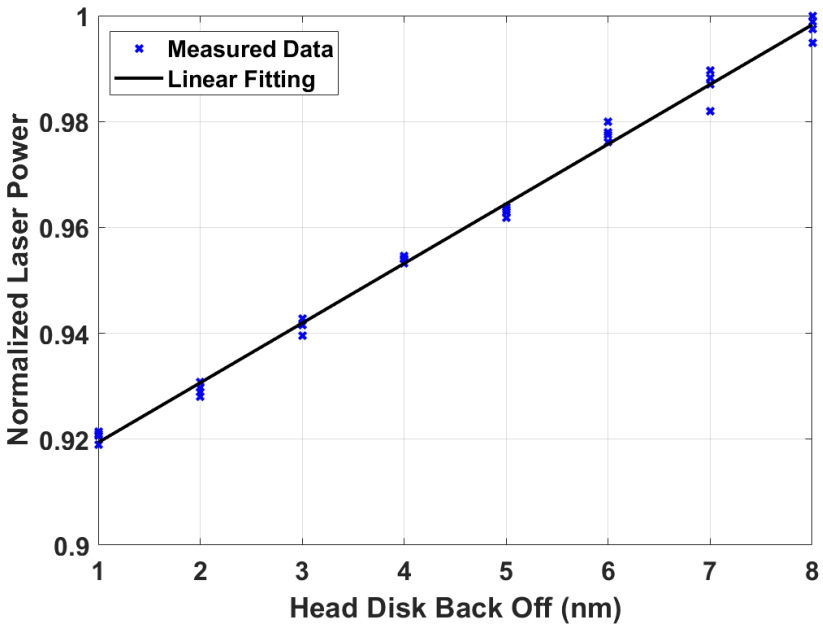

Figure 6.7 Laser current vs. head-disk spacing at 60nm MWW

Figure 6.7 shows the laser power to achieve a magnetic track width of 60 nm as a function of the head disk spacing during writing. We observe that a higher laser power of about 8% is required as the write spacing increases from 2 nm to 8 nm during writing of the data. It is apparent that the media heating efficiency of the NFT decreases as the flying height increases, i.e., to reach the Curie temperature, an increase in laser power is required at larger write spacing. It is important to note that a range from 1 nm to 8 nm write spacing is well within the range of near-field coupling effects.

6.3.3 Laser Current versus Media Design

We investigate two types of HAMR media, called media "A" and media "B". As can be seen in Figure 8, media A and B are very similar. They have the same magnetic layer, the same thermal insulation layer, heat sink layer and glass substrate. However, in media A, a capping layer of 2.5 nm thickness is deposited on top of the magnetic layer

[181]. This capping layer is absent in media B. A diamond like carbon overcoat layer of approximately 3.5 nm is deposited on top of the capping layer in media A. In media B, the capping layer is absent and the diamond-like carbon overcoat is 7 nm in thickness (Figure 6.8).

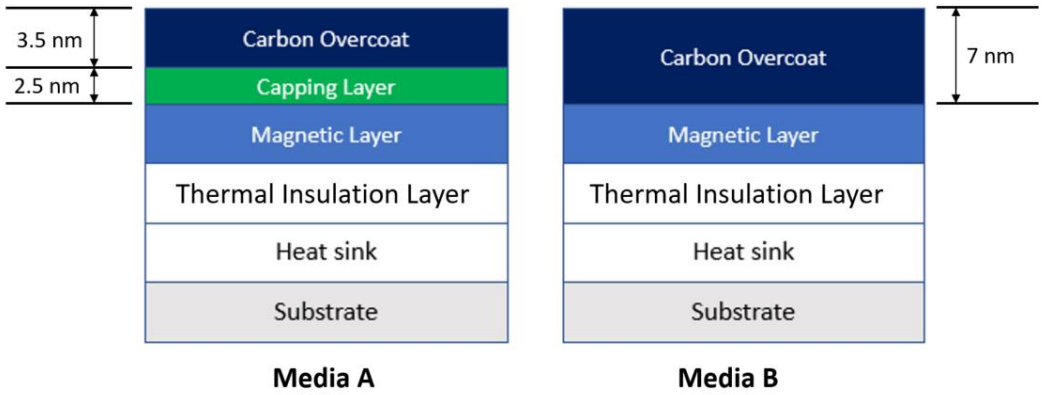

Figure 6.8 Schematic of media "A" (left) and media "B" (right). Media A consists of substrate, heat-sink, thermal insulation layer, magnetic layer, 2.5 nm capping layer, and 3.5 nm carbon overcoat layer. Media B consists of substrate, heat-sink, under layer, magnetic layer, and 7 nm carbon overcoat layer.

A similar measurement of the required laser power to achieve a track width of 60 nm was performed using the same HAMR heads as used in the earlier part of this study with the two types of media A and B. The flying height of the head was adjusted to be 2 nm during both reading and writing. We observe from Figure 6.9 that the required laser power for media A is approximatley 15% less than the required power for media B. Clearly, the use of a capping layer significantly reduces the optimal laser power.

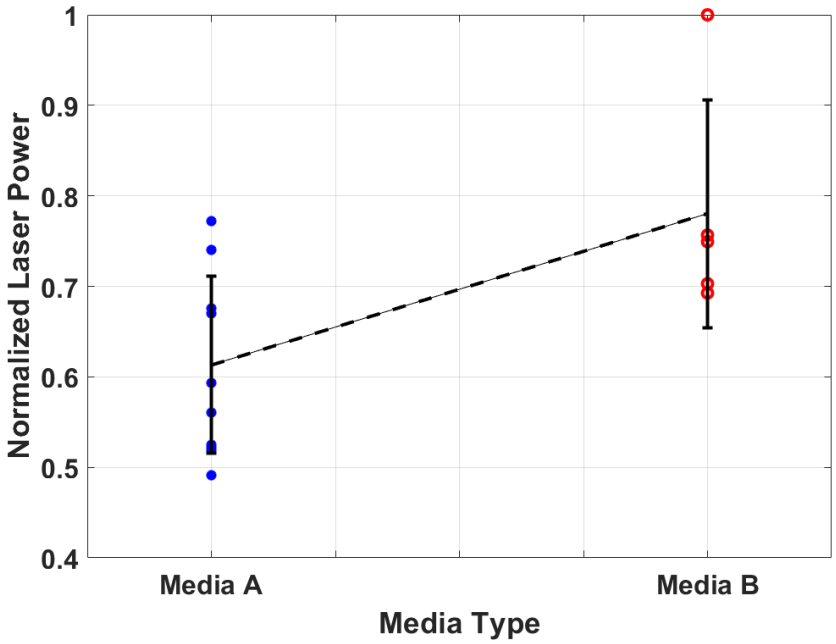

Figure 6.9 Laser current vs. media TA (having a cap layer) and media TB (without having a cap layer)

The difference in laser power for media type A and media type B can be explained by the different absorption of laser energy of both media layers. While the refractive index n of the capping layer (n_{Cap} ~ 2.3) is similar to that of the media overcoat (n_{MOC} ~ 2.2), the capping layer in media A has a much higher extinction coefficient (k_{Cap} ~ 1.5) than the carbon overcoat (k_{MOC} ~ 0.05) used in both media [182]. Thus, the laser energy absorption coefficient β of the capping layer is higher than the laser energy absorption coefficient of the media overcoat as shown in equation (6.3):

$$\beta = 4\pi k / \lambda \tag{6.3}$$

where β is the laser energy absorption coefficient, k is the extinction coefficient, and λ is the laser wavelength. Different absorption coefficients of the capping layer and the media overcoat cause different heat generation rate $\dot{Q}$ (equation 6.4) and, consequently, different

temperature T of the capping layer versus the media overcoat as shown in equation 6.5 [183].

$$\dot{Q}(\mathrm{x},\mathrm{y},\mathrm{z}) = \frac{P_w}{\pi r^2}\beta(1-R)e^{\frac{(x-x_0)^2+(\mathrm{y}-\mathrm{y}_o)^2}{r^2}}e^{-\beta z} \tag{6.4}$$

$$\frac{\partial T}{\partial t}(\mathrm{x},\mathrm{y},\mathrm{z}) = \alpha\left(\frac{\partial^2 T}{\partial x^2}+\frac{\partial^2 T}{\partial y^2}+\frac{\partial^2 T}{\partial \mathrm{z}^2}\right)+\frac{\dot{Q}}{\rho_a C_p} \tag{6.5}$$

In equation (6.4), P_w is the laser power, R is the reflectivity of the surface films, α, ρ_a, C_p are the thermal diffusivity, density and specific heat of the media layers, respectively, and r is the radius of the heated spot size. It is important to note from equation (6.4) and equation (6.5) that a higher absorption coefficient β of the capping layer results in a higher heat generation rate $\dot{Q}$ and, consequently, higher temperature T of the capping layer in media A compared to media B where the capping layer is absent. In media A, the higher temperature of the capping layer is the boundary condition for heat conduction to the recording layer. The higher temperature at the capping layer-media interface increases the temperature rise (heating efficiency) in media A compared to media B. This explains why media B requires an increase in laser power compared to media A.

6.4 Summary

The required laser current in heat assisted magnetic recording was investigated as a function of operating disk radius, head-disk "write" flying height, and media design. The following conclusions can be drawn:

1. The laser power increases as a function of operating disk radius for a given magnetic track width. The increase in laser power appears to be related to the increased cooling of the media at higher linear velocities, i.e., larger operating disk radii.
2. The laser power increases with an increase in the write flying height keeping the magnetic write track width constant. For the setup used, the required laser power at 8 nm “write” flying height was found to be higher by 8 % compared to the case of 1 nm “write” flying height.
3. Adding a capping layer of 2.5 nm thickness between the magnetic layer and the carbon overcoat reduces the laser power by approximately 15% for constant write track width. A reduction of the laser power is essential for improving the reliability of the HAMR head disk interface.

Chapter 6, in part, is currently being prepared for submission for publication of the material. "Laser Current Studies of Heat-Assisted Magnetic Recording", Tan Trinh, Sukumar Rajauria, Robert Smith, Erhard Schreck, Qing Dai, and Frank E. Talke, in preparation for submission to Microsystems Technologies, 2019. The dissertation author was the primary investigator and primary author of this paper.

Chapter 7

Life-Time Studies of the Head-Disk Interface in Heat-Assisted Magnetic Recording

7.1 Introduction

Heat-assisted magnetic recording (HAMR) is a promising technology that allows an increase of the areal density of hard drives beyond 1Tbits/in^2 [49], [51], [81], [184]. In heat-assisted magnetic recording (HAMR), a nanometer scale area on the disk surface is locally heated up to a temperature just below the Curie temperature (T_C) within a nanosecond that temporarily decreases the coercivity of the FePt-X magnetic layer [32], [181]. In order to achieve an areal density of 1Tbits/in^2, the diameter of the heated area on the disk surface must be approximately 50nm. To heat up the disk surface, optical energy from a laser diode mounted on the top of the slider is delivered through an optical wave-guide in the slider and coupled to the so-called "near-field" transducer, denoted as NFT. The near-field transducer (NFT) is embedded on the slider surface near the read and write elements that is located at a close proximity from the disk surface [51]. During the writing, temperature of the heated area on the disk surface is approximately 450°C, and temperature

of the near-field transducer is about 250°C [51], [181]. Such high temperature of the disk surface and the near-field transducer pose a great challenge on the tribological performance of the heat-assisted magnetic recording (HAMR) head-disk interface (HDI). A temperature increase of the head-disk interface reduces the reliability of the near-field transducer and causes degradation of the carbon overcoats and the lubricant layer on the disk surface. Ma et al. [185] studied the effect of laser heating on the degradation of the carbon overcoat layer on the disk surface. They observed degradation of carbon overcoat layer in form of hump and chemical structure changes. Ji et al. [186] and Seo et al. [187] studied the effect of laser heating on lubricant film property in HAMR heat-disk interface. Their studies show desorption and decomposition of the lubricant layer on the disk surface is a function of the duration of laser radiation and temperature. Degradation of the carbon overcoat and lubricant layer is critical for the reliability or life-time of the head-disk interface in heat-assisted magnetic recording (HAMR). Clearly, understanding of the parameters that affect life-time of the HAMR head-disk interface becomes a critical task.

In this study, HAMR heads and HAMR media were used to study life-time, or equivalently time-to-failure, of the HAMR head-disk interface. Life-time of the head-disk interface was determined by measuring changes of the signal-to-noise ratio as a function of time. Our experimental results show that the life-time of the HAMR head-disk interface is a strong function of the magnetic write width, which in turns is a function of the laser spot size and optical power of the laser. An exponential decrease in life-time is observed with an increase in the optical power of the laser.

7.2 Experimental Setup and Procedures

In this study, a component level tester, named Guzik tester, having a read and write capabilities is used for testing as presented in section 6.2. The experimental tester is enclosed inside a sealed environmental chamber with pressure sensor, temperature and humidity controllers, allowing a control of pressure, temprature and relative humidity inside the chamber. Testing was performed in air, at an ambient pressure (~1 atm), at a room temperature of 27°C, and at a low relative humidity level of 5%. A commercially available software package WITE32 [174], [180] was used to control the rotational speed of the spindle, the actuator arm, the thermal flying-height control (TFC) heater power, the applied laser current, the acquisition of the readback signal, and the environmental conditions inside the environmental chamber. In this study, the non-contact calibration technique using acoustic emission sensor, Wallace spacing mesurements, and burst writing scheme was used to control the spacing between head and disk surfaces as presented in section 6.2.1. The head-disk spacing during both the writing and reading process is maintained to be approximately 2nm. Testing was performed at the rotational speed of 7200 rpm, at the middle diameter (MD) location on the disk surface. After the slider was loaded to the middle diameter of the disk surface, the laser current and write gate were both activated to write data pattern on the disk surface using the read and write analyzer (Guzik Technical Enterprises). After data was written on the disk, the “track profile measurement” was performed to measure the magnetic write width of the written track.

In this study, the so-called life-time testing was performed to study the effect of life-time, or time-to-failure of the HAMR head-disk interface, as a function of the magnetic write width (MWW) and optical laser current. The testing procedure is shown in Fig. 7.1. Initially, the slider was loaded on a reference track at the middle diameter location of the disk surface. A head-disk clearance of 2 nm during the reading and writing process is calibrated using a micro heater element inside the thermal-flying height control (TFC) slider, Wallace spacing measurements and the burst writing scheme as presented using equations 6.1. Thereafter, the laser current was increased from 0mA in steps of 0.5mA and the magnetic write width was determined, keeping a constant writer current. The laser current that generates a desired magnetic write width, is called the optimal laser current (LC). After data is written on the disk surface the magnetic write width (MWW), the read width (RdWidth), the optimal laser current (LC) and the signal-to-noise (SNR) ratio were measured at the reference track before the head was moved to a different track, the so-called "stress-writing" tracks. At the stress writing tracks, the laser diode and the write coil were both turned on continuously for two minutes, keeping a head-disk clearance of 2nm, before the slider moves back to the reference track. This cycle was repeated over and over until the signal-to-noise ratio measured at the reference track was found to be decreased by more than 1 dB, i.e., until the head could not write data on the disk surface of the same quality as at the beginning of the test. The total writing duration of the testing is called a life-time of the HAMR head-disk interface.

To accelerate the life-time testing of the HAMR head-disk interface, larger magnetic write width (MWW) of 60nm, 70nm, 80nm, and 100nm were used for testing. A

large magnetic write width is likely to correspond to higher laser current that is applied to the laser diode, resulting in a higher temperature of the disk surface and the near-field transducer. In addition, two types of HAMR media, media "TA" and media "TB" as presented in section 6.3.3, were used for the life-time testing.

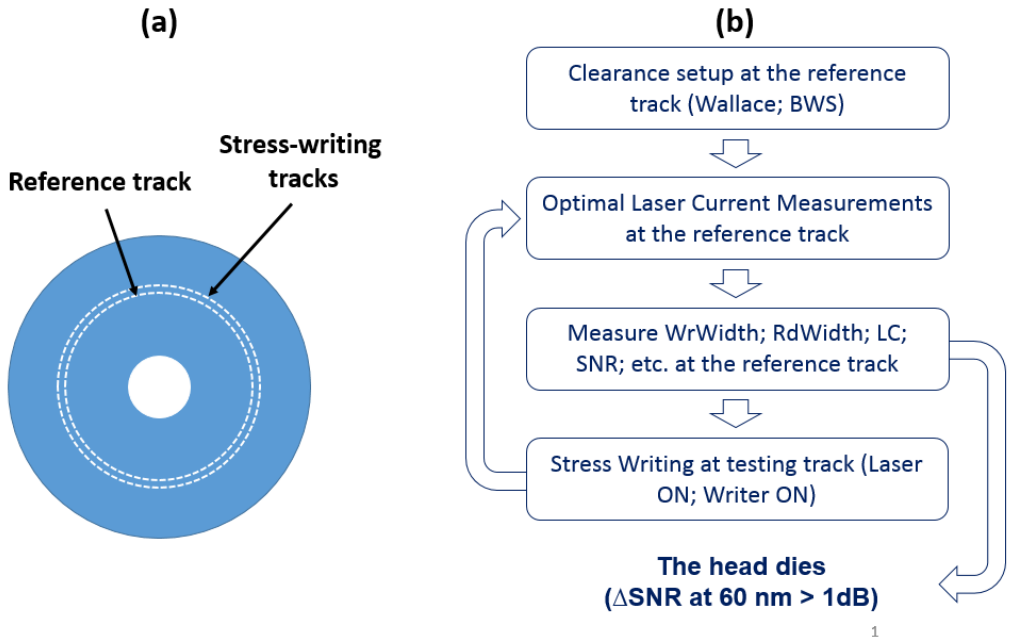

Figure 7.1 (a) Reference and stress-writing tracks (b) Life-time testing procedure

7.3 Experimental Results and Discussion

7.3.1 The Effect of Magnetic Write Width on Optimal Laser Current and NFT Protrusion

Fig. 7.2 (a) shows the optimal laser current (LC) is a function of the magnetic write width (MWW). We observe that the optimal laser current increases as the magnetic write width increases. As the magnetic write width increases from 60 nm to 100 nm, the optimal laser current was found to increase by approximately 20%. This increase corresponds to an

increase of 23% of the optical power applied to the laser diode. Using the previously described burst writing scheme [112], the near-field transducer protrusion was measured (Fig. 7.2(b)). For an increase in the magnetic write width from 60nm to 100nm, the near-field transducer protrusion increases by approximately 100%. An increase of the optical laser current is required to increase the magnetic write width. Clearly, an increase of the optical laser current leads to an increase in the temperature of the disk surface and the near-field transducer. This temperature increase at the near-field transducer results in an increase in the protrusion, the so-called NFT protrusion. An increase in the protrusion of the near-field transducer is related to the coupling efficiency of the optical laser power to the near-field transducer and temperature of the near-field transducer. Therefore, the relationship between applied laser current and near-field transducer protrusion is important for the design of the HAMR head-disk interface.

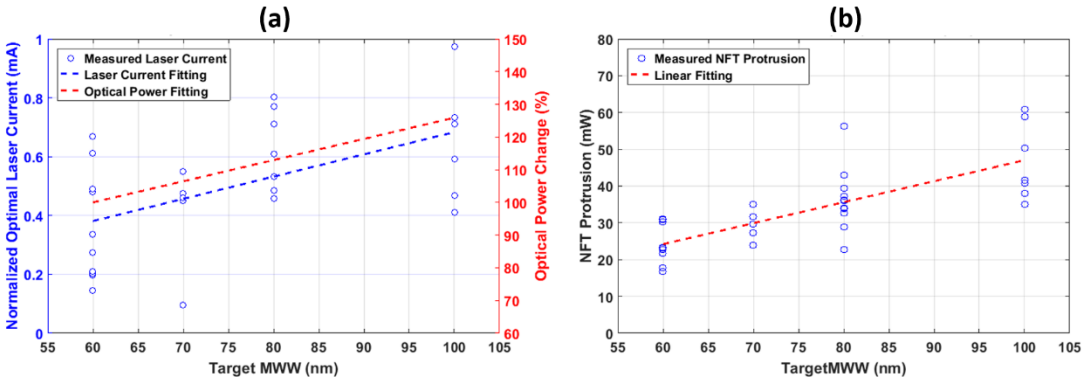

Figure 7.2 (a) Normalized optimal laser current and optimal laser power vs. magnetic write width (MWW) (b) Near-field transducer protrusion vs. magnetic write width (MWW)

7.3.2 Life-Time Study Results

During the life-time testing, the tribological characteristics of the head-disk interface was monitored. Typical magnetic write width, read width, optimal laser current and signal-to-noise ratio (SNR) measurements were shown to be a function of test duration. In Fig. 7.3, typical measurements are shown. We observe that at the beginning of a test, the optimal laser current decreases. This implies that a smaller laser current is required to achieve the same magnetic write width. Thereafter, the laser current reached a constant value, before increasing near the end of life-time of the recording head. The decrease of the optimal laser current at the beginning of the test is well known and is caused due to the formation of write-induced contamination at the head-disk interface, called "smear" [111]. Kiely et. al [188] suggested growth mechanisms for the smear at the head-disk interface is due to temperature difference between the hot spots of the head and the disk during writing. Kiely et al. experimentally observed that the smear height is a function of time as shown in equation (7.1):

$$h(t) = h_0 + Kt^{1/3} \qquad (7.1)$$

, where h(t) is the smear thickness, h_0 is the "critical nucleus height", K is the grow rate constant and t is time. However, contamination growth is inhibited by the head-media spacing that results in a formation of the smear that fulfills the spacing between the near-field transducer and the disk surface. More importantly, smear in the gap between the head and the disk has a higher thermal conductivity than air. This allows for good thermal coupling efficiency from the near-field transducer to the disk surface, i.e. the disk surface is heated up to the same temperature using a smaller input laser current. Thus, a smaller

laser current is required to achieve the same magnetic write width on the disk surface. After the smear if fully formed at the HAMR head-disk interface, the optimal laser current, the magnetic write width, the read width, and the signal-to-noise ratio were nearly constant until end of the life-time testing. At the end of the life-time testing, the signal-to-noise ratio measured decreases significantly compared to that at the beginning of the test as shown in Figure 7.3. A decrease of the signal-to-noise ratio is likely related to the failure of the near-field transducer, i.e. the near-field transducer is not able to couple laser optical power to heat up the disk surface. As the disk surface is not heated up to reach the Curie temperature, the writing quality is low and the readback signal is poor (Figure 7.4), leading to a decrease of the signal-to-noise ratio at the reference track. In addition, we observe that at the end of life-time testing, the optimal laser current increases significantly together with the increase of the magnetic write width and the read width. This implies that the near-field transducer does not transmit enough optical energy required for reaching the Curie temperature on the disk surface, even at a much higher laser current. Increasing the laser current leads to an

increase of the heated spot size on the disk surface, i.e. an increase of the magnetic write width and the read width as shown in Fig. 7.3.

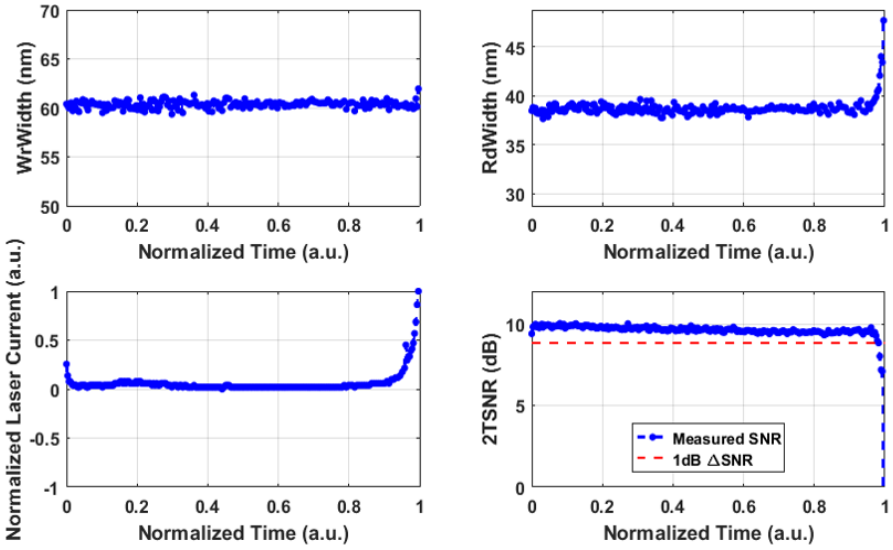

Figure 7.3 Typical magnetic write width, reader width, optimal laser current and signal-to-noise ratio measurements during life-time testing

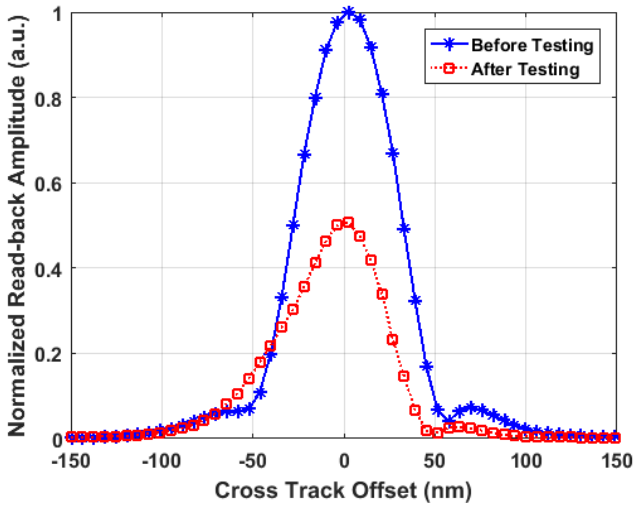

Figure 7.4 Readback Signal before and after life-time testing

7.3.3 Life Time as a Function of Magnetic Write Width (MWW) and Media Types

After the life-time testing was performed, Weibull distribution is used to study life-time of the head-disk interface as a function of the magnetic write width (Fig. 7.5). In Fig. 7.5, the triangles denote heads that maintained similar writing performance at the beginning and end of the testing. Those heads were "truncated" after a fixed period of time and is considered to be alive after testing. Most of the heads, however, failed during life-time testing, the so-called "dead" heads. We observe that an increase in magnetic write width (MWW) from 60 nm to 100 nm causes a reduction of the life-time of HAMR recording heads by approximately 10 times. We hypothesize that this is related to an increase of the laser current or the optical power that was delivered from the laser diode to the media surface.

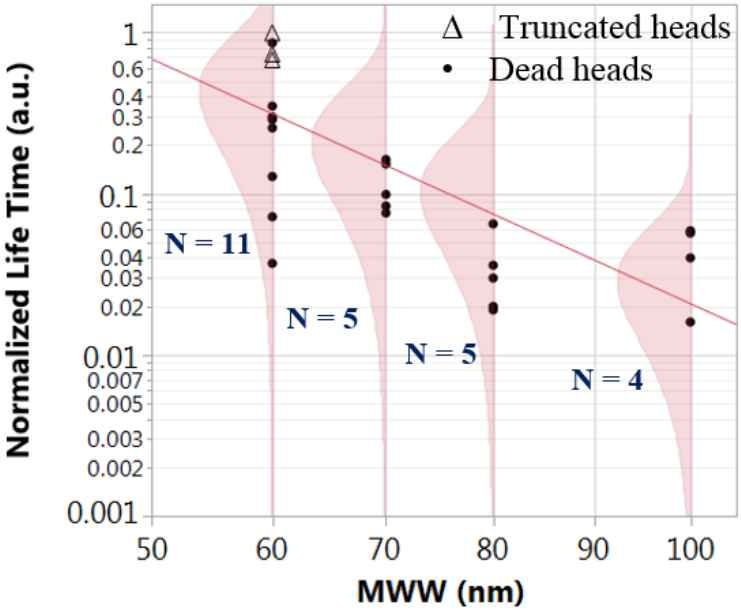

Figure 7.5 Normalized life-time data of HAMR heads as a function of the magnetic write width (MWW)

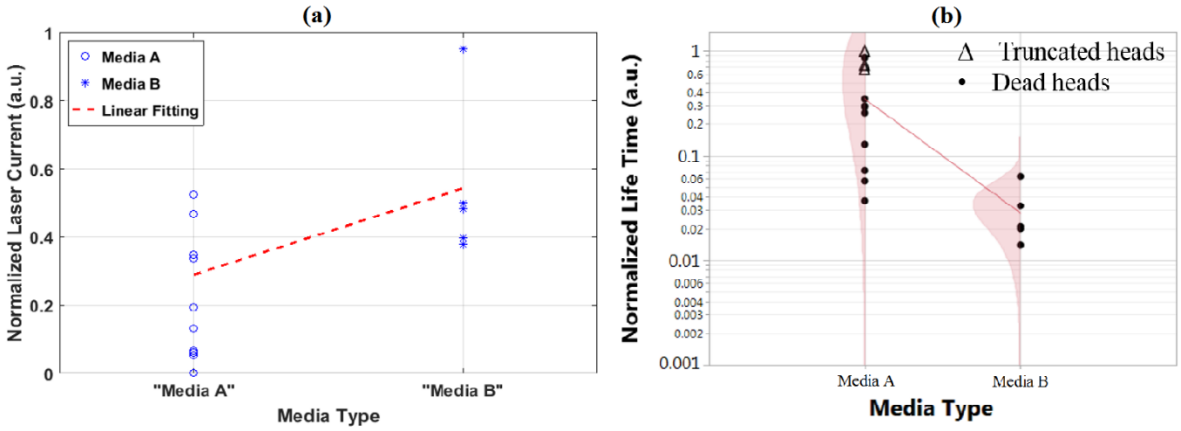

Figure 7.6 (a) Optimal laser current vs. media type (b) Normalized life-time vs. media type

To confirm this hypothesis, the two types of HAMR media, "TA" and "TB", that are presented in section 6.3.3 were used for testing. We observe that the touchdown power for media "TA" and media "TB" using the same heads was found to be similar, i.e. the two types of media have similar surface roughness. As presented in section 6.3.3, media "TA" has an extra capping layer of approximately 2.5nm on the top of the magnetic layer made of FePt-X material. The capping layer is absent in media "TB". It was found that media "TB" has a higher optimal laser current than the media A, keeping the same magnetic write width of 60 nm. Fig. 7.6 (a) shows an increase of the optimal laser current by 21% using media "TB" compared to the media "TA" for the same magnetic write width of 60nm. In addition, the near-field transducer protrusion was 41% larger on the media "TB" compared to media "TA". Life-time testing on both media "TA" and media "TB" shows that the life-time of the same type of HAMR recording heads on media "TB" is 10 times shorter than on media "TA" as shown in Figure 7.5. The result is interesting as the laser current for media TB is equivalent to the laser current for media TA at 100nm magnetic write width. And for both cases, the life-time of the HAMR head-disk interface is decreased by

approximately 10 times. Clearly, an increase in optimal laser current is a dominant effect that decreases the life-time of the head-disk interface. More importantly, for the same magnetic write width of 60nm, it is justifiable to assume that temperature on the disk surface for both media "TA" and "TB" is the same as the magnetic layer FePt-X is similar. Thus, temperature on the disk surface is less likely to have big impact on the big difference on reliability of the HAMR head-disk interface. Simulation results of the HAMR head-disk interface for media "TA" and "TB" as presented in Figure 6.10 in section 6.3.3 shows that maximum temperature of the near-field transducer at media TB is 20% increased compared to media TA. Assuming HAMR head-disk interface temperature is the only factor that affects the life-time measurements, temperature of the near-field transducer is a dominant factor for the reliability of the HAMR head-disk interface. A reliable near-field transducer is required to withstand extremely high temperature during the writing process, thus increases the life-time of the head-disk interface.

Fig. 7.6 shows the relationship between the measured optical power and life-time of all HAMR heads during the life-time testing. The x-axis shows the normalized optical power of all heads and the y-axis shows corresponding life-time measurements of the heads on semi-logarithmic scale. The data is distributive that is likely caused due to the alignment of the laser diode on the top of the slider, resulting in a coupling efficiency difference between the HAMR heads. An exponential fitting can be used to estimate the life-time of the HAMR head-disk interface as a function of the laser optical power. We observe that the life-time of the HAMR head-disk interface decreases exponentially. A reduction of life-time of the HAMR head-disk interface is a strong function of the optimal laser current.

Optimizing laser current is required for the improvement of the reliability of the head-disk interface.

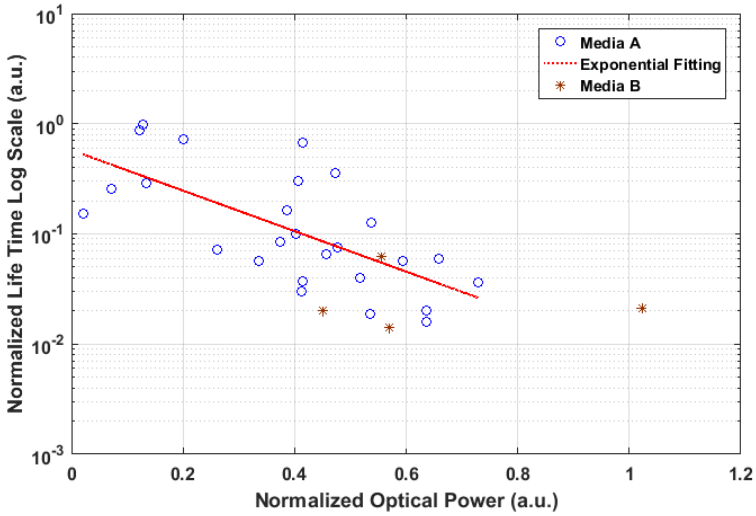

Figure 7.7 Normalized Life-time measurements as a function of normalized laser optical power

7.3.4 Atomic Force Microscopy Measurements

After life-time testing, atomic force microscopy (AFM) measurements were performed at the read and write transducer area. Typical AFM images of the slider surface are shown in Fig. 7.8. We observe that smear is present on the slider surface around the near-field transducer area. During the writing process, smear grows and fills the gap between the head and the slider. Measuring the height of the smear layer can be used to estimate the head-media clearance (Fig. 7.8 (d)). We observe that the thickness of the smear layer is approximately 2 nm, raised above the main write pole area. This finding suggests that the head-disk clearance is approximately 2 nm. In addition, smear was elongated on the slider surface, likely to be caused due to the temperature differences on the slider surface. This results in a movement of contamination from one hot spot area, i.e., the near-field transducer, to the cooler areas of the slider surface. The direction of the smear follows

the skew angle of the recording head at the MD location. Clearly, it suggests that smear growth is related to shear on the slider surface or possibly to mechanically-induced contacts between the smear and the disk surface. Fig. 7.8 shows that the smear is a strong function of the magnetic write width. Smear formation is more severe at 100 nm compared to those at 80 nm and 60 nm magnetic write width. As the magnetic write width increases, the temperature at the head-disk interface increases, notably the temperature of the near-field transducer. This suggests that an increase in the temperature of the head-disk interface is important for the amount of smear adhering on the slider surface.

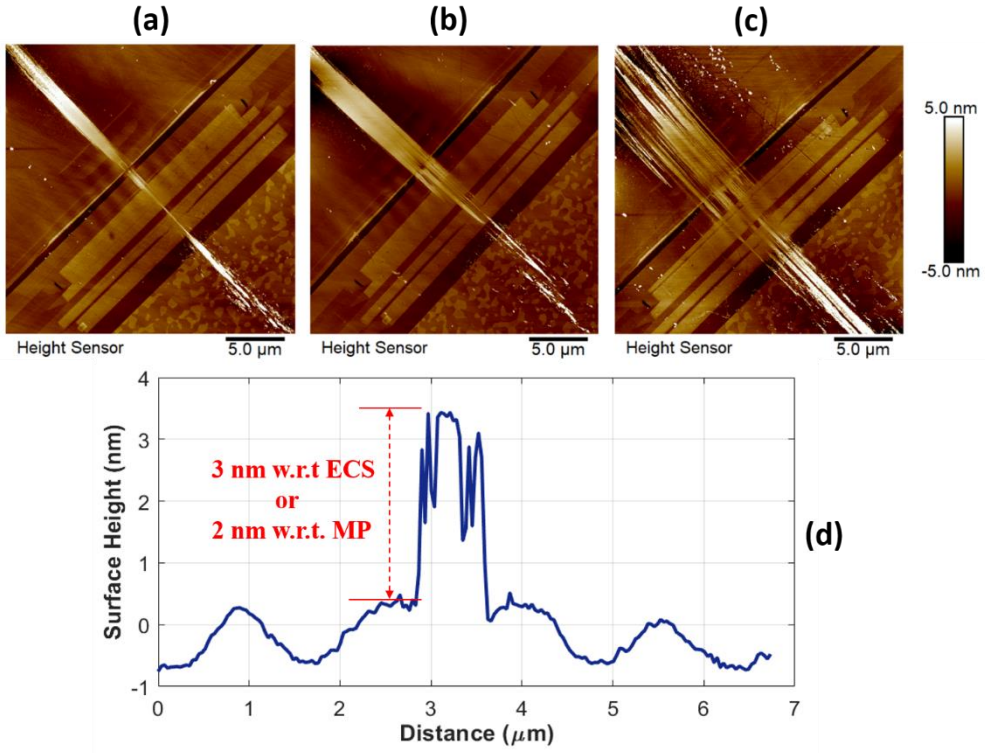

Figure 7.8 Atomic force microscopy images at (a) 60 nm (b) 80 nm (c) 100 nm magnetic write width (d) A surface height measurement: the smear height is approximately 2 nm with respect to the main write pole

7.4 Summary

In this chapter, we presented a novel experimental study to investigate the effect of laser current or laser optical power on the reliability of the heat-assisted magnetic recording (HAMR) head-disk interface. In this study, an integrated HAMR heads and HAMR media was used for testing using a component-level tester Guzik tester (Guzik Technical Enterprises). An in-situ non-contact method using thermal flying height control slider, Wallace spacing measurements and acoustic emission sensor was performed to calibrate the flying height of the slider of approximately 2nm during both the writing and reading process. Atomic force microscopy measurements were performed after testing to validate the desired flying height that shows excellent agreement. The magnetic write width was measured and was used as an accelerated testing condition for the life-time study of heat-assisted magnetic recording head-disk interface. Life-time study was performed at 60nm, 70nm, 80nm, and 100nm magnetic write width. During the life-time study, different metrics were measured that includes the magnetic write width (MWW), the read width (RW), and signal-to-noise ratio (SNR). The head is considered to be no longer operational when the signal-to-noise ratio is decreased by more than 1dB, i.e. the slider cannot write on the disk surface of the same quality as the untested slider. Our experimental results show that life-time of the heat-assisted magnetic recording (HAMR) is a strong function of the magnetic write width. As the magnetic write width increases, the optimal laser current linearly increases, showing that life-time of the heat-assisted magnetic recording is a direct function of the laser optimal power. As the laser power increases, life-time of the heat-assisted magnetic recording decreases exponentially. More importantly, an increase of the

temperature at the near-field transducer is observed to be a dominant factor that affects the reliability of the HAMR head-disk interface.

Chapter 7, in part is currently being prepared for submission for publication of the material. "Temperature induced near field transducer (NFT) failure in heat-assisted magnetic recording (HAMR)," Tan Trinh, Sukumar Rajauria, Robert Smith, Erhard Schreck, Qing Dai, and Frank E. Talke, submitted to *IEEE Transactions on Magnetics,* 2019. The dissertation author was the primary investigator and primary author of this paper.

Chapter 8

Summary and Conclusion

As the head-disk spacing in current hard disk drives is reduced to less than a nanometer, tribology of the head-disk interface becomes increasingly more important for the reliability of the hard disk drives. In this dissertation, we have studied the effect of bias voltage and helium environment on the tribological characteristics of the head-disk interface.

First, we have simulated numerically the effect of bias voltage and helium environment on the flying characteristics of the slider. For this study, we used a finite element analysis based simulation to simultaneously solve the Reynolds equations and the slider equilibrium equations. Our study shows that the electrostatic forces between head and disk have a large effect on the flying characteristics, including the minimum flying height, pitch and roll angles of the slider. The electrostatic forces of 1V potential difference between head and disk were shown to be approximately 16 times larger compared to well-known Van-der-Waals forces, causing the minimum flying height of the slider to decrease by approximately 0.5nm.

Thereafter, we performed experiments to study the effects of helium on wear and surface degradation of slider surfaces during the ramp load-unload process. In this study, an experimental tester was built that was located inside a sealed environmental chamber with various sensors to allow control of pressure, humidity, and air and helium

concentrations. We performed load-unload testing that consisted of 10,000 wear cycles and used atomic force microscopy and optical surface analysis to study wear on the slider surfaces and lubricant redistribution on the media surface. Atomic force measurements show that wear and scratches are much less noticeable in helium environment compared to air environment. Optical surface analyzer results also confirm that the lubricant redistribution in helium environment is reduced significantly compared to air environment. Clearly, helium is important for improving wear and lubricant transfer at the head-disk interface.

To understand the effect of bias voltage on the tribological performance of the head-disk interface, we have performed burnishing tests in the presence of bias voltage. We have varied the relative humidity conditions from 5% to 45% and 85% using a commercially available VENA environmental controller. We have measured the contact potential difference across the head-disk interface using a "power-to-contact (PtC)" as a function of applied bias voltages. Different bias voltages were applied to the disk surface keeping the slider surface grounded. A burnishing test was performed by applying an additional 30mW heater power for approximately 20 minutes at different humidity conditions (5%, 45%, and 85%). After testing, the sliders were investigated using Atomic Force Microscopy (AFM). We observed that at all humidity conditions (5%, 45%, and 85%), wear was seen to increase at the negative bias voltages compared to positive bias voltages. At 45% and 85% relative humidity, AFM measurements showed a good agreement with the power-to-contact measurements. However, at 5% relative humidity, power-to-contact measurements do not agree with wear of the slider surface using Atomic Force Microscopy (AFM). Substantially, less material buildup is observed at 5% relative humidity than at 45% and

85% relative humidity. The difference in the amount of material build-up can be explained by the presence of di-electrophoresis. Electrostatic Force Microscopy (EFM) was used to study the electrical conductivity of the material build-up on the head surface. One of the interesting observation in our study is that pit formation is observed at 85% relative humidity and at large positive bias voltage cases. Pit formation is likely caused by the breakdown of the carbon overcoat layer on the slider surface caused as a consequence of the bias voltage at high relative humidity or due to the corrosion effects at the pre-existing pits on the slider surface. A hypothesis of "stray current corrosion" is suggested to explain the difference in corrosion sites on the head surface after switching the polarity of the bias voltage from +1.35V to -1.35V.

At the end of the dissertation, we studied optimal laser currents in heat-assisted magnetic recording (HAMR) as a function of magnetic write width, operating radius, head-disk clearance, and media design. We have observed that the laser current increases as the operating radius increases. Optical laser current was found to increase by approximately 20% as the slider moves from the inner diameter (ID) to the outer diameter (OD) on the disk surface. Increasing the head-disk spacing from 2nm to 8nm leads to an increase of the laser current by approximately 10%. Increasing the laser current also leads to an increase in the heated area on the media surface. This is equivalent to increasing the magnetic write width (MWW) on the disk surface. The media design plays a crucial role in reducing the laser current in heat-assisted magnetic recording. We have observed that the laser current decreased by approximately 20% by adding "capping" layer of approximately 2.5nm. The optimal laser current is shown to be independent of the thickness of the diamond-like carbon overcoat layer on the disk surface. A systematic study of the reliability of the head-

disk interface in heat-assisted magnetic recording was performed using a component level tester (Guzik tester) with read-write capabilities. The life-time study was performed at two different tracks, the so-called reference track and the stress-writing track, to monitor the writing performance of HAMR heads and HAMR disk. The end of the life-time is detected if the signal-to-noise ratio of the readback signal has decreased by more than 1dB. Our experimental results showed that life-time of the head-disk interface is a strong function of the magnetic write width and the optical laser power that is applied to the laser diode. We have found that life-time of the HAMR head-disk interface is reduced exponentially with an increase in laser optical power or laser current. Optimizing the laser current is very important for improving the reliability of the head-disk interface.

In conclusion, the studies presented in this dissertation helps to improve the understanding of the tribological performance of the head-disk interface in hard disk drives in helium environment and in the presence of bias voltages. Our results in the reliability of heat-assisted magnetic recording (HAMR) provide a guideline on the effect of the most important factors on the laser power. Life-time experimental data reveals that the most dominant factor that affect the reliability of the HAMR head-disk interface that can be used to design more reliable HAMR heads and disks.

Future investigations of bias voltage application and humidity in heat-assisted magnetic recording should be performed in an attempt to optimize wear and smear on the slider surface in air and helium environment.

REFERENCES

[1] T. U. Daim, P. Ploykitikoon, E. Kennedy, and W. Choothian, “Forecasting the future of data storage: case of hard disk drive and flash memory,” *Foresight*, vol. 10, no. 5, pp. 34–49, Aug. 2008.

[2] K. Kim and S. Y. Lee, “Memory technology in the future,” *Microelectron. Eng.*, vol. 84, no. 9–10, pp. 1976–1981, Sep. 2007.

[3] R. Haavind, “The great race: flash vs. magnetic storage,” *Solid State Technol.*, vol. 50, no. 9, pp. S6–S6, Sep. 2007.

[4] Christine Taylor, “SSD vs HDD,” *Enterprise Storage Forum*, 2018. [Online]. Available: https://www.enterprisestorageforum.com/storage-hardware/ssd-vs-hdd.html. [Accessed: 05-Jun-2019].

[5] D. Tang, “Innovating to Fuel the Next Decade of Big Data.”

[6] Ralph Jacobson, “2.5 quintillion bytes of data created every day. How does CPG & Retail manage it? - IBM Consumer Products Industry Blog,” *IBM Consumer Products Industry Blog*, 2013. [Online]. Available: https://www.ibm.com/blogs/insights-on-business/consumer-products/2-5-quintillion-bytes-of-data-created-every-day-how-does-cpg-retail-manage-it/. [Accessed: 05-Jun-2019].

[7] D. Reinsel, J. Gantz, and J. Rydning, “The Digitization of the World From Edge to Core,” 2018.

[8] Joe McKendrick, “What Pioneering Enterprises Are Telling Us About Artificial Intelligence,” *Forbes*. [Online]. Available: https://www.forbes.com/sites/joemckendrick/2019/01/28/what-pioneering-enterprises-are-telling-us-about-artificial-intelligence/#605444b4189f. [Accessed: 05-Jun-2019].

[9] “IBM Archives: IBM 350 disk storage unit,” *IBM*. [Online]. Available: https://www.ibm.com/ibm/history/exhibits/storage/storage_350.html. [Accessed: 05-Jun-2019].

[10] “IBM Archives: IBM 1301 disk storage unit,” *IBM*. [Online]. Available: https://www.ibm.com/ibm/history/exhibits/storage/storage_1301.html. [Accessed: 05-Jun-2019].

[11] “IBM Archives: IBM 1311 disk storage drive,” *IBM*. [Online]. Available: https://www.ibm.com/ibm/history/exhibits/storage/storage_1311.html. [Accessed: 05-Jun-2019].

[12] “1965: First cartridge HDD and voice coil actuator | The Storage Engine | Computer

History Museum," *IBM*. [Online]. Available: https://www.computerhistory.org/storageengine/first-cartridge-hdd-and-voice-coil-actuator/. [Accessed: 05-Jun-2019].

[13] "1973: "Winchester" pioneers key HDD technology | The Storage Engine | Computer History Museum," *IBM*. [Online]. Available: https://www.computerhistory.org/storageengine/winchester-pioneers-key-hdd-technology/. [Accessed: 05-Jun-2019].

[14] "1979: Thin-film heads introduced for large disks | The Storage Engine | Computer History Museum," *Computer History*. [Online]. Available: https://www.computerhistory.org/storageengine/thin-film-heads-introduced-for-large-disks/. [Accessed: 05-Jun-2019].

[15] "Timeline: 50 Years of Hard Drives | PCWorld," *PCWorld*. [Online]. Available: https://www.pcworld.com/article/127105/article.html. [Accessed: 05-Jun-2019].

[16] "1990: Magnetoresistive read-head HDD introduced | The Storage Engine | Computer History Museum," *Computer History*. [Online]. Available: https://www.computerhistory.org/storageengine/magnetoresistive-read-head-hdd-introduced/. [Accessed: 05-Jun-2019].

[17] M. N. Baibich, J. M. Broto, A. Fert, Nguyen Van Dau, F. Petroff, P. Etienne, G. Creuzet, A. Friederich, J. Chazelas, "Giant Magnetoresistance of (001)Fe/(001)Cr Magnetic Superlattices," *Phys. Rev. Lett.*, vol. 61, no. 21, pp. 2472–2475, Nov. 1988.

[18] "IBM Archives: IBM 3340 direct access storage facility." [Online]. Available: https://www.ibm.com/ibm/history/exhibits/storage/storage_3340.html. [Accessed: 18-Jul-2019].

[19] S. Mao, Y. Chen, F. Liu, X. Chen, B. Xu, P. Lu, M. Patwari, H. Xi, C. Chang, B. Miller, D. Menard, B. Pant, J. Loven, K. Duxstad, S. Li, Z. Zhang, A. Johnston, R. Lamberton, M. Gubbins, T. McLaughlin, J. Gadbois, J. Ding, B. Cross, S. Xue, P. Ryan., "Commercial TMR heads for hard disk drives: characterization and extendibility at 300 gbit ^{2}," *IEEE Trans. Magn.*, vol. 42, no. 2, pp. 97–102, Feb. 2006.

[20] I. R. McFadyen, E. E. Fullerton, and M. J. Carey, "State-of-the-Art Magnetic Hard Disk Drives," *MRS Bull.*, vol. 31, no. 5, pp. 379–383, May 2006.

[21] "GMR und Festplattentechnologie." [Online]. Available: http://www.peter-lemmens.de/vorlesung-ws02-dateien/gmr-festplatten.htm. [Accessed: 18-Jul-2019].

[22] D. Weller and M. F. Doerner, "Extremely High-Density Longitudinal Magnetic Recording Media," *Annu. Rev. Mater. Sci.*, vol. 30, no. 1, pp. 611–644, Aug. 2000.

[23] S. Iwasaki, “Perpendicular magnetic recording—Its development and realization,” *J. Magn. Magn. Mater.*, vol. 324, no. 3, pp. 244–247, Feb. 2012.

[24] R. H. Victora, Jianhua Xue, and M. Patwari, “Areal density limits for perpendicular magnetic recording,” *IEEE Trans. Magn.*, vol. 38, no. 5, pp. 1886–1891, Sep. 2002.

[25] M. Mallary, A. Torabi, and M. Benakli, “One terabit per square inch perpendicular recording conceptual design,” *IEEE Trans. Magn.*, vol. 38, no. 4, pp. 1719–1724, Jul. 2002.

[26] C. Tannous and R. L. Comstock, “Magnetic Information-Storage Materials,” in *Springer Handbook of Electronic and Photonic Materials*, Cham: Springer International Publishing, 2017, pp. 1–1.

[27] “Magnetic Recording Media editor-in-chief and publisher Hisao Shigekane.”

[28] M. T. Kief and R. H. Victora, “Materials for heat-assisted magnetic recording,” *MRS Bull.*, vol. 43, no. 2, pp. 87–92, Feb. 2018.

[29] D. Jiles, *Introduction to magnetism and magnetic materials*. 2015.

[30] Jorgensen F., *The Complete Handbook Of Magnetic Recording Find your books library Online reading group Finn Jorgensen*. 1996.

[31] J.-Y. Juang and D. B. Bogy, “Air-Bearing Effects on Actuated Thermal Pole-Tip Protrusion for Hard Disk Drives,” *J. Tribol.*, vol. 129, no. 3, p. 570, Jul. 2007.

[32] D. Weller, O. Mosendz, G. Parker, S. Pisana, and T. S. Santos, “L1 $_0$ FePtX-Y media for heat-assisted magnetic recording,” *Phys. status solidi*, vol. 210, no. 7, pp. 1245–1260, Jul. 2013.

[33] E. Della Torre, *Magnetic hysteresis*. IEEE Press, 1999.

[34] S. Kasap and P. Capper, Eds., *Springer Handbook of Electronic and Photonic Materials*. Cham: Springer International Publishing, 2017.

[35] J. M. Daughton, “GMR applications,” *J. Magn. Magn. Mater.*, vol. 192, no. 2, pp. 334–342, Feb. 1999.

[36] E. Grochowski and R. F. Hoyt, “Future trends in hard disk drives,” *IEEE Trans. Magn.*, vol. 32, no. 3, pp. 1850–1854, May 1996.

[37] M. P. Jan van Ek, *The Physics of Ultra-High-Density Magnetic Recording - Google Books*. 2012.

[38] R. Wood, M. Williams, A. Kavcic, and J. Miles, “The Feasibility of Magnetic Recording at 10 Terabits Per Square Inch on Conventional Media,” *IEEE Trans.*

Magn., vol. 45, no. 2, pp. 917–923, Feb. 2009.

[39] K. O'Grady and H. Laidler, "The limits to magnetic recording — media considerations," *J. Magn. Magn. Mater.*, vol. 200, no. 1–3, pp. 616–633, Oct. 1999.

[40] "1.2 Magnetic recording crisis and challenges." [Online]. Available: http://www.fgarciasanchez.es/thesisfelipe/node5.html. [Accessed: 18-Jul-2019].

[41] K. Keng Teo, M. R. Elidrissi, K. S. Chan, and Y. Kanai, "Analysis and design of shingled magnetic recording systems," *J. Appl. Phys.*, vol. 111, no. 7, p. 07B716, Apr. 2012.

[42] "Shingled Magnetic Recording + HelioSeal ® Technology Achieving Unprecedented Storage Capacity Through Innovation," 2018.

[43] T. Feldman, "Shingled Magnetic Recording Areal Density Increase Requires New Data Management T I M F E L D M A N A N D G A R T H G I B S O N."

[44] "Breaking Capacity Barriers With Seagate Shingled Magnetic Recording | Seagate US," *Seagate Technology*. [Online]. Available: https://www.seagate.com/tech-insights/breaking-areal-density-barriers-with-seagate-smr-master-ti/. [Accessed: 05-Jun-2019].

[45] R. Wood, "IEEE Magnetics Society Santa Clara Valley Chapter Shingled Magnetic Recording and Two-Dimensional Magnetic Recording INSIC EHDR Program," 2010.

[46] Anton Shilov, "Western Digital: Over Half of Data Center HDDs Will Use SMR by 2023," *AnandTech*. [Online]. Available: https://www.anandtech.com/show/14099/western-digital-over-half-of-dc-hdds-will-use-smr-by-2023. [Accessed: 05-Jun-2019].

[47] J.-G. Zhu, X. Zhu, and Y. Tang, "Microwave Assisted Magnetic Recording," *IEEE Trans. Magn.*, vol. 44, no. 1, pp. 125–131, Jan. 2008.

[48] T. Taniguchi and H. Kubota, "Spin torque oscillator for microwave assisted magnetization reversal," *Jpn. J. Appl. Phys.*, vol. 57, no. 5, p. 053001, May 2018.

[49] G. Ju, Y. Peng, E. K. C. Chang, Y. Ding, A. Q. Wu, X. Zhu, Y. Kubota, T. J. Klemmer, H. Amini, L. Gao, Z. Fan, T. Rausch, P. Subedi, M. Ma, S. Kalarickal, C. J. Rea, D. V. Dimitrov, P. W. Huang, K. Wang, X. Chen, C. Peng, W. Chen, J. W. Dykes, M. A. Seigler, E. C. Gage, R. Chantrell, J-U. Thiele, "High Density Heat-Assisted Magnetic Recording Media and Advanced Characterization—Progress and Challenges," *IEEE Trans. Magn.*, vol. 51, no. 11, pp. 1–9, Nov. 2015.

[50] L. Pan and D. B. Bogy, "Heat-assisted magnetic recording," *Nat. Photonics*, vol. 3, no. 4, pp. 189–190, Apr. 2009.

[51] M. H. Kryder, E. C. Gage, T. W. McDaniel, W. A. Challener, R. E. Rottmayer, G. Ju, Y-T. Hsia, M. F. Erden, "Heat Assisted Magnetic Recording," *Proc. IEEE*, vol. 96, no. 11, pp. 1810–1835, Nov. 2008.

[52] W. A. Challener, C. Peng, A. V. Itagi, D. Karns, W. Peng, Y. Peng, X. Yang, X. Zhu, N. J. Gokemeijer, Y.-T. Hsia, G. Ju, R. E. Rottmayer, M. A. Seigler, E. C. Gage, "Heat-assisted magnetic recording by a near-field transducer with efficient optical energy transfer," *Nat. Photonics*, vol. 3, no. 4, pp. 220–224, Apr. 2009.

[53] W. A. Challener and A. V. Itagi, "Near-Field Optics for Heat-Assisted Magnetic Recording (Experiment, Theory, and Modeling)," Springer, New York, NY, 2009, pp. 53–111.

[54] B. Marchon, X. C. Guo, B. K. Pathem, F. Rose, Q. Dai, N. Feliss, E. Schreck, J. Reiner, O. Mosendz, K. Takano, H. Do, J. Burns, Y. Saito, "Head–Disk Interface Materials Issues in Heat-Assisted Magnetic Recording," *IEEE Trans. Magn.*, vol. 50, no. 3, pp. 137–143, Mar. 2014.

[55] H. J. Richter, A. Y. Dobin, R. T. Lynch, D. Weller, R. M. Brockie, O. Heinoken, K. Z. Gao, J. Xue, R. J. M. v. d. Veerdonk, P. Asselin, M. F. Erden, "Recording potential of bit-patterned media," *Appl. Phys. Lett.*, vol. 88, no. 22, p. 222512, May 2006.

[56] A. Kikitsu, "Prospects for bit patterned media for high-density magnetic recording," *J. Magn. Magn. Mater.*, vol. 321, no. 6, pp. 526–530, Mar. 2009.

[57] T. R. Albrecht, D. Bedau, E. Dobisz, H. Gao, M. Grobis, O. Hellwig, D. Kercher, J. Lille, E. Marinero, K. Patel, R. Ruiz, M. E. Schabes, L. Wan, D. Weller, T.-W. Wu, "Bit Patterned Media at 1 Tdot/in^{2} and Beyond," *IEEE Trans. Magn.*, vol. 49, no. 2, pp. 773–778, Feb. 2013.

[58] J. K. W. Yang, Chen Y., Huang T. Duan H., Thiyagarajah N., Hui H. K., Leong S. H., Ng Y., "Fabrication and characterization of bit-patterned media beyond 1.5 Tbit/in ^{2}," *Nanotechnology*, vol. 22, no. 38, p. 385301, Sep. 2011.

[59] Y. Wang and J.-G. Zhu, "Understanding Noise Mechanism in Small Grain Size Perpendicular Thin Film Media," *IEEE Trans. Magn.*, vol. 46, no. 6, pp. 2391–2393, Jun. 2010.

[60] G. Francis, "Data Storage-Trends and Directions," 2011.

[61] B. Shahsavari, E. Keikha, F. Zhang, and R. Horowitz, "Repeatable Runout Following in Bit Patterned Media Recording," in *2014 Conference on Information Storage and Processing Systems*, 2014, p. V001T03A001.

[62] "Hard Disk (Hard Drive) Performance - transfer rates, latency and seek times," *PCTechGuide*. [Online]. Available: https://www.pctechguide.com/hard-disks/hard-

disk-hard-drive-performance-transfer-rates-latency-and-seek-times. [Accessed: 12-Jun-2019].

[63] "SSD and HDD Speed," *Enterprise Storage Forum*. [Online]. Available: https://www.enterprisestorageforum.com/storage-hardware/ssd-vs-hdd-speed.html. [Accessed: 06-Jun-2019].

[64] G. Bouchard, L. Lau, and F. Talke, "An investigation of non-repeatable spindle runout," *IEEE Trans. Magn.*, vol. 23, no. 5, pp. 3687–3689, Sep. 1987.

[65] A. C. Swann, J. C. Harrison, and F. E. Talke, "Non-repeatable runout measurement and simulation of fluid lubricated spindles," *IEEE Trans. Magn.*, vol. 32, no. 3, pp. 1727–1732, May 1996.

[66] A. H. Sacks, M. Bodson, and W. Messner, "Advanced methods for repeatable runout compensation [disc drives," *IEEE Trans. Magn.*, vol. 31, no. 2, pp. 1031–1036, Mar. 1995.

[67] Shang-Chen Wu and M. Tomizuka, "Repeatable runout compensation for hard disk drives using adaptive feedforward cancellation," in *2006 American Control Conference*, 2006, p. 6 pp.

[68] Gunhee Jang, Dongkyun Kim, and Jae-Eung Oh, "New frequency domain method of nonrepeatable runout measurement in a hard disk drive spindle motor," *IEEE Trans. Magn.*, vol. 35, no. 2, pp. 833–838, Mar. 1999.

[69] M. Tatewaki, N. Tsuda, and T. Maruyama, "An analysis of disk flutter in hard disk drives in aerodynamic simulations," *IEEE Trans. Magn.*, vol. 37, no. 2, pp. 842–846, Mar. 2001.

[70] K. Aruga, M. Suwa, K. Shimizu, and T. Watanabe, "A Study on Positioning Error Caused by Flow Induced Vibration Using Helium-Filled Hard Disk Drives," *IEEE Trans. Magn.*, vol. 43, no. 9, pp. 3750–3755, Sep. 2007.

[71] "HOYA Starts to Build Next-Gen HDD Glass Substrate Production Facility." [Online]. Available: https://www.anandtech.com/show/13954/hoya-starts-to-build-nextgen-hdd-media-production-facility. [Accessed: 12-Jun-2019].

[72] "Progress and Outlook of HDD Technology - Xiaodong Che." [Online]. Available: https://www.slideshare.net/xuyunhao/caiss-ac-10-2012pub. [Accessed: 18-Jul-2019].

[73] H. J. Lee, R. D. Hempstead, and J. Weiss, "Study of head and disk interface in contact start/stop test," *IEEE Trans. Magn.*, vol. 25, no. 5, pp. 3722–3724, 1989.

[74] M. Suk and T. R. Albrecht, "The evolution of load/unload technology," *Microsyst. Technol.*, vol. 8, no. 1, pp. 10–16, Mar. 2002.

[75] B. Bhushan and K. Ono, *Advances in information storage systems. Volume 9*. World Scientific, 1999.

[76] B. Bhushan, *Nanotribology and nanomechanics : an introduction*. .

[77] A. K. Menon, “Interface tribology for 100 Gb/in2,” *Tribol. Int.*, vol. 33, no. 5–6, pp. 299–308, May 2000.

[78] Jing Gui, “Tribology challenges for head-disk interface toward 1 Tb/in/sup 2/,” *IEEE Trans. Magn.*, vol. 39, no. 2, pp. 716–721, Mar. 2003.

[79] J. Robertson, “Diamond-like amorphous carbon,” *Mater. Sci. Eng. R Reports*, vol. 37, no. 4–6, pp. 129–281, May 2002.

[80] T. E. Karis, G. W. Tyndall, and R. J. Waltman, “Lubricant Bonding Effects on Thin Film Disk Tribology,” *Tribol. Trans.*, vol. 44, no. 2, pp. 249–255, Jan. 2001.

[81] B. Marchon, T. Pitchford, Y.-T. Hsia, and S. Gangopadhyay, “The Head-Disk Interface Roadmap to an Areal Density of Tbit/in ^{2},” *Adv. Tribol.*, vol. 2013, pp. 1–8, Mar. 2013.

[82] “The History of Tribology | Fritsche - German manufacturer,” *Fritsche*. [Online]. Available: http://www.centrallubrication.com/history-tribology/. [Accessed: 05-Jun-2019].

[83] I. M. Hutchings and P. Shipway, *Tribology : friction and wear of engineering materials*. .

[84] B. Bhushan, *Introduction to tribology*. .

[85] E. Meyer, T. Gyalog, R. M. Overney, and K. Dransfeld, *Nanoscience: Friction and Rheology on the Nanometer Scale*. WORLD SCIENTIFIC, 1998.

[86] D. Dowson, “A generalized Reynolds equation for fluid-film lubrication,” *Int. J. Mech. Sci.*, vol. 4, no. 2, pp. 159–170, Mar. 1962.

[87] R. Stribeck, *Die wesentlichen Eigenschaften der Gleit- und Rollenlager*. Berlin: Julius Springer, 1903.

[88] F. P. Bowden and D. Tabor, *The friction and lubrication of solids*. Clarendon Press, 2001.

[89] J. F. Archard, “Contact and Rubbing of Flat Surfaces,” *J. Appl. Phys.*, vol. 24, no. 8, pp. 981–988, Aug. 1953.

[90] K. L. Johnson, “One Hundred Years of Hertz Contact,” *Proc. Inst. Mech. Eng.*, vol. 196, no. 1, pp. 363–378, Jun. 1982.

[91] B. Bhushan, *Springer handbook of nanotechnology*. Springer, 2010.

[92] E. H. Falcao and F. Wudl, “Carbon allotropes: beyond graphite and diamond,” *J. Chem. Technol. Biotechnol.*, vol. 82, no. 6, pp. 524–531, Jun. 2007.

[93] T. W. Scharf, R. D. Ott, D. Yang, and J. A. Barnard, “Structural and tribological characterization of protective amorphous diamond-like carbon and amorphous CNx overcoats for next generation hard disks,” *J. Appl. Phys.*, vol. 85, no. 6, pp. 3142–3154, Mar. 1999.

[94] C. Donnet and A. Erdemir, Eds., *Tribology of Diamond-Like Carbon Films*. Boston, MA: Springer US, 2008.

[95] A. Grill, “Tribology of diamondlike carbon and related materials: an updated review,” *Surf. Coatings Technol.*, vol. 94–95, pp. 507–513, Oct. 1997.

[96] A. H. Tan, “Corrosion and tribological properties of ultra-thin DLC films with different nitrogen contents in magnetic recording media,” *Diam. Relat. Mater.*, vol. 16, no. 3, pp. 467–472, Mar. 2007.

[97] R. J. Waltman, G. W. Tyndall, G. J. Wang, and H. Deng, “The Effect of Solvents on the Perfluoropolyether Lubricants Used on Rigid Magnetic Recording Media,” *Tribol. Lett.*, vol. 16, no. 3, pp. 215–230, Apr. 2004.

[98] C. Mathew, “Molecular tribology of disk drives.”

[99] Z. Tao and B. Bhushan, “Bonding, degradation, and environmental effects on novel perfluoropolyether lubricants,” *Wear*, vol. 259, no. 7–12, pp. 1352–1361, Jul. 2005.

[100] L. M. Matthes, R. Brunner, B. Knigge, and F. E. Talke, “Head Wear of Thermal Flying Height Control Sliders as a Function of Bonded Lubricant Ratio, Temperature, and Relative Humidity,” *Tribol. Lett.*, vol. 60, no. 3, p. 39, Dec. 2015.

[101] N. Shukla, E. Svedberg, J. van de Veerdonk, X. Ma, J. Gui, and A. J. Gellman, “Water adsorption on lubricated a-CH x in humid environments.”

[102] Z. Zhao and B. Bhushan, “Humidity effect on friction/stiction and durability of head-disk interface with polar perfluoropolyether lubricant,” *J. Appl. Phys.*, vol. 81, no. 8, pp. 5387–5389, Apr. 1997.

[103] “Experimental studies of the head-disk interface from a tribological and controls point of view for flying heights below 2 nm.”

[104] R. Z. Lei, A. J. Gellman, and P. Jones, “Thermal Stability of Fomblin Z and Fomblin Zdol Thin Films on Amorphous Hydrogenated Carbon,” *Tribol. Lett.*, vol. 11, no. 1, pp. 1–5, 2001.

[105] A. M. Homola, “Lubrication issues in magnetic disk storage devices,” *IEEE Trans. Magn.*, vol. 32, no. 3, pp. 1812–1818, May 1996.

[106] G. W. Tyndall, P. B. Leezenberg, R. J. Waltman, and J. Castenada, “Interfacial interactions of perfluoropolyether lubricants with magnetic recording media,” *Tribol. Lett.*, vol. 4, no. 2, pp. 103–108, 1998.

[107] Y. Ma and B. Liu, “Lubricant transfer from disk to slider in hard disk drives,” *Appl. Phys. Lett.*, vol. 90, no. 14, p. 143516, Apr. 2007.

[108] P. H. Kasai and V. Raman, “Lubricant Transfer in Disk Drives,” *Tribol. Lett.*, vol. 48, no. 3, pp. 367–374, Dec. 2012.

[109] R. J. Waltman, H. Deng, G. J. Wang, H. Zhu, and G. W. Tyndall, “The Effect of PFPE Film Thickness and Molecular Polarity on the Pick-Up of Disk Lubricant by a Low-Flying Slider,” *Tribol. Lett.*, vol. 39, no. 2, pp. 211–219, Aug. 2010.

[110] B. Marchon, T. Karis, Qing Dai, and R. Pit, “A model for lubricant flow from disk to slider,” *IEEE Trans. Magn.*, vol. 39, no. 5, pp. 2447–2449, Sep. 2003.

[111] S. Xiong, N. Wang, R. Smith, D. Li, E. Schreck, and Q. Dai, “Material Transfer Inside Head Disk Interface for Heat Assisted Magnetic Recording,” *Tribol. Lett.*, vol. 65, no. 2, p. 74, Jun. 2017.

[112] S. Xiong, R. Smith, J. Xu, S. Nishida, M. Furukawa, K. Tasaka, K. Kuroki, Y. Yoon, N. Wang, S. Canchi, E. Schreck, Q. Dai, “Setting Write Spacing in Heat Assisted Magnetic Recording,” *IEEE Trans. Magn.*, vol. 54, no. 8, pp. 1–7, Aug. 2018.

[113] “The feasibility of using helium (He) inside of.”

[114] P. de Groot, L. Deck, J. Soobitsky, and J. Biegen, “Polarization interferometer for measuring the flying height of magnetic read–write heads,” *Opt. Lett.*, vol. 21, no. 6, p. 441, Mar. 1996.

[115] C. Lacey, R. Shelor, A. J. Cormier, and F. E. Talke, “Interferometric measurement of disk/slider spacing: the effect of phase shift on reflection,” *IEEE Trans. Magn.*, vol. 29, no. 6, pp. 3906–3908, Nov. 1993.

[116] M. H. Wahl, J. C. Briggs, and F. E. Talke, “Interferometric spacing measurements of the Bernoulli head/disk interface,” *IEEE Trans. Magn.*, vol. 28, no. 5, pp. 2551–2553, Sep. 1992.

[117] “Accurate Measurement of Gas-Lubricated Slider Bearing Separation Using Visible Laser Interferometry,” 1988.

[118] L. Ma and C. Zhang, “Discussion on the Technique of Relative Optical Interference Intensity for the Measurement of Lubricant Film Thickness,” *Tribol. Lett.*, vol. 36,

no. 3, pp. 239–245, Dec. 2009.

[119] Xinqun Liu, W. Clegg, D. F. L. Jenkins, and Bo Liu, “Polarization interferometer for measuring small displacement,” *IEEE Trans. Instrum. Meas.*, vol. 50, no. 4, pp. 868–871, 2001.

[120] Xinqun Liu, W. Clegg, and Bo Liu, “Normal incidence polarization interferometer for measuring flying height of magnetic heads,” *IEEE Trans. Magn.*, vol. 35, no. 5, pp. 2457–2459, 1999.

[121] by Xinqunliu, “DEVELOPMENT OF IMPROVED HEAD-DISK SPACING MEASUREMENT METHODS FOR MAGNETIC DISK DRIVES,” 2002.

[122] Y. Mitsuya, Y. Kawamoto, H. Zhang, and H. Oka, “Head-Disk Spacing Measurement Using Michelson Laser Interferometry as Observed Through Glass Disk,” *J. Tribol.*, vol. 126, no. 2, p. 360, 2004.

[123] T. A. Riener, A. C. Goding, and F. E. Talke, “Measurement of head/disk spacing modulation using a two channel fiber optic laser Doppler vibrometer,” *IEEE Trans. Magn.*, vol. 24, no. 6, pp. 2745–2747, 1988.

[124] M. Suk, T. Ishii, and D. B. Bogy, “Comparison of flying height measurement between multi-channel laser interferometer and the capacitance probe slider,” *IEEE Trans. Magn.*, vol. 27, no. 6, pp. 5148–5150, Nov. 1991.

[125] N. A. Feliss and F. E. Talke, “Capacitance Probe Study of Rotating-Head/Tape Interface,” *IBM J. Res. Dev.*, vol. 21, no. 3, pp. 289–293, May 1977.

[126] Chua Lin, “Techniques for the measurement of air-bearing separation -- A review,” *IEEE Trans. Magn.*, vol. 9, no. 4, pp. 673–677, Dec. 1973.

[127] S. Millman, R. Hoyt, D. Horne, and B. Beye, “Motion pictures on in-situ air bearing dynamics,” *IEEE Trans. Magn.*, vol. 22, no. 5, pp. 1031–1033, Sep. 1986.

[128] B. Marchon, K. Saito, B. Wilson, and R. Wood, “The Limits of the Wallace Approximation for PMR Recording at High Areal Density,” *IEEE Trans. Magn.*, vol. 47, no. 10, pp. 3422–3425, Oct. 2011.

[129] R. L. Wallace, “The Reproduction of Magnetically Recorded Signals,” *Bell Syst. Tech. J.*, vol. 30, no. 4, pp. 1145–1173, Oct. 1951.

[130] Hao Zheng, Hui Li, and F. E. Talke, “Numerical Simulation of a Thermal Flying Height Control Slider With Dual Heater and Insulator Elements,” *IEEE Trans. Magn.*, vol. 45, no. 10, pp. 3628–3631, Oct. 2009.

[131] T. Shiramatsu, M. Kurita, K. Miyake, M. Suk, S. Ohki, H. Tanaka, S. Saegusa, “Drive Integration of Active Flying-Height Control Slider With Micro Thermal

Actuator," *IEEE Trans. Magn.*, vol. 42, no. 10, pp. 2513–2515, Oct. 2006.

[132] M. Kurita, T. Shiramatsu, K. Miyake, H. Tanaka, S. Saegusa, "Active flying-height control slider using MEMS thermal actuator," *Microsyst. Technol.*, vol. 12, no. 4, pp. 369–375, Mar. 2006.

[133] O. Reynolds, "IV. On the theory of lubrication and its application to Mr. Beauchamp tower's experiments, including an experimental determination of the viscosity of olive oil," *Philos. Trans. R. Soc. London*, vol. 177, pp. 157–234, Jan. 1886.

[134] M. Duwensee, "Numerical and experimental investigations of the head/disk interface."

[135] Uwe Boettcher, "Nano-scale positioning, control and motion planning in hard disk drives."

[136] Thomas J. R. Hughes, *The Finite Element Method: Linear Static and Dynamic Finite Element Analysis - Thomas J. R. Hughes - Google Books*. .

[137] Robert W. Bruce, *Handbook of Lubrication and Tribology: Theory and Design, Second Edition - Google Books*. .

[138] W. Peng, R. M. Crone, P. M. Jones, and Y.-T. Hsia, "Effect of van der Waals Force on Air-Bearing Flying Characteristics at Ultra-Low Fly Height," *IEEE Trans. Magn.*, vol. 42, no. 10, pp. 2483–2485, Oct. 2006.

[139] K. Ono, "Effect of van der Waals forces in a near contact head-disk interface," *IEEE Trans. Magn.*, vol. 44, no. 11 PART 2, pp. 3675–3678, Nov. 2008.

[140] R. R. Dagastine, L. R. White, P. M. Jones, and Y.-T. Hsia, "Effect of van der Waals forces on molecularly thin lubricant in the magnetic storage head-disk interface," *J. Appl. Phys.*, vol. 98, no. 12, p. 124906, Dec. 2005.

[141] G. W. Tyndall and R. Technology, "Role of the Head Disk Interface in HDD Role of the Head Disk Interface in HDD Reliability Reliability."

[142] H.-R. Ao, Z.-Y. Han, K. Zhang, and H.-Y. Jiang, "Lubricant film flow and depletion characteristics at head/disk storage interface," *Chinese Phys. B*, vol. 25, no. 12, p. 124601, Dec. 2016.

[143] L. R. White, R. R. Dagastine, P. M. Jones, and Y.-T. Hsia, "van der Waals force calculation between laminated media, pertinent to the magnetic storage head-disk interface," *J. Appl. Phys.*, vol. 97, no. 10, p. 104503, May 2005.

[144] B. E. Knigge, C. M. Mate, O. Ruiz, and P. M. Baumgart, *No Title*, vol. 40, no. 4. 2004, pp. 3165–3167.

[145] H. Tani, S. Koganezawa, and N. Tagawa, “Reduction in lubricant pickup by bias voltage between slider and disk surfaces,” *Microsyst. Technol.*, vol. 22, no. 6, pp. 1221–1225, Jun. 2016.

[146] H. Stenberg, M. H. Wahl, and F. E. Talke, “Comparison of numerical and experimental flying characteristics of tri-pad sliders,” *IEEE Trans. Magn.*, vol. 31, no. 6, pp. 2970–2972, 1995.

[147] R. Wood, “Future hard disk drive systems,” *J. Magn. Magn. Mater.*, vol. 321, no. 6, pp. 555–561, Mar. 2009.

[148] N. Liu, J. Zheng, and D. B. Bogy, “Thermal flying-height control sliders in hard disk drives filled with air-helium gas mixtures,” *Appl. Phys. Lett.*, vol. 95, no. 21, p. 213505, Nov. 2009.

[149] P. G. Levi and F. E. Talke, “Load/unload investigations on a rotary actuator disk drive,” *IEEE Trans. Magn.*, vol. 28, no. 5, pp. 2877–2879, Sep. 1992.

[150] S. Weissner and F. E. Talke, “Load/unload measurements using laser doppler vibrometry and acoustic emission,” *Tribol. Int.*, vol. 33, no. 5–6, pp. 367–372, May 2000.

[151] N. S. Tambe and B. Bhushan, “Effect of load/unload process on friction/stiction and durability of head-disk interface,” *Microsyst. Technol.*, vol. 8, no. 6, pp. 409–418, Sep. 2002.

[152] Yonghyun Lee ; Eo-Jin Hong ; Cheol-Soon Kim, “Effect of mechanical parameters for loading contact and instability in HDD.”

[153] Bo Liu and Yansheng Ma, “Visualization and characterization of slider-disk interactions in dynamic load/unload processes,” *IEEE Trans. Magn.*, vol. 39, no. 2, pp. 743–748, Mar. 2003.

[154] J. P. Peng, “Theoretical Prediction of Ramp Loading/Unloading Process in Hard Disk Drives,” *J. Tribol.*, vol. 121, no. 3, p. 568, Jul. 1999.

[155] H. AO, H. WEI, and H. JIANG, “Simulation of Head-Disk Interface and Ramp/Lift-Tab Interfaces During Load/Unload Process of Hard Disk Drive,” *J. Adv. Mech. Des. Syst. Manuf.*, vol. 4, no. 1, pp. 23–31, 2010.

[156] Z. Tang and F. E. Talke, “Investigation of slider flying characteristics and frequency response in helium-air gas mixtures,” *Microsyst. Technol.*, vol. 21, no. 12, pp. 2589–2596, Dec. 2015.

[157] J. Xu, J. D. Kiely, Y.-T. Hsia, and F. E. Talke, “Dynamics of ultra low flying sliders during contact with a lubricated disk,” *Microsyst. Technol.*, vol. 13, no. 8–10, pp. 1371–1375, Apr. 2007.

[158] L. Su, Y. Hu, E. L. Lam, P. Li, R. W. Ng, D. Liang, O. Zheng, H. Liu, Z. Deng, J. Zhang, "Tribological and Dynamic Study of Head Disk Interface at Sub-1-nm Clearance," *IEEE Trans. Magn.*, vol. 47, no. 1, pp. 111–116, Jan. 2011.

[159] W. Peng, J. Kiely, and Y.-T. Hsia, "Wear Analysis of Head-Disk Interface During Contact," *J. Tribol.*, vol. 127, no. 1, p. 171, Jan. 2005.

[160] Y. Wang, X. Wei, K.-L. Tsui, and T. W. S. Chow, "Tribological Degradation of Head–Disk Interface in Hard Disk Drives Under Accelerated Wear Condition," *IEEE Trans. Magn.*, vol. 50, no. 3, pp. 27–33, Mar. 2014.

[161] Y.-K. Chen, A. N. Murthy, R. Pit, and D. B. Bogy, "Angstrom Scale Wear of the Air-Bearing Sliders in Hard Disk Drives," *Tribol. Lett.*, vol. 54, no. 3, pp. 273–278, Jun. 2014.

[162] L. M. Matthes, F. E. Spada, A. Ovcharenko, B. E. Knigge, and F. E. Talke, "Effect of Head–Disk Interface Biasing and Relative Humidity on Wear of Thermal Flying Height Control Sliders," *Tribol. Lett.*, vol. 65, no. 2, p. 44, Jun. 2017.

[163] Ning Li, Lanshi Zheng, Yonggang Meng, and D. B. Bogy, "Experimental Study of Head-Disk Interface Flyability and Durability at Sub-1-nm Clearance," *IEEE Trans. Magn.*, vol. 45, no. 10, pp. 3624–3627, Oct. 2009.

[164] H. Li, B. Liu, W. Hua, and T.-C. Chong, "Intermolecular force, surface roughness, and stability of head-disk interface," *J. Appl. Phys.*, vol. 97, no. 10, p. 10P305, May 2005.

[165] "Negative biasing a slider with respect to a disk to reduce slider wear and provide burnish rate control," Dec. 2009.

[166] S. Rajauria, E. Schreck, and B. Marchon, "Voltage assisted asymmetric nanoscale wear on ultra-smooth diamond like carbon thin films at high sliding speeds," *Sci. Rep.*, vol. 6, no. 1, p. 25439, May 2016.

[167] I. Manousakis, S. Sankar, G. McKnight, T. D. Nguyen, and R. Bianchini, "Environmental Conditions and Disk Reliability in Free-cooled Datacenters." 2016.

[168] "Data Acquisition Toolbox - MATLAB," *MathWorks*. [Online]. Available: https://www.mathworks.com/products/daq.html. [Accessed: 05-Jun-2019].

[169] T. D. Trinh, F. E. Spada, A. Ovcharenko, and F. E. Talke, "Investigation of the Contact Potential of the Head-Disk Interface Using Kelvin Probe Measurements," in *ASME-JSME 2018 Joint International Conference on Information Storage and Processing Systems and Micromechatronics for Information and Precision Equipment*, 2018, p. V001T01A008.

[170] S. Rajauria, S. V. Canchi, E. Schreck, and B. Marchon, "Nanoscale wear and kinetic

friction between atomically smooth surfaces sliding at high speeds," *Appl. Phys. Lett.*, vol. 106, no. 8, p. 081604, Feb. 2015.

[171] R. W. (Robert W. Revie and H. H. Uhlig, *Corrosion and corrosion control : an introduction to corrosion science and engineering*. .

[172] A. J. Wallash, "Electrostatic Discharge and Electrical Breakdown Study of the Head–Disk Interface in a Hard Disk Drive," *IEEE Trans. Magn.*, vol. 40, no. 3, pp. 1751–1755, May 2004.

[173] B. C. Stipe, T. C. Strand, C. C. Poon, H. Balamane, T. D. Boone, J. A. Katine, J. - L. Li, V. Rawat, H. Nemoto, A. Hirotsune, A. Hellwig, R. Ruiz, E. Dobisz, D. S. Kercher, N. Robertson, T. R. Albrecht, B. D. Terris, "Magnetic recording at 1.5 Pb m−2 using an integrated plasmonic antenna," *Nat. Photonics*, vol. 4, no. 7, pp. 484–488, Jul. 2010.

[174] Guzik Technical Enterprises, "Spinstands - Guzik Technical Enterprises." [Online]. Available: https://www.guzik.com/products/head-and-media-disk-drive-test/spinstands/. [Accessed: 17-Jun-2019].

[175] E. Schreck, D. Li, S. V. Canchi, L. Huang, G. P. Singh, B. Marchon, H. J. Richter, B. Stipe, M. Staffaroni, "Thermal Aspects and Static/Dynamic Protrusion Behaviors in Heat-Assisted Magnetic Recording," *IEEE Trans. Magn.*, vol. 50, no. 3, pp. 126–131, Mar. 2014.

[176] E. Schreck, , D. Li, S. V. Canchi, L. Huang, G. P. Singh, B. Marchon, H. J. Richter, B. Stipe, M. Staffaroni, "Thermal aspects and static/dynamic protrusion behaviors in heat-assisted magnetic recording," *IEEE Trans. Magn.*, vol. 50, no. 3, pp. 126–131, 2014.

[177] D. Li, M. Staffaroni, E. Schreck, and B. Stipe, "A New AFM-Based Technique to Detect the NFT Protrusion on HAMR Head," *IEEE Trans. Magn.*, vol. 49, no. 7, pp. 3576–3579, Jul. 2013.

[178] "US9595280B2 - Hard disk drive head-disk interface dithering - Google Patents." [Online]. Available: https://patents.google.com/patent/US9595280B2/en. [Accessed: 12-Dec-2019].

[179] A. Q. Wu, Y. Kubota, T. Klemmer, T. Rausch, C. Peng, Y. Peng, D. Karns, X. Zhu, Y. Ding, E. K. C. Chang, Y. Zhao, H. Zhou, K. Gao, J. - U. Thiele, M. Seigler, G. Ju, E. Gage, "HAMR Areal Density Demonstration of 1+ Tbpsi on Spinstand," *IEEE Trans. Magn.*, vol. 49, no. 2, pp. 779–782, Feb. 2013.

[180] Alexander Taratorin, *Guzik - Magnetic Recording Systems and Measurements Chapter 7 - Guzik Technical Enterprises*. 2004.

[181] C. Papusoi, T. Le, P.-O. Jubert, D. Oswald, B. Ozdol, D. Tripathy, P. Dorsey, M.

Desai, “L10 FePt films with high TC capping layer for Heat Assisted Magnetic Recording (HAMR),” *J. Magn. Magn. Mater.*, vol. 483, pp. 249–265, Aug. 2019.

[182] D. L. Windt, W. C. Cash, M. Scott, P. Arendt, B. Newnam, R. F. Fisher, A. B. Swartzlander, “Optical constants for thin films of Ti, Zr, Nb, Mo, Ru, Rh, Pd, Ag, Hf, Ta, W, Re, Ir, Os, Pt, and Au from 24 Å to 1216 Å,” *Appl. Opt.*, 1988.

[183] P. Yu, W. Zhou, S. Yu, and Y. Zeng, “Laser-induced local heating and lubricant depletion in heat assisted magnetic recording systems,” *Int. J. Heat Mass Transf.*, vol. 59, no. 1, pp. 36–45, 2013.

[184] R. E. Rottmayer, S. Batra, D. Buechel, W. A. Challener, J. Hohlfeld, Y. Kubota, L. Li, B. Lu, C. Mihalcea, K. Mountfield, K. Pelhos, C. Peng, T. Rausch, M. A. Seigler, D. Weller, X.-M. Yang, “Heat-Assisted Magnetic Recording,” *IEEE Trans. Magn.*, vol. 42, no. 10, pp. 2417–2421, Oct. 2006.

[185] Y. S. Ma, Y. J. Man, M. Shakerzadeh, H. L. Seet, R. Ji, R. Y. Zheng, H. J. Chung, X. Y. Chen, J. F. Hu, T. Yamamoto, R. Hempstead, “Laser-Heating-Induced Damage to Ultrathin Carbon Overcoat in Heat-Assisted Magnetic Recording,” *Tribol. Lett.*, vol. 53, no. 1, pp. 303–310, Jan. 2014.

[186] R. Ji, Y. Ma, M. Shakerzadeh, H. Li Seet, and J. Feng Hu, “Laser irradiation effect on carbon overcoat for HAMR application,” 2014.

[187] Y. W. Seo, A. Rosenkranz, and F. E. Talke, “Molecular dynamics study of lubricant depletion by pulsed laser heating,” *Appl. Surf. Sci.*, vol. 440, pp. 73–83, May 2018.

[188] J. D. Kiely, P. M. Jones, Y. Yang, J. L. Brand, M. A. Dufresne, P. C. Fletcher, F. Zavaliche, Y. Toivola, J. C. Duda, M. T. Johnson, “Write-Induced Head Contamination in Heat-Assisted Magnetic Recording,” *IEEE Trans. Magn.*, vol. 53, no. 2, pp. 1–7, Feb. 2017.